

Evaluation of the Potential Radar Cross-
Section & Experimental Aero-Acoustic
Noise Merits of the GA-ASI MQ-9 Reaper
by Applying Flap Morphing

M.W. Hayat

Technische Universiteit Delft

THIS PAGE IS INTENTIONALLY LEFT BLANK

Evaluation of the Potential Radar Cross-Section & Experimental Aero-Acoustic Noise Merits of the GA-ASI MQ-9 Reaper by Applying Flap Morphing

by

M.W. Hayat

in partial fulfillment of the requirements for the degree of

Master of Science
in Aerospace Engineering

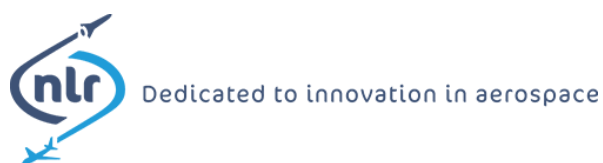
at the Delft University of Technology,
to be defended publicly on Wednesday July 4, 2018 at 10:00 AM.

Thesis registration number:

Supervisors: Dr. ir. R. Vos, TU Delft
 Ir. J. W. Dominicus, NLR

Thesis committee: Prof. dr. ing. G. Eitelberg, TU Delft
 Dr. ir. R. Vos, TU Delft
 Dr. ir. M. Snellen, TU Delft
 Ir. J. W. Dominicus, NLR

An electronic version of this thesis is available at <http://repository.tudelft.nl/>



Abstract

Defence institutions and military aircraft manufacturers are increasingly exploring the ways to improve stealth in new aircraft designs. Design for low observability, more specifically for low Radar Cross-Section is the fundamental design aspect during design of a new military aerial vehicle. Acoustic stealth is also an important characteristic of an aerial vehicle and is one of the main objectives during the design of a stealth aircraft to avoid being heard by the enemy troops below.

Although there has been some work done in the past on flap morphing of wings, there are still some engineering aspects of flap morphing which are still left unexplored. Previous research focused more on aerodynamic and structural aspects of flap morphing. Couple of these unexplored aspects are the Aero-Acoustic Noise and Radar Cross-Section assessment of flap morphing. Flap gaps, kinematics and side-edges are a source of generating noise and radar signature and through flap morphing potential merits of these two aspects can be assessed.

Flap morphing technology is most likely to be used on unmanned military aerial vehicles. Therefore, the GA-ASI MQ-9 Reaper was used for achieving the research objectives in this thesis work. The study focuses on the Aero-Acoustic noise and Radar Cross-Section merits through flap morphing of the GA-ASI MQ-9 Reaper. Aero-Acoustic noise analysis were performed experimentally as well as analytically whereas Radar Cross-Section merits were obtained by performing simulations.

From the Aero-Acoustic noise experiments on the scaled 3D printed morphing and conventional wings of GA-ASI MQ-9 Reaper, noise reduction in the morphing wing have been observed in all configurations and operational settings. From the 35m/s noise experiments, Overall Sound Pressure Level reduction is observed between 4.7% and 38.2% for different angles of attack whereas reduction in the overall Sound Pressure Level between 20.66% and 32.2% have been observed with 50m/s. Similarly, with the Werner Dobrzynski's noise prediction technique, together with Karl-Stephane Rossignol's flap side-edge noise prediction model, benefits in the noise generation are observed for the morphing wings. For similar geometrical configurations as experiments, noise reduction variation in the predicted Overall Sound Pressure Level lies between 37% and 46% for different angles of attack at 50 m/s.

For the mono-static Radar Cross-Section with trailing edge and flap deflection of 0° , a significant reduction in the radar signature is observed for the morphing wing, whereas for 25° trailing edge and flap deflection it turns out that the radar signature for the morphing wing is very similar or slightly higher than the conventional wing. For the mono-static radar signature with 0° trailing edge and flap deflection, after summation of total RCS in all 360 directions, a maximum and minimum decrease of 10.52dBsm and 9.95dBsm have been observed by flap morphing whereas for 25° trailing edge and flap deflection an increase in radar signature between 1.54 and 2 dBsm was noticed. Bi-static RCS analysis were also performed on the 0° trailing edge and flap deflection of where the decrease in radar signature between 4 and 18 dBsm was observed.

Acknowledgements

My time as a student at TU Delft is coming to an end with this thesis work after which I will obtain my Master of Science degree. First of all, I would like to express gratitude to my principle supervisors, Dr.ir. Roelof Vos from TU Delft and Ir. Jacco Dominicus from the Netherlands Aerospace Centre for all their help, guidance and insights during this thesis work. I am grateful for this excellent opportunity at the Netherlands Aerospace Center. NLR was always very supportive of the ideas I used to come up with and this helped in molding this thesis into some very exciting and innovative work.

In addition, this thesis work was supported by a number of other people from the TU Delft and the NLR to whom I would like to express my gratitude. First of all, I would like to thank Eddy van den Bos, CAD specialist at Aerospace Engineering faculty of TU Delft for guiding and helping me whenever I ran into problems with CATIA during modelling of the wings. I would also like to extend my gratitude to Dr. ir. Abhishek Sahai from TU Delft for providing the literature material and his guidance in selecting and adapting the analytical noise prediction method. I would like to thank Dr. Mark-Jan van der Meulen from the NLR and the technicians from the NLR AV-LAB for their complete support in setting up and performing the experiments. I would also like to thank Ralph Haagsma from the NLR for helping me with the 3D printing of the wing prototypes.

Special thanks to my fellow students and colleagues for constantly supporting and motivating me throughout my time at TU Delft and during my thesis work at the NLR Amsterdam.

Last but not least my journey to become a successful engineer may not have been possible without support of many from my personal life. I would like to express many thanks to the generous and selfless support of my parents, wife and siblings for not only over this period of research but throughout my entire studies.

THANK YOU!

M.W. Hayat
Oslo, May 2018

Contents

Abstract	iv
Acknowledgements	v
List of Symbols	viii
List of Abbreviations	ix
List of Figures	x
List of Tables	xiii
1 Introduction	1
2 Background & State-of-the-art Morphing Wing Techniques	5
2.1 Overview of Morphing Wing Enablers	5
2.1.1 Shape Memory Alloy devices (SMA)	5
2.1.2 Shape Memory Polymers (SMP)	6
2.1.3 Piezoelectric Actuators (PZT)	6
2.1.4 Active Aeroelastic Concepts for twist	7
2.1.5 Hyper Elliptic Cambered Span (HECS)	8
2.1.6 Dihedral/Gull actuation	8
3 Redesign of the MQ-9 Reaper Wing	10
3.1 Geometrical Properties of Conventional MQ-9 Reaper	10
3.2 Sizing of the Morphing Wing	10
3.3 CAD modelling of the Wings	16
3.3.1 Conventional	16
3.3.2 Morphed	20
4 Aero-Acoustic Noise Analysis & Evaluation	24
4.1 Acoustic Metrics	24
4.1.1 A-weighted Sound Pressure Level (dBA)	24
4.1.2 C-weighted Sound Pressure Level (dBC)	25
4.1.3 Sound Exposure Level (SEL)	25
4.1.4 Perceived Noise Level (PNL)	25
4.1.5 Effective Perceived Noise Level (EPNL)	25
4.2 Experimental Aero-Acoustic Noise Analysis	26
4.2.1 3D Printing of the wing models	26
4.2.2 Experimental setup	29
4.2.3 Results from the experiments	35
4.3 Analytical Aero-Acoustic Noise Analysis	49
4.3.1 Werner Dobrzynski's noise prediction model	50
4.3.2 Flap Side-Edge noise prediction and modelling	53
4.3.3 Results and comparison to the experimental data	54

5	Radar Cross-Section Analysis & Evaluation	56
5.1	RCS theoretical background	57
5.1.1	Mono-static RCS	59
5.1.2	Bi-static RCS	59
5.2	Radar Cross-Section Measurement Software	60
5.2.1	FEKO overview	60
5.3	FEKO Solvers	61
5.3.1	Solver selection for RCS simulations	62
5.4	Radar Cross-Section Simulations Setup	62
5.4.1	Frequency, excitations and requests	65
5.4.2	Solution settings	65
5.4.3	Models & mesh	66
5.4.4	Simulations	71
5.5	Results from RCS Simulations	72
5.5.1	Monostatic RCS	72
5.5.2	Bi-static RCS	74
5.6	Discussion of results	77
5.7	Validation of Hyperworks-FEKO	78
5.7.1	Experimental data	79
5.7.2	FEKO measurements	80
6	Conclusions & Recommendations	83
6.1	Conclusions	83
6.2	Recommendations	84
A	History of Morphing Wing Aircraft	86
B	Future of Morphing Wings in Military Domain	87
C	Additional Radar Cross-Section Results	88
C.1	Mono-static RCS	88
C.2	Bi-Static RCS	90
D	Additional Aero-Acoustic Noise Results	93
D.1	SPL spectras	93
D.2	Beamforming results	98
	Bibliography	103

List of Symbols

<i>Symbol</i>	<i>Description</i>	<i>Unit</i>	<i>Symbol</i>	<i>Description</i>	<i>Unit</i>
n_{max}	Maximum noy value	[-]	PNL	Perceived Noise Level	[dB]
N	Overall noy	[-]	k	Time step index	[-]
d	Time interval	[s]	D	Duration correction factor	[-]
$p_{i_{airframe}}$	Far-field airframe SPL	[dB]	b_W	Wing span	[m]
K_i	Empirical constant	[-]	δ_w^*	Boundary layer thickness	[m]
A_w	Wing surface area	[m ²]	F_S	Spectral function	[-]
N	Number of microphones	[-]	\mathbf{p}	Pressure vector	[-]
θ	Polar directivity angle	[°]	δ_f	Flap deflection angle	[°]
A_f	Flap area	[m ²]	c	Speed of sound	[m/s]
D	Array diameter	[m]	G	Green's function	[-]
S_f	Flap Strouhal number	[-]	I	Acoustic intensity	[W/m ²]
I_{ref}	Reference acoustic intensity	[W/m ²]	β	Lateral emission angle	[°]
B	Source Cross-Power	[dB]	\mathbf{C}	Cross-Spectral Matrix	[-]
v_{ref}	Reference velocity	[m/s]	x_{ref}	Ref. dimension noise source	[m]
v_m	Mean inflow velocity	[m/s]	l_a	Mean airfoil length	[m]
P_{ref}	Reference pressure	[Pa]	x_{ref}	Ref. dimension noise source	[m]
\mathbf{g}	Green's steering vector	[-]	\mathbf{h}	Empirical steering vector	[-]
Δw	Element length	[m]	u_0	Characteristic velocity scale	[m/s]
p	Complex pressure amp.	[-]	\mathbf{w}	CB weight vector	[-]
ψ	Trailing edge sweep angle	[°]	ν	Wing dihedral angle	[°]
Str_{max}	Maximum Strouhal number	[-]	l_f	Deployed flap length	[m]
f	1/3 octave center frequency	[Hz]	U_c	Cross-flow velocity	[m/s]
A	Source auto-power from CB	[dB]	a	Pressure amp.(complex) at source	[-]
S_g	Directional power density	[W/m ³]	σ	Radar Cross-Section	[m ²]
P_s	Transmitted power	[W]	R_1	Range(antenna-aim)	[m]
S_t	Power density	[W/m ³]	S_r	Total scattered power density	[W/m ³]
R_2	Range(aim-antenna)	[m]	A_W	Effective antenna aperture	[m ²]
A	Antenna geometrical area	[m ²]	K_a	Antenna efficiency	[%]
G	Antenna gain	[dBi]	R_{max}	Maximum range	[m]
A_e	Projected area	[m ²]	L_{Atm}	Atmospheric losses	[dBi]
Dw	Raw time signal	[-]	\tilde{P}	Sound pressure	[Pa]
Δnbf	Narrow band freq. band-width	[Hz]	PSD	Power Spectral density	[(W/Hz)]

<i>Subscripts</i>	<i>Description</i>	<i>Subscripts</i>	<i>Description</i>
ref	Reference	dir	Directivity
vel	Velocity	$norm$	Normal
geo	Geometrical	TE	Trailing edge
cl	Lift coefficient	m	Mean inflow
$spec$	Spectral	fse	Flap side-edge
c	Chord	0	Free-stream
rms	Root mean square	w	Wing
max	Maximum	r	Reciever
t	Transmitter	rms	Root mean square

List of Abbreviations

<i>Abbreviation</i>	<i>Description</i>
AASs	Aeroelastic Structures
AAW	Active Aeroelastic Wing
ACTE	Adaptive Compliant Trailing Edge
AFRL	Air Force Research Laboratory
AFW	Active Flexible Wing
AMVT	All Moving Vertical Tail
ANOPP	Aircraft Noise Prediction Program
ATS	Adaptive Torsion Structure
CAA	Computational Aero-Acoustics
DARPA	Defense Advanced Research Projects Agency
DLR	Deutsches Zentrum für Luft- und Raumfahrt/German Aerospace Center
FAA	Federal Aviation Authority
HECS	Hyper Elliptic Cambered Span
LE	Leading Edge
MAS	Morphing Aircraft Structures
PSF	Point Spread Function
MAVs	Micro Aerial Vehicles
MLFMM	Multi-Level Fast Multiple-Method
NLR	Nederlands Lucht- en Ruimtevaartcentrum/Netherlands Aerospace Center
PANAM	Parametric Noise Analysis Module
PZT	Piezoelectric Actuators
PWL	Sound Power Level
QFF	Quiet Flow Facility
RADAR	RADio Detection And Ranging
SMA	Shape Memory Alloys
SMP	Shape Memory Polymers
TE	Trailing Edge
UAV	Unmanned Aerial Vehicle
VSS	Variable Stiffness Spar

List of Figures

1.1	Illustration of conventional high lift devices and the morphed airfoil [52]	1
1.2	NASA's Adaptive Compliant Trailing Edge (ACTE) project	2
1.3	Project flow diagram	3
2.1	Classification of wing morphing concepts	5
2.2	Chordwise bending of Unmorphed(top) and morphed(bottom) surfaces achieved by varying heat of SMA strips [16]	6
2.3	Wind tunnel testing of the Boeing Smart Rotor [47]	7
2.4	Tendon-based spool system for Hyper Elliptic Cambered Span concept	8
2.5	Lockheed Martin Z-wing	9
2.6	Wind tunnel testing of the Z-Wing	9
3.1	$cl - \alpha$ curves for LS(1)-0417 and its morphed version for two different deflection angles	11
3.2	Single slotted fowler flap extension and deflections with corresponding chord lengths	13
3.3	Geometrical properties of existing MQ-9 Reaper [48]	13
3.4	Conventional wing(blue) and the new morphing wing planform(red)	16
3.5	Render of the conventional MQ-9 Reaper without flap attachment	17
3.6	Flap layout for the Boeing 747SP for two different configurations [38]	18
3.7	Render of the designed morphing MQ-9 Reaper with and without chord extension	18
3.8	The designed morphing MQ-9 Reaper and the Boeing 747SP with flap deflections	19
3.9	Another rendered view of the designed MQ-9 Reaper with the flap deflection	19
3.10	Line drawing of the wing and the flap assembly	20
3.11	Render of the modelled conventional MQ-9 Reaper wing with the flap attachment	20
3.12	Flexsys morphing wing concept with side-edges highlighted	21
3.13	Gap bridging between the deflecting trailing edges and the outboard wing for NASA morphing wing concept and the modelled MQ-9 morphing wing	21
3.14	Modelling of the MQ-9 morphing wing in CATIA with transition surface airfoils highlighted	22
3.15	Line drawing of the morphing wing	22
3.16	Render of the morphed wing with a trailing edge deflection of 25°	23
4.1	Noise-radiating components on an aircraft	24
4.2	Duration correction for Perceived Noise Level [44]	26
4.3	3D printed morphing wing using ABS plastic with layer delaminations highlighted	27
4.4	Interface rod to mount the wing in the test section	27
4.5	Morphed and conventional wings being 3D printed with Ultimaker 3 Extended	28
4.6	Morphed wing glued after 3D printing with glued surface highlighted	29
4.7	Both conventional and morphed wing models ready for testing	29
4.8	Anechoic chamber in the windtunnel is equipped with noise absorbing foam wedges	30
4.9	Wing profile mounted between two horizontal side-plates	30
4.10	Layout of the microphone array	31
4.11	View of the wing(morphed) fitted between side-plates and in front of the microphone array	32
4.12	Calibration factors for all 48 microphones	33
4.13	Overview of the noise facility before an experiment	34
4.14	Sound Pressure Level spectra for the speaker with two different frequencies and speaker positions	36
4.15	Windtunnel and background noise for 35,50 and 70m/s	37
4.16	SPL spectra for morphed and conventional wing along background noise with angle of attack of 8° for two different speeds and microphones	38
4.17	SPL spectra for morphed and conventional wing along background noise with angle of attack of 10° for two different speeds and microphones	39

4.18	SPL spectra for morphed and conventional wing along background noise with angle of attack of 12° for two different speeds and microphones	40
4.19	Illustration of side lobes in PSF[5]	43
4.20	Beamform maps of speaker with two different frequencies and speaker position at (0,0,0)	46
4.21	Beamform maps for the conventional and the morphing wing with an 8° angle of attack and 35m/s	46
4.22	Beamform maps for the conventional and the morphing wing with an 8° angle of attack and 50m/s	47
4.23	Beamform maps for the conventional and the morphing wing with a 10° angle of attack and 35m/s	47
4.24	Beamform maps for the conventional and the morphing wing with a 10° angle of attack and 50m/s	48
4.25	Beamform maps for the conventional and the morphing wing with a 12° angle of attack and 35m/s	48
4.26	Beamform maps for the conventional and the morphing wing with a 12° angle of attack and 50m/s	49
4.27	Clean airfoil noise at the trailing edge generated due to turbulent flow [40]	50
4.28	Vortex structures at flap side-edge due to flap deployment [14]	53
5.1	Continuous wave radar operation	56
5.2	Pulse radar operation	56
5.3	Radar reflection sources on a fighter aircraft	57
5.4	Connection between different terms in the equations used	58
5.5	Mono-static Radar	59
5.6	Bi-static Radar	60
5.7	Process flow diagram for RCS simulations	64
5.8	An example of different excitations and far-field bi-static analysis setup in FEKO	65
5.9	Finer mesh adaptation at the wing leading edge	66
5.10	Mono-static RCS signature of the wings with TE deflection of 0° with radar location at $\theta=155^\circ$ & $\phi=0^\circ$	72
5.11	Mono-static RCS signature of the wings with TE deflection of 0° with radar location at $\theta=205^\circ$ & $\phi=0^\circ$	73
5.12	Mono-static RCS signature of the wings with a TE deflection of 25° and the radar location at $\theta=155^\circ$ & $\phi=0^\circ$	73
5.13	Mono-static RCS signature of the wings with a TE deflection of 25° and the radar location at $\theta=205^\circ$ & $\phi=0^\circ$	74
5.14	Bi-static RCS signatures of the wings with the transmitting radar located at $\theta=120^\circ$ & $\phi=0^\circ$ and the receiver radar located at $\theta=240^\circ$ & $\phi=160^\circ$	75
5.15	Bi-static RCS signature of the wings with the transmitting radar located at $\theta=120^\circ$ & $\phi=0^\circ$ and the receiver radar located at $\theta=240^\circ$ & $\phi=320^\circ$	75
5.16	Bi-static RCS signature of the wings with the transmitting radar located at $\theta=240^\circ$ & $\phi=0^\circ$ and the receiver radar located at $\theta=120^\circ$ & $\phi=160^\circ$	76
5.17	Bi-static RCS signature of the wings with the transmitting radar located at $\theta=240^\circ$ & $\phi=0^\circ$ and the receiver radar located at $\theta=120^\circ$ & $\phi=320^\circ$	77
5.18	Experimental data extraction for validation	80
5.19	Comparison of RCS signatures of experimental and simulated analysis in a polar plot	81
5.20	Comparison of RCS signatures of experimental and simulated analysis in a 2D plot	81
A.1	Timeline of the implementation of morphing wing technologies [39]	86
C.1	Mono-static RCS signature of the wings with a TE deflection of 0° and the radar location at $\theta=105^\circ$ & $\phi=0^\circ$	88
C.2	Mono-static RCS signature of the wings with a TE deflection of 0° and the radar location at $\theta=255^\circ$ & $\phi=0^\circ$	89
C.3	Mono-static RCS signature of the wings with a TE deflection of 25° and the radar location at $\theta=105^\circ$ & $\phi=0^\circ$	89

C.4	Mono-static RCS signature of the wings with a TE deflection of 25° and the radar location at $\theta= 255^\circ$ & $\phi =0^\circ$	90
C.5	Bi-static RCS signature with the transmitting radar located at $\theta= 120^\circ$ & $\phi =0^\circ$ and the receiver radar located at $\theta= 240^\circ$ & $\phi= 80^\circ$	90
C.6	Bi-static RCS signature with the transmitting radar located at $\theta= 120^\circ$ & $\phi =0^\circ$ and the receiver radar located at $\theta= 240^\circ$ & $\phi= 240^\circ$	91
C.7	Bi-static RCS signature with the transmitting radar located at $\theta= 240^\circ$ & $\phi =0^\circ$ and the receiver radar located at $\theta= 120^\circ$ & $\phi= 80^\circ$	91
C.8	Bi-static RCS signature with the transmitting radar located at $\theta= 240^\circ$ & $\phi =0^\circ$ and the receiver radar located at $\theta= 120^\circ$ & $\phi= 240^\circ$	92
D.1	SPL spectra for the morphed and the conventional wing along the background noise with an angle of attack of 0° for two different speeds and microphones	93
D.2	SPL spectra for the morphed and the conventional wing along the background noise with an angle of attack of 2° for two different speeds and microphones	94
D.3	SPL spectra for the morphed and the conventional wing along the background noise with an angle of attack of 4° for two different speeds and microphones	94
D.4	SPL spectra for the morphed and the conventional wing along the background noise with an angle of attack of 6° for two different speeds and microphones	95
D.5	SPL spectra for each AOA starting with 2° with microphone 39 and the speed of 35, 50 and 70 m/s	96
D.6	SPL spectras for each AOA starting with 2° with microphone 39 and the speed of 35 and 50 m/s	97
D.7	Beam maps of speaker with two 1000Hz(left) and 5000Hz(right) and speaker position at (0.3,-0.21,0)	98
D.8	Beam maps for the windtunnel and the background noise with 35 m/s(left) and 50 m/s(right) speeds	98
D.9	Beam maps for the conventional(right) and the morphed(left) wing with 0° angle of attack and 35m/s	99
D.10	Beam maps for the conventional(right) and the morphed(left) wing with 0° angle of attack and 50m/s	99
D.11	Beam maps for the conventional(right) and the morphed(left) wing with 2° angle of attack and 35m/s	100
D.12	Beam maps for the conventional(right) and the morphed(left) wing with 2° angle of attack and 50m/s	100
D.13	Beam maps for the conventional(right) and the morphed(left) wing with 4° angle of attack and 35m/s	101
D.14	Beam maps for the conventional(right) and the morphed(left) wing with 4° angle of attack and 50m/s	101
D.15	Beam maps for the conventional(right) and the morphed(left) wing with 6° angle of attack and 35m/s	102
D.16	Beam maps for the conventional(right) and the morphed(left) wing with 6° angle of attack and 50m/s	102

List of Tables

3.1	Geometrical parameters of the existing MQ-9 Reaper	10
3.2	Increase in maximum lift coefficient for different types of flaps	12
3.3	2D and 3D lift contribution from the wing and the flap	14
3.4	New MQ-9 morphing wing planform	15
4.1	Important parameters of the microphones used in experiments	31
4.2	Final test matrix	35
4.3	Test matrix for speaker analysis	36
4.4	Overall Sound Pressure Level comparison between both wings	41
4.5	Overall A-weighted Sound Pressure Level comparison between both wings	42
4.6	Comparison of predicted Overall Sound Pressure Level between both wings	55
5.1	Wing configurations and radar positioning for mono-static RCS	63
5.2	Wing configurations and Radar positioning for bi-static RCS	63
5.3	Mesh information for four wing types	67
5.4	Mono-static Radar Cross-Section comparison of the wings with a TE deflection of 0°	78
5.5	Mono-static Radar Cross-Section comparison of the wings with a TE deflection of 25°	78
5.6	Bi-Static Radar Cross-Section comparison of the wings with a TE deflection of 0° by summation of total RCS from 0 to 360°	78
B.1	Future of Shape-Changing Structures in Military domain (<i>Note: EM-Electromagnetic & CoG-Center of Gravity</i>)	87

1. Introduction

Shape changing structures in aerial vehicles offer an attractive alternative or addition to conventional aerodynamic control surfaces such as slats, flaps, elevators, ailerons and rudders. The traditional reason to change the outer shape of an aerial vehicle is either to gain some aerodynamic benefit, such as reducing drag or lowering the stall speed, or to apply control to the platform by means of inducing pitch, roll or yaw moments, or direct lift control.

The first powered flight that Wright Brothers flew did not have conventional control surfaces. It had a "wing warping" phenomenon meaning that the wings were very lightweight and Wright Brothers twisted them to get flight control. It enabled roll control by changing the twist of the wing using the cables actuated by the pilot itself. This could be said to be the original motivation or the original morphing of the wing. In the present or near future, this technology is expected to be limited to just the unmanned aerial vehicles/military vehicles. The FAA puts so many roadblocks on the new technologies that it will be decades before shape-changing/morphing technology shows up in civil aviation.

The military community is also interested in the aerodynamic benefits and structural enablers and consequences to platforms of shape changing structures. But the potential effect on RCS is an added benefit for military users as well. Gaps that are associated with conventional hinged high-lift devices and control surfaces are a source of increased radar reflection and noise generation. Reducing or eliminating the need for such gaps by means of shape changing structures has a potential benefit in terms of observability and acoustic stealth.

An illustration of conventional high lift devices and the morphed trailing edge is shown in Figure 1.1.

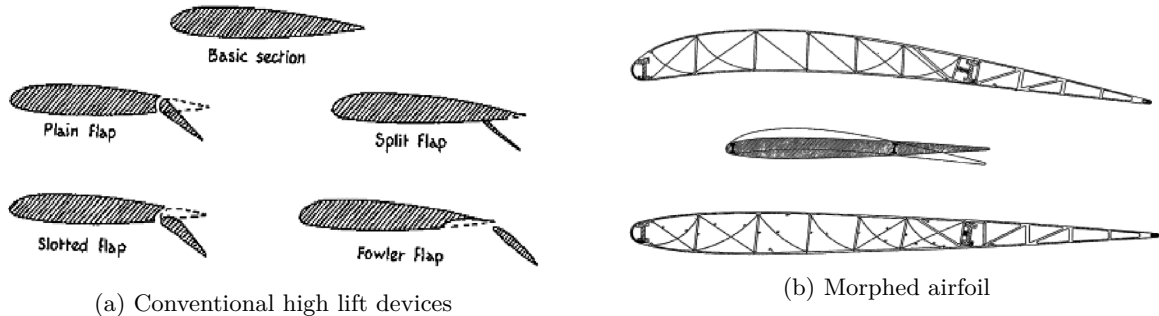


Figure 1.1: Illustration of conventional high lift devices and the morphed airfoil [52]

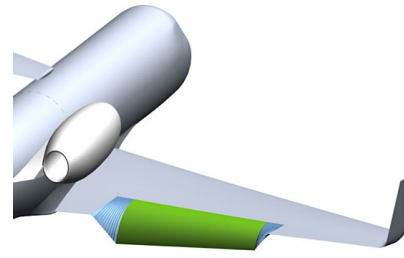
Although not new to aviation, shape changing structures are currently under renewed interest by aircraft designers, driven by recent technological innovations and developments. This has resulted in research programs which include real-life applications of flap morphing structures on test aircraft. While shape changing adds complexity to the design and poses structural challenges, its potential benefits might outweigh the drawbacks. For instance, flap morphing technology has already been tested by NASA together with the US Air Force Research Laboratory (AFRL). Application and illustration of this technology by NASA can be found in Figures 1.2a¹ and 1.2b² respectively.

¹URL:<https://www.nasa.gov/centers/armstrong/news/NewsReleases/2014/14-33.html> [Cited 14-Apr-2017]

²URL: <https://www.nasa.gov/centers/armstrong/research/ACTE/index.html> [Cited 14-Apr-2017]



(a) NASA Armstrong's G-III during flight test for the Adaptive Compliant Trailing Edge (ACTE) project



(b) Illustration of the experimental morphing flaps on NASA Armstrong's G-III for ACTE project

Figure 1.2: NASA's Adaptive Compliant Trailing Edge (ACTE) project

Research Aims

Although there has been some work done in the past on flap morphing of wings but there are still some engineering aspects of flap morphing which are still left unexplored. Previous research focused more on aerodynamic and structural aspects of flap morphing. Couple of these unexplored aspects are the Aero-Acoustic noise and Radar Cross-Section assessment of flap morphing.

Research on two very novel subjects with respect to morphing of the wing flaps is done during this thesis work. With very limited research in these fields for the morphing wings, this thesis aims to give insights into the potential Aero-Acoustic Noise and Radar Cross-Section merits that can be achieved by applying flap morphing. To observe these potential benefits, the following research question is answered:

What are the potential Radar Cross-Section and Aero-Acoustic noise merits of a GA-ASI MQ-9 Reaper by applying flap morphing?

To answer the above-mentioned research question, it is further divided into the following sub-questions.

- What effect does the elimination of gaps, when replacing conventional flaps with morphing surface have on the mono-static and bi-static radar signatures of MQ-9 Reaper?
- How does the Radar Cross-Section vary between the conventional and morphing wings at different radar locations for mono-static and bi-static analyses?
- How does the Radar signature of MQ-9 Reaper vary without i.e. 0° and with 25° trailing edge flap and morphing wing deflections?
- What are the potential noise merits for the 25° trailing edge flap and morphing wing deflections at different angles of attack?
- How does the potential noise merits vary for different Mach numbers?
- How does the adjusted noise prediction simulation models compare to the experimental data for the morphing wing and how does the potential noise merits vary between the predicted and experimental data for both wings?

Study Case Description

With different disciplines involved and each with different requirements, elements studied in each discipline is explained here. After the re-design of the MQ-9 Reaper's wing, during the modelling of the wings 4 different types of CAD models are generated. A conventional wing with 25° flap deflection, morphing wing with 25° trailing edge deflection, conventional wing with no flap deployment i.e. 0° flap deflection and 0° morphing trailing edge deflection i.e. straight wing. All these models are required for the Aero-Acoustic noise and Radar Cross-Section analysis and how these are required by each discipline are explained in the following.

Aero-Acoustic noise

For the Aero-Acoustic noise analysis, experiments and the noise predictions are performed. Experiments are performed on a 3D printed scaled wing of the MQ-9 Reaper at the landing configuration with 25° trailing edge flap and morphing wing deflections. Due to time limitations, 0° trailing edge flap and morphing wing deflections are not analysed.

Radar Cross-Section

In the evaluation of the Radar Cross-Section merits, all four full scaled models are used. For the mono-static RCS analysis, a conventional wing with 25° flap deflection, morphing wing with 25° trailing edge deflection, conventional wing with no flap deployment i.e. 0° flap deflection and 0° morphing trailing edge deflection are analysed and compared to each other whereas for the bi-static RCS analysis only the 0° flap deflection and 0° morphing trailing edge deflection are analysed due to time limitations.

Thesis Approach and Outline

The thesis is split between different disciplines in order to answer the research question. The thesis starts with the re-design of the MQ-9 reaper wing with morphing characteristics. Once all the parameters and planform of the new wing are determined, both wings are modelled in a 3D CAD modelling software. These first two steps are essential in order to proceed with the Aero-Acoustic noise and Radar Cross-Section analyses. Once the first two steps are completed, Aero-Acoustic noise and Radar Cross-Section analysis are treated simultaneously. Figure 1.3 contains the all the steps required to be followed in order to reach the set goal.

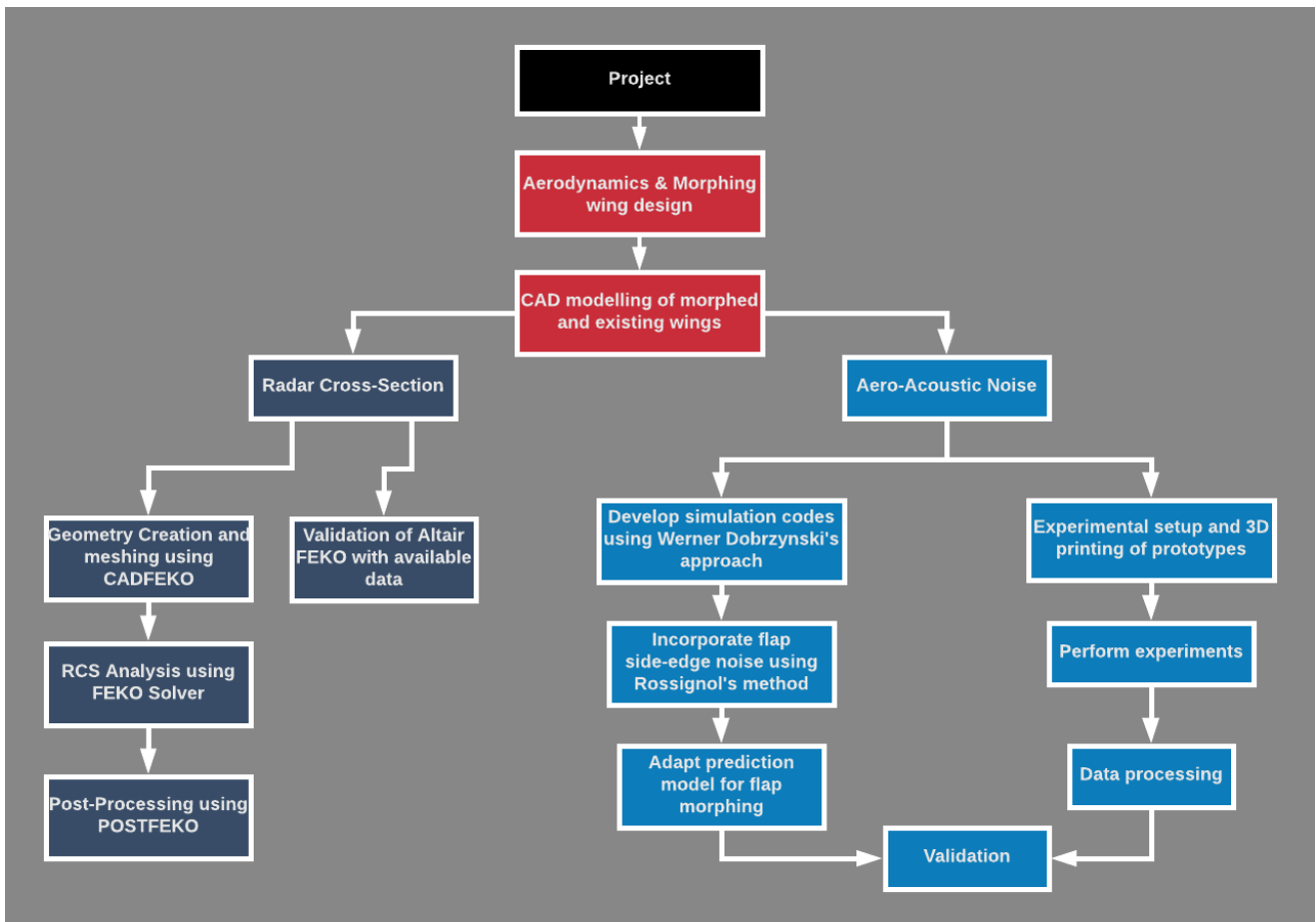


Figure 1.3: Project flow diagram

This work for the last year is summarized in this report. The report is divided into six different chapters. The subject of morphing wings has been introduced in this Chapter. Chapter 2 discusses

the past and current developments in the field of morphing wings and state-of-the-art morphing wing enablers. Chapter 3 explains the design of the morphing wing from MQ-9 Reaper's existing wing and also the CAD modelling of the conventional and morphing wings at different trailing edge deflections for morphing wings and different flap settings for conventional wings. In Chapter 4, experimental and analytical Aero-Acoustic noise prediction analysis on the MQ-9 conventional and morphing wings are discussed. Beamforming maps on the experimental data to visualize the noise sources on the wings and the comparison of the noise predicted data are also part of the chapter. Subsequently, in Chapter 5 theoretical background knowledge of Radar Cross-Section, RCS simulations setup and mono-static and bi-static RCS analysis with different antenna(s) locations are elaborated. Finally in Chapter 6, conclusions are drawn based on the RCS and Aero-Acoustic noise evaluations and the recommendations for the future research on the discussed topic are suggested.

Additionally, Appendix A and B contains a time-line showing the implementation of the morphing wing technologies(along with the type of morphing) on fixed wing aerial vehicles and future of morphing wings in military domain respectively. . Subsequently, additional Radar Cross-Section and experimental Aero-Acoustic noise spectra and beam maps are shown in Chapters C and D respectively.

In addition, the nomenclature used throughout the report is provided. Here, the reader can find all the symbols used, their formal description and units.

2. Background & State-of-the-art Morphing Wing Techniques

There have been some recent developments and advancements in morphing wings/shape-changing structures. Morphing of aircraft wings can be classified into three primary categories namely airfoil adjustment, planform adjustment and out-of-plane transformation [39]. All these categories along with their respected planforms can be found in Figure 2.1.

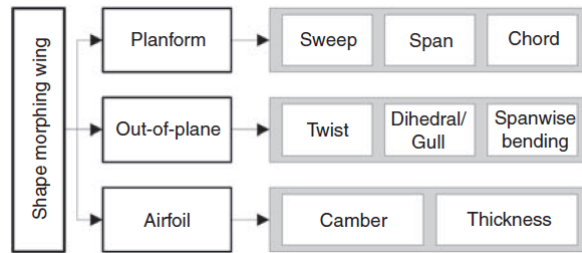


Figure 2.1: Classification of wing morphing concepts

One of the important question that comes to mind regarding this technology is why almost all the aircraft after Wright Brothers' time use conventional discrete flaps or control surfaces instead of having a twisted wing for flight control like Wright Brothers. In order to twist the wing with a reasonable amount of actuation, the wing has to be very light-weight/flexible. Being very light weight and flexible means it flutters very early, which means the aircraft can not fly at high speeds and achieve high Mach numbers.

Now, this possibility can be re-evaluated with the availability of new materials which can twist and can act as actuation devices for themselves. There have been some other projects in the past that tested and applied this technology on the aerial vehicles. Some of these projects along with their respective enablers are discussed in the next section of this Chapter. These do not only contain techniques for flap morphing but also the techniques/methods that are applicable to other type of morphing of wings.

2.1 Overview of Morphing Wing Enablers

In this section, design methodologies and technologies that are used to facilitate wing morphing are discussed. Some of the main technologies discussed in the literature are mentioned here.

2.1.1 Shape Memory Alloy devices (SMA)

In aerospace, Shape Memory Alloys are a kind of Smart Materials that changes their characteristics depending on temperatures. These are actuated by changes in temperature/heat.

An example of such a technology in Aerospace domain is the SMART Wing Program of the Defense Advanced Research Projects Agency (DARPA), The Air Force Research Laboratory (AFRL), NASA and Northrop Grumman. During this project, wing twist along with the leading and trailing edge morphing was implemented by using Shape Memory Alloy devices on an Unmanned Combat Aerial Vehicle. Wing twist was obtained using the SMA torque tubes and the flexible trailing and leading edges were achieved using SMA wires [22][26]. An illustration of chordwise bending obtained by varying the heat on the Shape memory Alloy strips can be seen in Figure 2.2.

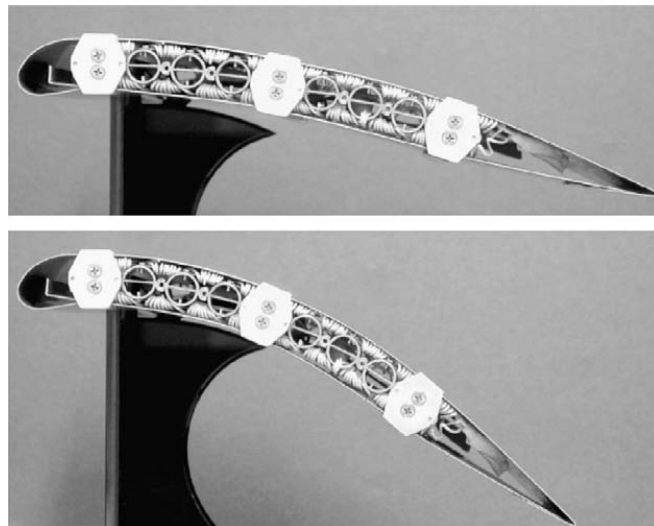


Figure 2.2: Chordwise bending of Unmorphed(top) and morphed(bottom) surfaces achieved by varying heat of SMA strips [16]

2.1.2 Shape Memory Polymers (SMP)

Shape Memory polymers are also in the category of SMART materials, that can change from their deformed shape and return back to their previous (original) shape due of its activation by heat change/-electricity/light. The Aerospace domain did not have much success in the past with Shape Memory Polymers for morphing but with current research and latest developments this possibility can be revisited.

A research group by the name of Cornerstone Research Group tried to vary chord length by using Shape Memory Polymer(Dynamic Modulus Foam) with the objective to achieve 80% increase in lift. Due to the characteristic of SMPs to withstand high stresses, they were preferred and activated through temperature variance. Although the prototype could extend the chord length after being activated, it failed to return to its previous shape due to low stress recovery of SMPs [34].

Another effort to use SMPs for a morphing wing was in 2007 when the prototype was subjected to shear deformation to achieve variable sweep. The wing made from SMPs and composites did rotate from the hinge upon heating but in the process the mechanism was deformed due to hinge rotation [55].

2.1.3 Piezoelectric Actuators (PZT)

Piezoelectric actuators have small size, high power density, high bandwidth and as a result higher output force. Due to these properties, piezoelectric actuators are widely used for aerospace applications. This part of the section is focused on the techniques for achieving wing camber morphing, wing twist morphing and the rigid-body rotation with the use of Piezoelectric Actuators.

Camber

As mentioned earlier, Piezoelectric Actuators produces high force output. These actuators includes Piezobimorphs and Piezoelectric composite-coupled system for flap actuation. Since the early 1990's, several projects have already been successful in applying the Piezoelectric Actuation to obtain leading edge and trailing edge morphing.

One of the recent project which made use of Piezoelectric Actuation was from the Boeing with collaboration of the NASA AMES Research Center. Piezoelectric actuated blade flaps on a smart rotor were used and tested in a wind tunnel which resulted in 80% reduction in the vibrations and almost no vibrations at the hub [47]. Figure 2.3 shows the close-up and front view of the Boeing Smart rotor in the windtunnel. Another type of these Piezoelectric Actuators are the Piezoelectric Bender Actuators. These were used in testing of the Post-Buckled Pre-compressed (PBP) actuators on a scaled UAV where

the wing is deformed to obtain the variation in camber distribution which in return improved the roll control. Improvement in the roll control by 38% and more than 3.5 times improvement in control by replacing the conventional ailerons was observed using these Post-Buckled Pre-compressed actuators [50].

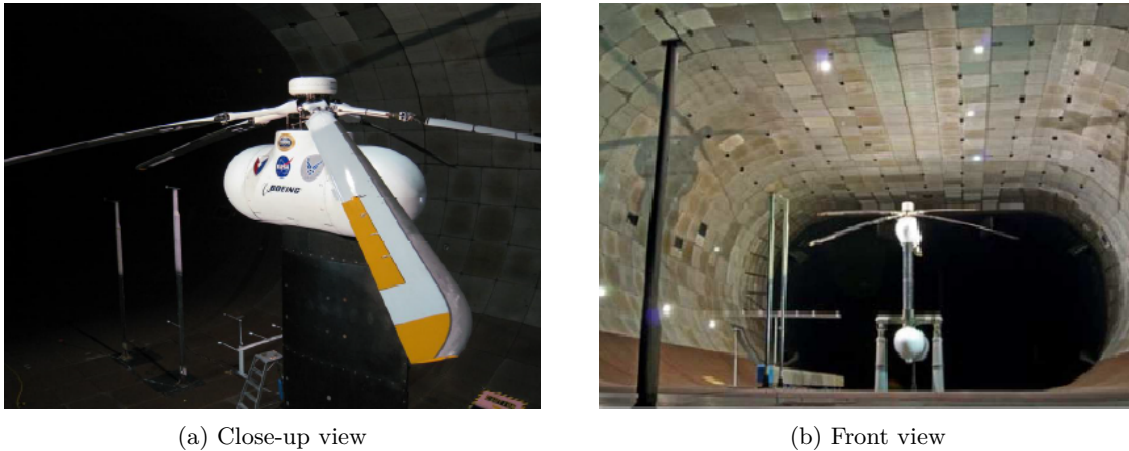


Figure 2.3: Wind tunnel testing of the Boeing Smart Rotor [47]

Twist

One of the first developments in the piezoelectric actuation was presented in 1989 when a graphite-epoxy plate was coupled with bending-twist and were actuated through piezoceramic sheets [13]. As the bending loads were varied, twist on the plate varied as well and because of the coupling, deflections became significant. Later in the same year this technology was applied on the aircraft wings, missiles and rotor blades of the helicopters [7] and their feasibility was also researched upon. It was discovered that the wings and the missile fins coupled with piezoceramic materials resulted in the required deflections for flight control [15].

Rigid-Body Rotation

In 1996, Flexspar stabilator with a morphing wing was introduced which was used to achieve the deflections of about $\pm 30^\circ$ without any aeroelastic behaviour of the material. The structure was rotated about the spar which was actuated by the piezoelectric bi-morph actuator placed inside the skin structure [8].

One of the first aerial vehicle to try this technology was a fixed-wing Unmanned Aerial Vehicle. Rudders and elevators of this Unmanned Aerial Vehicle were controlled through Flexspar [6]. Numerous projects followed this and achieved significant amount of success in applying piezoelectric actuation to achieve the Rigid-Body Rotation.

2.1.4 Active Aeroelastic Concepts for twist

Variation in the twist distribution to obtain better flight performance is an old phenomenon but the quest for achieving better flight performance and higher speeds was limited due to the instabilities (aeroelastic) and loading requirements. This led to the increase in the weight of an aircraft and as a result reduction in the flight performance. With recent developments in aerospace materials and structures and due to the increased demand in the improvement of performance, the interest of aircraft designers has been focused on using aeroelastic behaviour of the materials in a positive way. [51]

One of the first to use this technology was the Rockwell International who pioneered the Active Flexible Wing (AFW) program in late 1980's [28]. This program used the beneficial side of wing flexibility (elasticity) to minimize weight and also tried to minimize the problems associated with the control (aileron reversal) mostly for the Military Aerial Vehicles where dynamic pressures are very high due to high speeds. This technology did not incorporate conventional control surfaces for their primary use which was to produce control force but were used as aerodynamic tabs to control the aeroelastic twist. This

was used to provide the required roll to achieve the lateral stability. Another development in the Active Aeroelastic concept in the use morphing wing appeared where the sweeping movement of the rear spar increases or decreases the amount of wash-in induced by the presence of aerodynamic forces[51]. This was successfully tested on the scaled UAVS.

AFW was followed by the Active Aeroelastic Wing (AAW) program by the United States Air Force and NASA. Active Aeroelastic Wing (AAW) technology was tested on a modified version of a fighter jet namely F/A-18 to check the feasibility of this technology[33][54]. The original F/A-18 wing skin panels(at the rear of the wing) got replaced with more thinner and more flexible wing panels. At the leading edge, division was made between the inboard and the outboard sections. The outboard section of the wing was actuated separately from the inboard section. Together with trailing edge control surfaces the aeroelastic wing twist was controlled and provided enough power for rolling. This was successfully tested as well within the structural limits [12].

There were several other programs which followed Active Aeroelastic Wing (AAW). This includes Active Aeroelastic Structures(AASs), Variable Stiffness Spar(VSS), Active Aeroelastic Aircraft Structures(3AS) European research project, All Moving Vertical Tail (AMVT), 3AS project, Adaptive Torsion Structure (ATS), The DARPA Smart Wing program phase II e.t.c. All these projects with different point of focus researched and also tested the aeroelastic concepts to achieve twist. Detailed methodology of these programs is readily available in the open literature.

2.1.5 Hyper Elliptic Cambered Span (HECS)

Hyper Elliptic Cambered Span concept developed by NASA Langley Research Center is an effective technique to achieve a continuous out-of-plane morphing (span-wise). Two approaches were researched to achieve this type of morphing with this concept. First approach consists of the tendon-based spool system powered/actuated by a DC motor. An illustration of such a system is shown in Figure 2.4[24].

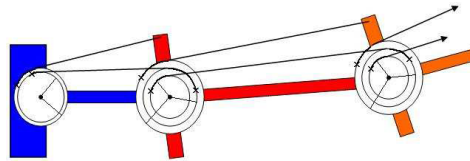


Figure 2.4: Tendon-based spool system for Hyper Elliptic Cambered Span concept

The second approach uses Shape Memory Alloys actuated mechanism that was powered by a closed-loop feedback control in tandems [25]. Feasibility of such structures to continuously morph a wing to its non-planar shape was determined by using a repeating quarterly-binary link(scissor-like) configuration which was used to translate motion of one segment onto the next one [53].

A similar concept to the HECS was researched upon where the wing could flex laterally in a continuous fashion. This prototype was made by carbon-epoxy and was actuated through the Shape Memory Alloys(SMA) similarly to the second approach of HECS. This prototype showed very good behaviour of the mechanism under different loads. It also showed significant advantages in the aerodynamics and power consumption of the UAV [45].

2.1.6 Dihedral/Gull actuation

Dihedral or gull wings attracted much interest due to their ability to improve aircraft performance and also significant improvement in the flight control.

A study on the characteristics and dynamics of Micro Aerial Vehicles(MAVs) have been done before in which the wing was divided into inboard and outboard sections. These sections were separated using a hinged spar structure and the dihedral angle at the partitions were varied [3].

One of the most important research/advancement in this category is the Z-wing developed by the

Lockheed Martin. Methods/enablers used to develop Z-wing are discussed below.

Lockheed Martin Z-Wing

Z-wing is the folding wing developed by the Lockheed Martin as part of The Morphing Aircraft Structures (MAS) program. Sweep angle, aspect ratio and the wing span may be varied for this Z-wing [43].

Figure 2.5 illustrates this Lockheed Martin Z-Wing for varied span, aspect ratio and sweep.

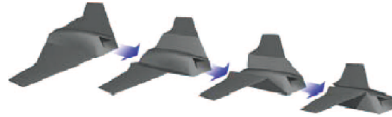
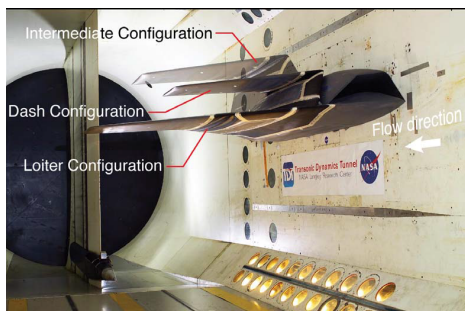


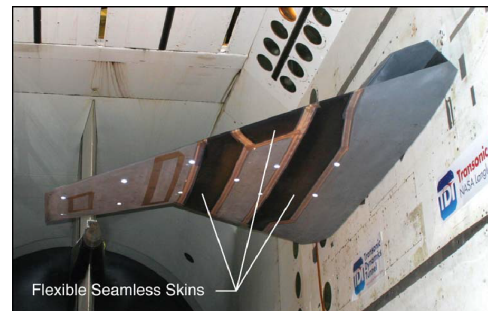
Figure 2.5: Lockheed Martin Z-wing

A couple of approaches were researched upon for the folding of the Z-Wing. In the first approach, a thermo-polymer actuator was chosen to operate the helical spline gear but due to the high risk associated with the helical spline gear, electro-mechanical rotary actuators were used [11]. In the second approach, whole wing was covered with elastometric skins which enabled the shape changes.

Figure 2.6[18] shows the Z-wing during wind tunnel testing. The Z-wing was successfully flight tested as well.



(a) Front view for different configurations



(b) Underside view for loiter configuration

Figure 2.6: Wind tunnel testing of the Z-Wing

3. Redesign of the MQ-9 Reaper Wing

In this chapter, geometrical properties of the MQ-9 Reaper, re-design of the MQ-9's morphing wing and the 3D CAD modelling of the conventional and the new morphing wing are explained.

Geometrical properties of the MQ-9 Reaper wing were at first gathered and the wing planform was constructed. In order to determine the sizing of the morphing wing, availability of wing geometrical data of conventional wing is essential. Sizing of the morphing wing is based on obtaining similar lifting performance characteristics as of the conventional wing. The relation is stated below.

$$S_{morphed} \cdot C_{L_{maxMorphed}} = S_{conventional} \cdot C_{L_{maxConventional}}$$

As the potential Aero-acoustic noise and Radar Cross-Section merits are being analysed, therefore it is required to model the existing wing of MQ-9 as well. Both wings were modelled using CATIA.

3.1 Geometrical Properties of Conventional MQ-9 Reaper

In this section, wing geometrical properties of the conventional MQ-9 Reaper are determined. Some properties may not be known due to the sensitive nature of the aerial vehicle due to its usage in military purposes. Most of the geometrical properties for its planform were gathered from the book *All the Worlds Aircraft: Unmanned* and from a report from NASA about the MQ-9 Reaper/Predator B. According to the NASA report, wings of the MQ-9 Reaper are equipped with redundant single-slotted fowler flaps.

Due to confidentiality reasons, some parameters of MQ-9 were not easily available to work with. Leading and trailing edge sweep angles of the older version of MQ-9 were used for this case as no information was available. Airfoil coordinates of the wing were not available as well. In one of the online forums Prof. Mark Drela mentioned the airfoil is very similar to NASA/Langley LS(1) - 0417, therefore the airfoil NASA/Langley LS(1) - 0417 was assumed for the wings as it was not possible to obtain the exact coordinates.

All the required geometrical properties of the conventional wing are assembled in Table 3.1.

Table 3.1: Geometrical parameters of the existing MQ-9 Reaper

Parameter	Value	Unit
Root chord	1.74	[m]
Tip chord	0.86	[m]
Taper ratio	0.494	[m]
Leading edge sweep	4	[°]
TE sweep	1.3	[°]
Wing span	18.99	[m]
Flaps span	51.1	[%]
Dihedral	2	[°]
Wing aspect ratio	14.6	[-]
Wing area	24.69	[m ²]

3.2 Sizing of the Morphing Wing

New design of the wing is based on the textbook approach in order to satisfy the performance requirements. Before morphing wing is sized, lift capabilities of the existing conventional wing needs to be determined. This includes the maximum lift capabilities during landing where flap extensions and

deflections are highest.

The existing wing of MQ-9 is equipped with redundant high lift devices, which means that high lift devices are not required for landing and take-off operations. High lift devices are present in order to reduce the stopping distance after landing where there is shorter landing field length is available. High lift devices reduce the approach speed which in return reduces the stopping distance of the aircraft. Flap chord and the maximum flap deflection for the equipped flaps is not available in the open literature. Therefore, a maximum flap extension is assumed to be 25° and flap chord is assumed to be 20% of the total chord length. Due to the redundant high lift devices on the conventional wing, a 25° single-slotted fowler flap deflection is justified.

Based on all the available information discussed above, lift computations were carried out for the conventional wing.

Wing lift contribution in conventional wing

For the wing and flap contribution to lift, maximum 3D lift coefficient of the wing is determined at first followed by the computation of the 3D lift contribution of flaps. Summation of these two quantities provide the overall/total maximum lift capability of the wing.

Figure 3.1 contains the lifting characteristics for different angles of attack of NASA/Langley LS(1) - 0417, morphed NASA/Langley LS(1) - 0417 at 10° trailing edge deflection and morphed NASA/Langley LS(1) - 0417 at 25° trailing edge deflection. These characteristics were determined using XFOIL¹, an open source airfoil design and analysis software. These lift computations were based on the Reynolds number of about half a million determined for the landing configuration. From Figure 3.1, maximum 2D lift coefficient of straight NASA/Langley LS(1) - 0417 is **1.905** at an angle of attack of 20° .

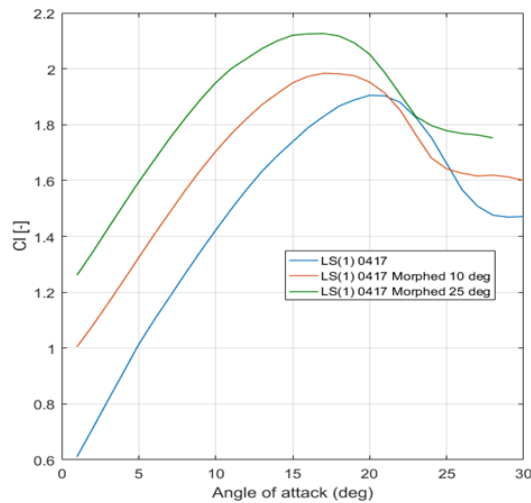


Figure 3.1: $cl - \alpha$ curves for LS(1)-0417 and its morphed version for two different deflection angles

These lift characteristics and values for NASA/Langley LS(1) - 0417 were validated with the experimental data from NASA with the experimental values and the analysis very similar and close to each other [27]. With this validation, it was assumed that the analysis by XFOIL are valid for the morphing wing as well as no experimental data is available for morphing NASA/Langley LS(1) - 0417.

DATCOM method by Raymer [36] is used to determine the 3D lift coefficient from the 2D lift coefficient. Equation 3.1 is used to determine the 3D lift coefficient due to only wing without any contribution from the flap. In the equation $C_{l_{max}}$ term is already known as determined before to be 1.905.

¹URL:<http://web.mit.edu/drela/Public/web/xfoil/> [Cited 14-Apr-2018]

$$C_{L_{max}} = \left[\frac{C_{L_{max}}}{c_{l_{max}}} \right] \cdot c_{l_{max}} + \Delta c_{l_{max}} \quad (3.1)$$

At landing or take off speeds the Mach number is lower than 0.2 meaning that no compressibility effects exists. Therefore, the term $\Delta C_{l_{max}}$ which accounts for the effect of Mach number higher than 0.2 is not relevant. Ratio between $C_{L_{max}}$ and $C_{l_{max}}$ is determined using 3D to 2D maximum lift coefficient ratio by Raymer based on the airfoil sharpness factor and the leading edge sweep angle.

ΔY is a measure of the sharpness of an airfoil. It is the difference in the height of the airfoil between 1.5% and 6% of the chord length. The sharper the LE, the higher the intensity of the generated leading edge vortices leading to higher $C_{L_{max}}$. The shape of the upper part of the airfoil, near the leading edge, is mostly responsible for the formation of these vortexes.

After determination of ΔY , all the parameters are available to proceed with the computation of the 3D wing lift contribution. These parameters were used as inputs in Equation 3.1 with which the final 3D maximum lift coefficient due to the wing is determined to be **1.73**.

Flap lift contribution in conventional wing

To determine the overall maximum lift coefficient, contribution to lift from the wing and flaps both are required. Wing contribution to the maximum 3D lift coefficient has already been determined. The method to determine flap contribution to the overall maximum lift coefficient is discussed here.

Methods developed by Torenbeek[48] are used in determining the contribution to maximum lift coefficient by flaps. Equation 3.2 is used in determining the 3D maximum lift coefficient.

$$\Delta C_{L_{max}} = 0.9 \cdot \Delta c_{l_{max}} \cdot \frac{Swf}{S} \cdot \cos(\Lambda_{hinge-line}) \quad (3.2)$$

The flapped area (Swf) is not the actual area of flaps. The reference wing flapped surface (Swf) is the spanwise portion of the reference wing area (S) affected by the presence of a certain type of HLD. There is a different reference wing flapped surface defined for each type of HLD that is installed on the wing.

Flap hinge angle value is generally based on the position of the support spar (the back spar) used to attach the flaps. The flap hinge line is likely to be parallel to the spar to which it is attached. If the wing has a trailing edge chord extension, and an extra support spar is used to hinge the flaps, it is likely that the hinge line will have null sweep angle, or a much lower sweep than the “regular” wing spars just because the extra support spar has a zero or lower sweep. For this case it is assumed that the flap hinge angle is set to zero.

As mentioned before, the $\Delta C_{l_{max}}$ in the equation is determined for single slotted fowler flaps. Table 3.2 contains different types of trailing edge devices and their overall contribution to wing lift when in operation. c'/c is dependent on flap type and deflection. According to a technical report from the General Atomics, MQ-9’s wings with single-slotted fowler flaps extends up to 51.1% of the total wing span [1].

Table 3.2: Increase in maximum lift coefficient for different types of flaps

TE High-lift device	$\Delta C_{l_{max}}$
Plain and Split	0.9
Slotted	1.3
Fowler	1.3 c'/c
Double slotted	1.6 c'/c
Triple slotted	1.9 c'/c

From Table 3.2, $\Delta c_{l_{max}}$ contribution for a single-slotted fowler flap is 1.3 c'/c which can be re-written as in Equation 3.3.

$$\Delta c_{l_{max}} = 1.3 \cdot c' / c \quad (3.3)$$

Figure 3.2 define both chord lengths c and c' . c' is the chord length after the flap extension.

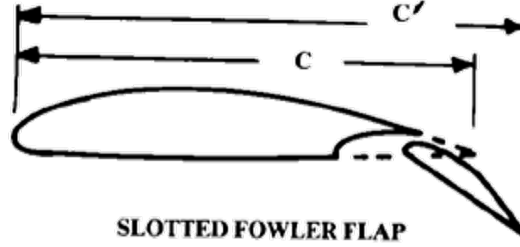


Figure 3.2: Single slotted fowler flap extension and deflections with corresponding chord lengths

c' can be re-written as sum of the original chord length (c) without any flap extension and the change in chord length after flap extension. c' is the chord length of the wing section when the HLD is deployed. It is defined parallel to the wing section chord. It is determined using Equation 3.4.

$$c' = c + \Delta c \quad (3.4)$$

$\Delta c / c_f$ is estimated using Figure 3.3 where c_f is the part of the wing section chord taken by the HLD.

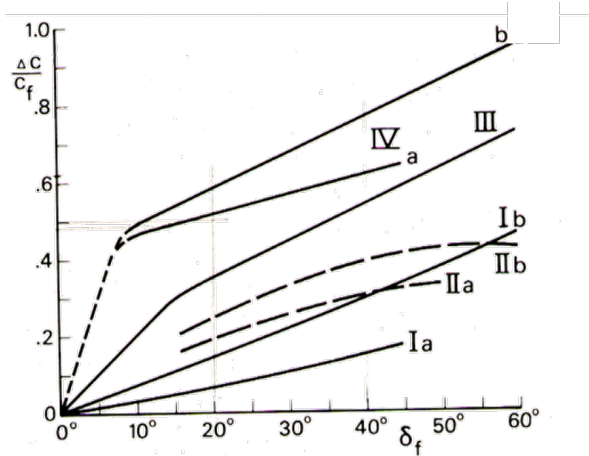


Figure 3.3: Geometrical properties of existing MQ-9 Reaper [48]

- I. Fixed hinge - a: $z_h/c_f = 0.2$ & b: $z_h/c_f = 0.4$
- II. Typical optimum flap position - a: single slotted & b: double slotted
- III. Double slotted with variable geometry, with flap extension
- IV. Fowler - a: single slotted, double slotted with fixed vane & b: double and triple slotted, with flap extension

$\Delta c / c_f$ is estimated for flap angle deflection of 25° which is assumed maximum for this design. The type of flap as mentioned earlier is a single-slotted fowler flap which is $4a$ in Figure 3.3.

Δc is determined from the figure with c_f already known and input into Equation 3.4 from where c' is computed which then leads to the computation of $\Delta c_{l_{max}}$ using $1.3 c' / c$. The value of $\Delta c_{l_{max}}$ due to

flaps is computed to be **1.46**.

2D lift($\Delta c_{l_{max}}$) contribution from the flaps is then used in Equation 3.1 to compute the 3D lift coefficient for the flap contribution. The 3D lift coefficient is computed to be **0.78**.

The 2D and 3D coefficients from both the wing and the flap contribution is shown in Table 3.3. Overall total maximum 3D lift coefficient is also determined in the table.

Table 3.3: 2D and 3D lift contribution from the wing and the flap

Surface type	$c_{l_{max}}$	$C_{L_{max}}$	Total max. 3D Lift coefficient
Wing	1.905	1.73	2.51
Flap	1.456	0.78	

Morphing Wing lift

Before the new morphing wing can be re-sized, it is necessary to determine the amount of lift produced by morphing the existing wing. Morphing wing must be able to produce similar amount of lift as the conventional wing to match the lifting performance requirements. The following relation in Equation 3.5 is used to determine the surface area of the morphing wing.

$$S_{morphed} \cdot C_{L_{max_{Morphed}}} = S_{conventional} \cdot C_{L_{max_{Conventional}}} \quad (3.5)$$

Morphing span percentage and the flap span percentage to the total wing span is kept same i.e. 51.1%. For the morphing wing two different airfoil sections exist. Inboard wing (morphed part) will consist of a morphing NASA/Langley LS(1) - 0417 airfoil whereas the outboard wing will consist of straight NASA/Langley LS(1) - 0417. Morphing section of the airfoil with 25° trailing edge deflection stalls at an angle of attack of 17° with maximum 2D lift coefficient of 2.13 whereas the outboard airfoil section stalls at an angle of 20° with maximum 2D lift coefficient of 1.905. These lift coefficients can be found in Figure 3.1. In this situation combination of the maximum lift coefficient from both sections of the wing can not be obtained as the morphed part of the wing stalls earlier than the outboard wing. Therefore, in the analysis maximum angle of attack for outboard section of the wing is set to be same as morphed part i.e. 17° where its lift coefficient is 1.83. By using this approach both sections of the wing will stall at the same angle of attack.

The overall 2D lift coefficient for morphed wing is computed by using the following relation in Equation 3.6.

$$c_{l_{max_{morphed-wing}}} = \frac{S_{wing_{inboard}} \cdot c_{l_{max_{morphed}}} + S_{wing_{outboard}} \cdot c_{l_{straight@17^\circ}}}{S_{wing_{inboard}} + S_{wing_{outboard}}} \quad (3.6)$$

After the 2D lift coefficient is determined for morphing wing, 3D lift coefficient is computed using the same method as the conventional wing in Equation 3.1. The airfoil sharpness factor is same in both cases meaning the ratio $\frac{C_{L_{max}}}{c_{l_{max}}}$ is the same and as mentioned before $\Delta c_{l_{max}}$ term accounts for the effect of Mach numbers higher than 0.2 so this term is not relevant at landing speeds or take off. In this case it is equal to zero as there exists no compressibility effects.

The computed 3D lift coefficient for the morphed wing is **1.827**. It can be noticed there exists a big difference between the 3D lift coefficients of the conventional and morphing wing. Maximum 3D lift coefficient of conventional wing is 2.51 and for morphing wing it is 1.827 meaning that to compensate for the extra lift coefficient surface area of the morphing wing needs to be increased. Using Equation 3.5 morphed wing area is determined to be $33.97m^2$. By increasing the area of the wing to $33.97m^2$ for the morphing wing (morphed inboard wing and straight outboard wing) similar lifting performance characteristics can be achieved as the conventional wing.

As there exists a big difference between the lift produced by the morphing wing and the conventional configuration (wing + flap), effect of circulation is an important phenomenon that lie behind this increase

in the effectiveness of the trailing edges of the conventional configuration. When flow washes over a component it leaves a wake on the succeeding component with a high possibility of this wake mixing with the boundary layer of the element (confluent boundary layer). The wake consists of the flow with very low momentum (energy) which reduces effectiveness of the component. With some distance between the elements this confluent boundary layer phenomena can be avoided which in return increases the lift of the succeeding element. This gap increases the region with potential flow between the boundary layer and the wake. By avoiding mixing of these two off the surface pressure recovery is obtained through which there is no momentum loss in the boundary layer of the succeeding element.

New planform for morphing wing

After a surface area value is computed for the morphing wing, the rest of the planform values follows. Taper ratio(λ) is defined as c_t/c_r which can be re-written as $c_r = c_t/\lambda$. Taper ratio and aspect ratio of the wing are kept constant (same as conventional wing). Also the dihedral angle of the wing and leading and trailing edge sweep angles were kept same. The flap span now becomes morphing span i.e. 51.1%.

Equations 3.7 and 3.8 were then used to determine the wing span and the root chord of the new morphing wing. There are two unknowns and two equations which are then solved simultaneously to obtain these parameters.

$$S = 2 \left\{ \frac{1}{2} \left[\frac{b}{2} (c_r + c_t) \right] \right\} \quad (3.7)$$

$$A = \frac{2b}{c_r(1 + \lambda)} \quad (3.8)$$

After determining the wing span and the root chord of the wing, tip chord using the taper ratio and wing span can be determined as well. Table 3.4 contains all the parameters of the new wing along with the parameters that were kept constant during the design of the new morphing wing.

Table 3.4: New MQ-9 morphing wing planform

Parameter	Value	Unit
Root chord	2.04	[m]
Tip chord	1.01	[m]
Leading edge sweep	4	[°]
TE sweep	1.3	[°]
Wing span	22.27	[m]
Morphing span	51.1	[%]
Dihedral	2	[°]
Wing aspect ratio	14.6	[-]
Wing area	33.97	[m ²]

All parameters for the new morphing wing have been determined sufficiently to construct the wing planform. The planform for the conventional wing and the new morphed wing can be found in Figure 3.4. Chord lengths of the wings lie on the Y-axis of the graph whereas span of the wings lie at the X-axis. Only half of the wings i.e. semi-spans have been plotted in the figure.

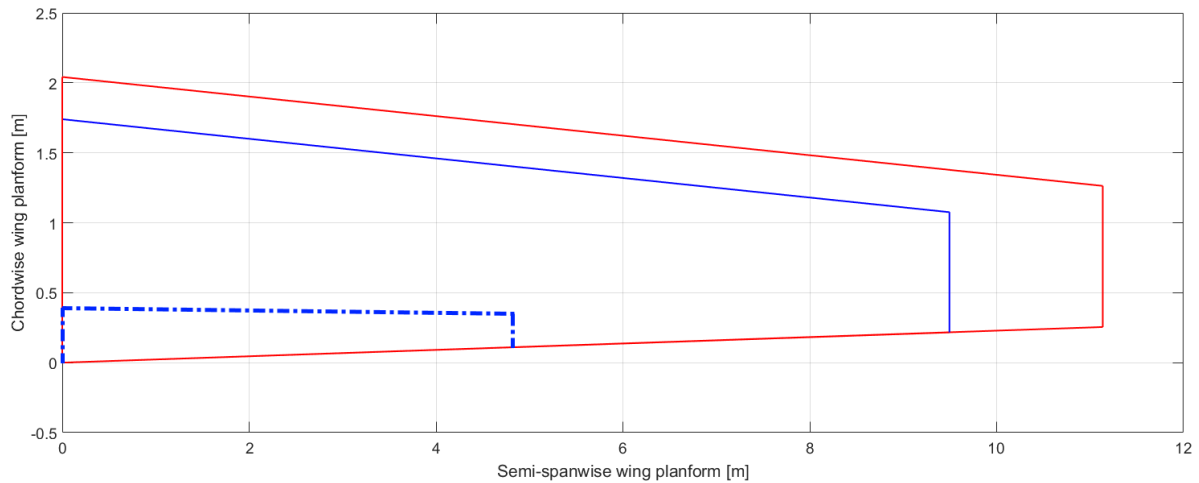


Figure 3.4: Conventional wing(blue) and the new morphing wing planform(red)

3.3 CAD modelling of the Wings

In this section of the report, CAD modelling of the conventional wing and the morphing wing is discussed. CAD models generated here are used later for 3D printing and Radar Cross-Section analysis. 3D printed models are used in the noise experiments whereas Radar Cross-Section analysis are based on the simulations using the models developed in this section. Both CATIA V5 and V6 were used in the modelling of these wings. The dimensions and planform for these models is based on the parameters from the previous two sections.

(Please note: Files generated with V5 can be opened with both versions whereas files generated with V6 can only be opened with V6)

3.3.1 Conventional

For the conventional wing, the wing without flap is constructed first followed by the flap design. These two are then assembled together. Only the semi-span wing is constructed which can be mirrored to obtain full wing if required.

Wing without flap

Airfoils are imported at different sections of the wing within CATIA using GSD². Airfoil points need to be imported manually in the GSD sheet where MACROS scans through all the points and exports them to the CATIA.

For the wing without flap, four different airfoil sections were imported into CATIA. One at the wing root and it is also the point where flap span starts, second at the point where flap span ends i.e. at 51.1% of the span. Only 80% of the chord is imported at these two points as the rest of the 20% is taken by the flaps. At 80% of the chord length, a separate spline is used to close down the airfoil section. The dihedral angle and leading and trailing edge sweep angles are also taken into account when importing the airfoil coordinates by adding a certain offset in both Z and X direction in CATIA. The third airfoil section is imported right next to the second airfoil section where the flap ends. This airfoil consists of 100% of the chord length as no flap is present after 51.1% of span. The fourth airfoil is the tip airfoil of the wing. The surface between the first two and the last two airfoils is generated using *Multi-Sections Surface* which consists of two surfaces through which a solid surface is formed using *Multi-Sections Solid*.

Render

The render of the wing without flap is generated after the solid surface is formed using all four airfoils. This render of the wing without flap can be found in Figure 3.5.

²URL:<https://www.intrinsys.com/blog/2016/creating-multiple-points-in-catia-v5-using-microsoft-excel>
[Cited 18-Apr-2018]

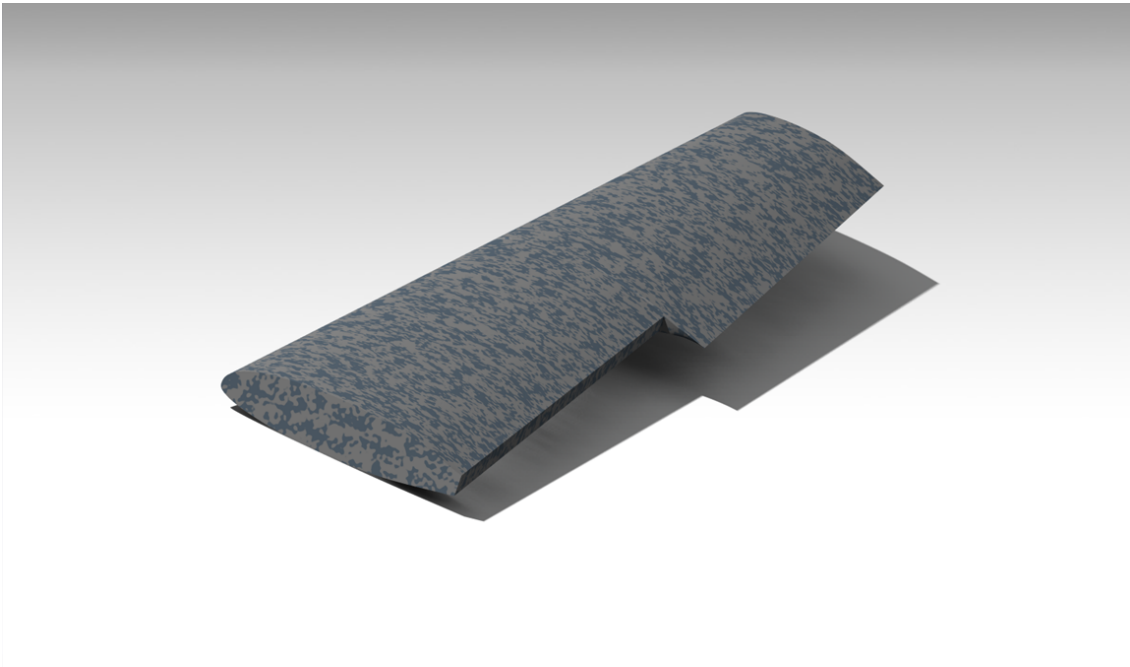


Figure 3.5: Render of the conventional MQ-9 Reaper without flap attachment

Only the semi-span of the wing can be seen in the figure to better visualise the remaining area where the flap of the wing is going to be assembled.

Flap Design

As mentioned earlier, the wing of MQ-9 reaper is fitted with a single slotted fowler flap but no more details about the flap or the flap track mechanism are provided. Therefore, the flap for the wing is designed according to the single slotted fowler flap for the Boeing 747SP due to availability of its detailed flap mechanism layout. The Boeing 747SP is very similar to the Boeing 747-100 but has more simpler flaps, shorter fuselage and bigger tail. The flap of 747SP can be found in Figure 3.6, where the top image shows the flap without any chord extension. In the bottom image, the flap chord is first extended followed by the chord deflection.

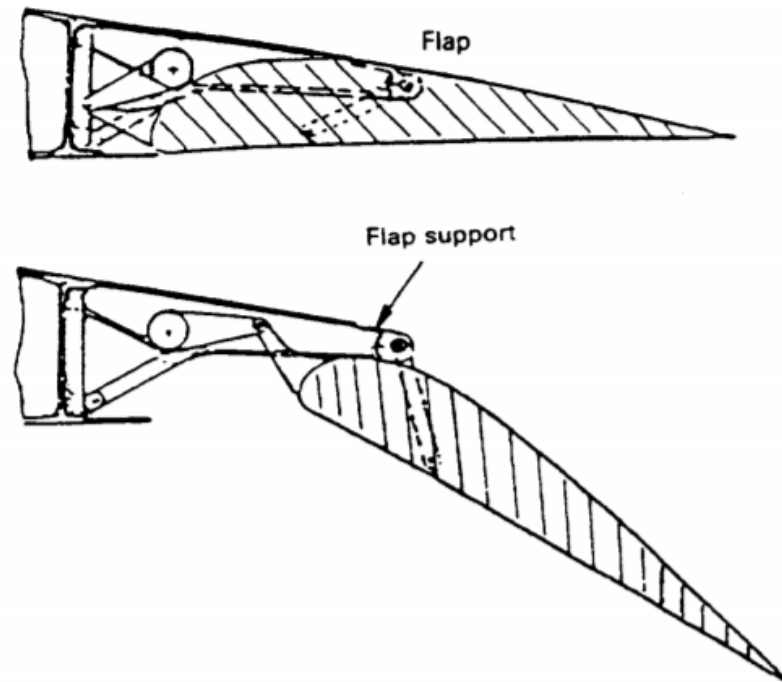


Figure 3.6: Flap layout for the Boeing 747SP for two different configurations [38]

These images also give an idea of the mechanism used in the chord extension and deflection of the flap. The flap was designed using CATIA where the dimensions and parameters of the flap have been adjusted to the MQ-9 wing requirements.

Flap kinematics for the wing were designed for the flap where the chord is first extended and then deflected according to the given input. These inputs could range between 0° to 60° , but only two deflections are used for the analysis in the upcoming chapters. The first case is the 0° flap deflection without chord extension, whereas the second case has a chord extension and a 25° flap deflection.

Render

Renders of the designed flap of MQ-9 are shown in this part of the chapter. Figure 3.7a shows the designed flap for the MQ-9 with no chord extension or deflection. In Figure 3.7b, the same flap with chord extension can be seen. It is at a point where the flap chord extension is maximum and after which flap is deflected to a certain angle. The figures demonstrate both the extension of the flap track mechanism and the deflection of the flap.

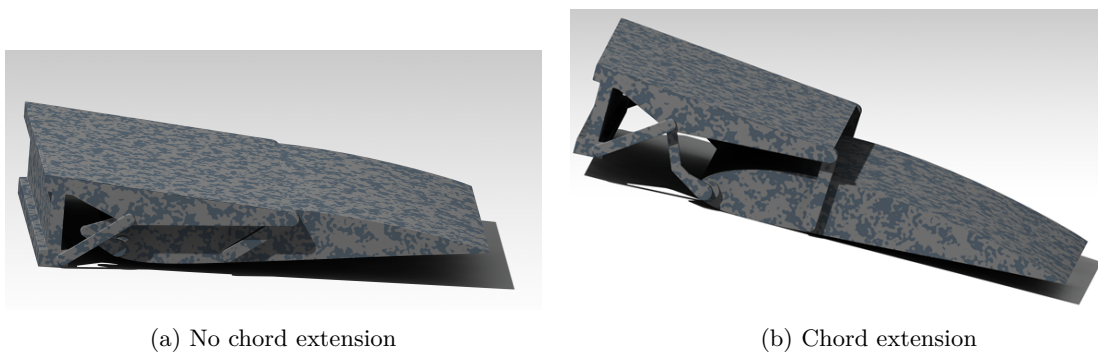


Figure 3.7: Render of the designed morphing MQ-9 Reaper with and without chord extension

Figure 3.8a shows the designed flap for the MQ-9 Reaper deflected to a certain angle. Just for comparison with an actual flap of a wing, the Boeing 747SP flap deflection can be seen opposite to this figure in Figure 3.8b. From the figures it can be noticed that the flap mechanisms and their kinematics for both designs are very much similar to each other.

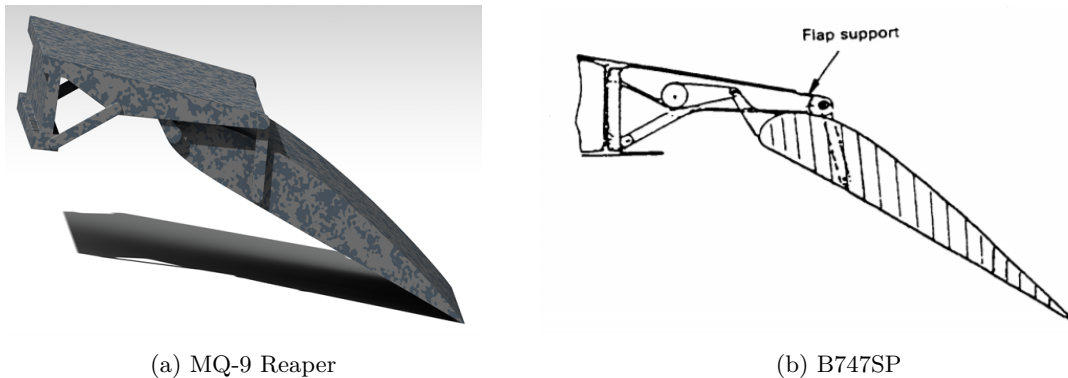


Figure 3.8: The designed morphing MQ-9 Reaper and the Boeing 747SP with flap deflections

Below in Figure 3.9, a different view of the MQ-9 flap deflection to a certain angle can be seen.

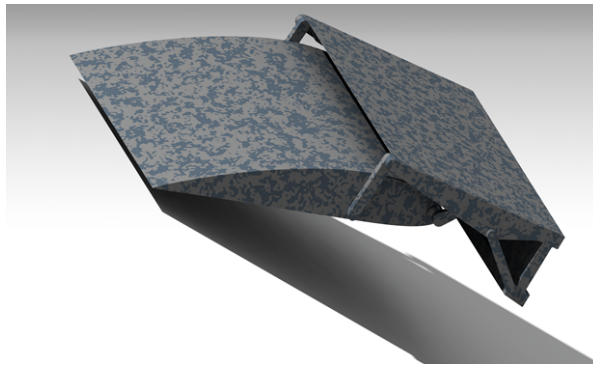


Figure 3.9: Another rendered view of the designed MQ-9 Reaper with the flap deflection

Wing and flap assembly

The assembly can be performed now as the wing without flaps as well as the flap have been designed separately. This assembly procedure is discussed in this part of the Chapter. The flap for the wing was re-sized according to the requirements of the MQ-9 wing. As there exists a certain taper ratio for the wing, the flap for the wing was also tapered accordingly to fit with the chord length along a certain span-wise position. As mentioned earlier, the flap chord is 20% of the total chord length at all span-wise positions until where the flap stops outboard (51.1% of total span). Due to this taper ratio, the flap size and the kinematics of flap were adjusted to provide same flap deflection across the span when a certain flap deflection value is provided.

A line drawing of the wing and flap assembly can be seen in Figure 3.10.

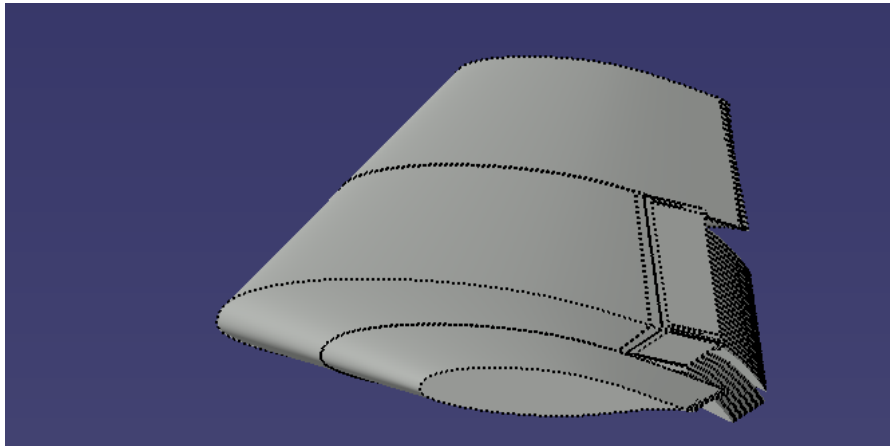


Figure 3.10: Line drawing of the wing and the flap assembly

Render

The render of the wing and flap together can be seen in Figure 3.11. The wing and the flap were designed only for the semi-span, after which the semi-span wing was mirrored in CATIA resulting in a full span of the wing. Flaps have been deflected to 25° in the figure.

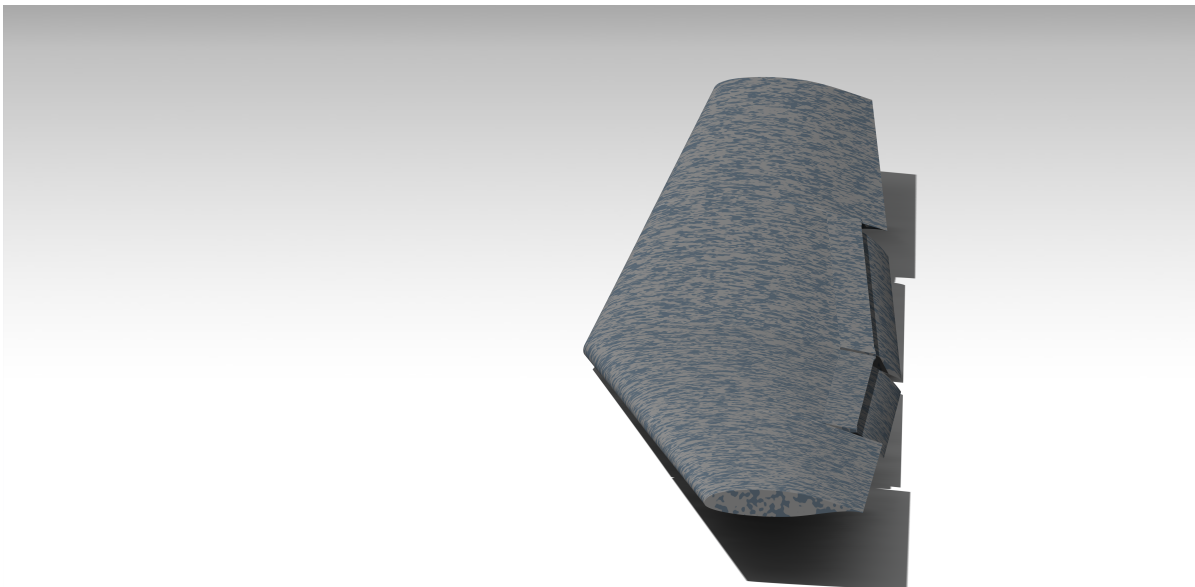


Figure 3.11: Render of the modelled conventional MQ-9 Reaper wing with the flap attachment

3.3.2 Morphed

Dimensions determined in Table 3.4 for the morphing wing were used in the wing modelling. The morphing wings with two different configurations of 0° and 25° trailing edge deflections were designed. For the 0° only the root airfoil and the tip airfoil were required and imported into CATIA. The wing was modelled out of these two airfoils. For the wing with 25° trailing edge deflection a transition surface between the inboard(morphed) and outboard(straight) wing was constructed. Reason for this is in Figure 3.12³ where the trailing edges are morphed but side edges are still present in the design. These side-edges as mentioned before contribute significantly to noise and also scattering in the radar. The motivation to have a transition surface is to avoid these side-edges and the disadvantages that comes

³URL:<https://www.popularmechanics.com/flight/a23703/flexible-composite-wings-morph-into-different-shapes/> [Cited 24-Apr-2018]

with it.

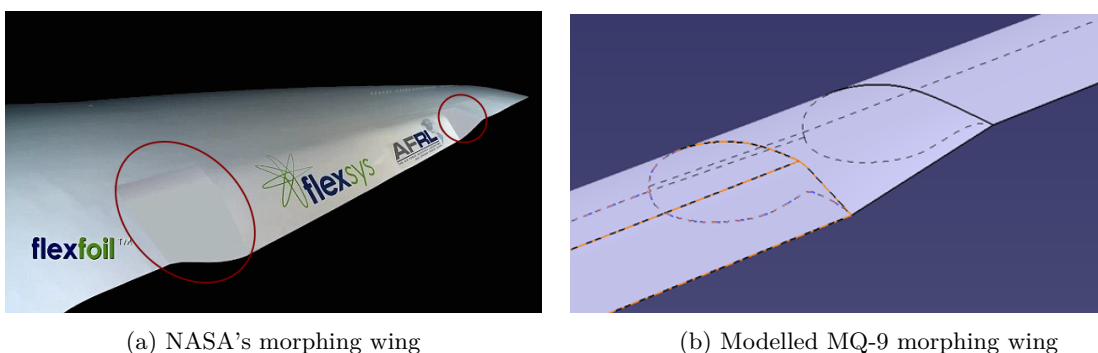


Figure 3.12: Flexsys morphing wing concept with side-edges highlighted

NASA and the US AFRL (Air Force Research Laboratory) already have successfully flight tested a morphing and straight trailing edges of a wing with a transition surface. Flexsys developed this technology and claims significant drag reduction, fuel savings and reduction in the airframe noise.⁴

This wing can be seen in Figure 3.13a⁵ where the trailing edge of the wing is deflecting downwards and the high lift devices have been replaced. This wing is shown in Figure 1.2 and has been flight tested by NASA. The transition surface is made of an elastic surface where it adjusts itself according to the provided deflection input. In the case of MQ-9 flap morphing, only the 25° is used for analysis, therefore these material considerations were not taken into account.

For the 25° trailing edge deflection, four different airfoils were required. First at the root of the wing which is deflected at 25°, second at the 51.1% of the span which is also deflected downwards by 25°. The third and fourth airfoil are straight airfoils for the outboard wing but a transition surface of 0.5m lies between the second and third airfoil. This transition surface gradually bridges the gap between the deflected and the straight surface of the wing. This can be seen in Figure 3.13b where this phenomenon is illustrated.



(a) NASA's morphing wing

(b) Modelled MQ-9 morphing wing

Figure 3.13: Gap bridging between the deflecting trailing edges and the outboard wing for NASA morphing wing concept and the modelled MQ-9 morphing wing

⁴URL:<https://www.flexsys.com/flexfoil/> [Cited 24-Apr-2018]

⁵URL:<http://www.wpafb.af.mil/News/Article-Display/Article/818757/flight-tests-conclude-for-shape-changing-aircraft-flap/> [Cited 24-Apr-2018]

Between the second and third airfoil, airfoil points of first 80% of the chord are connected as usual, whereas the airfoil points of last 20% connects in a slope which merges both airfoils (*It is necessary to have same number of airfoil points for each airfoil to obtain this in CATIA*). In figure 3.14, the semi-span of the morphed wing during design in CATIA can be seen. The deflected and straight airfoils are both highlighted in the figure. The black line indicates the starting point of the deflection point.

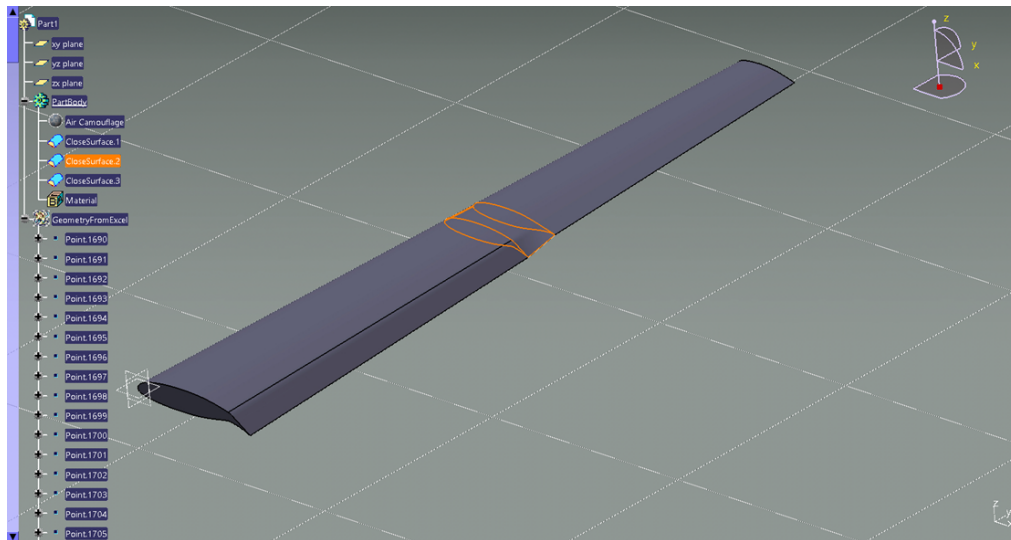


Figure 3.14: Modelling of the MQ-9 morphing wing in CATIA with transition surface airfoils highlighted

A line drawing of the final designed morphing wing can be seen in Figure 3.15.

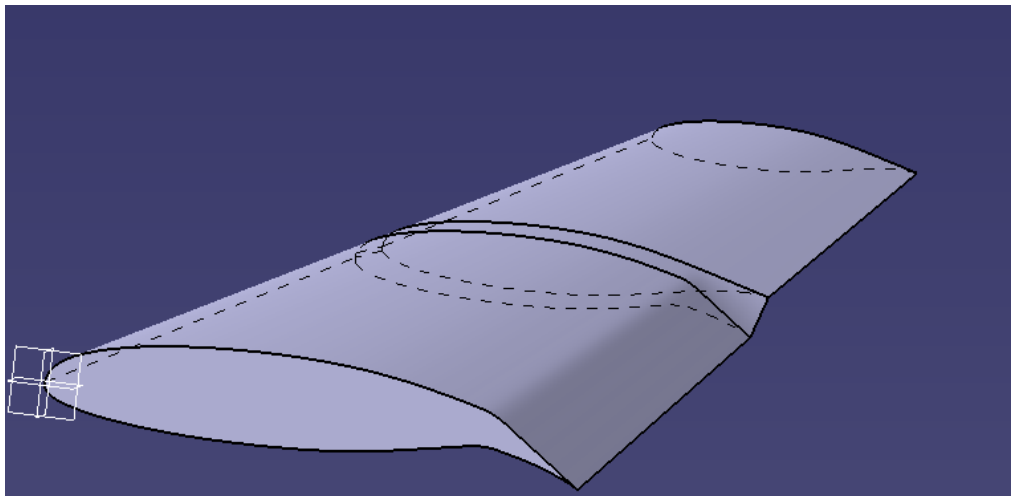


Figure 3.15: Line drawing of the morphing wing

In the figure, it can be seen that the morphed wing is one single surface without presence of any gaps or joints. This is expected to have lower noise generation and lower scattering in the radar.

Render

A render of the morphed wing was generated after its modelling was finished. It can be seen in Figure 3.16. This render was generated for trailing edge deflection of 25% and the transition surface can also be noticed in the figure.

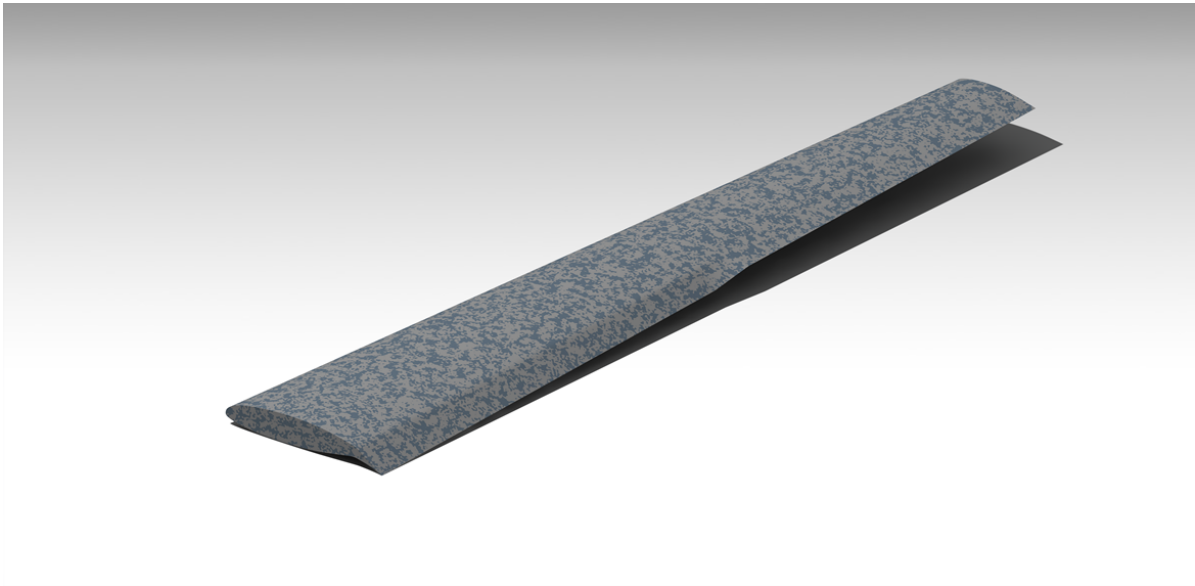


Figure 3.16: Render of the morphed wing with a trailing edge deflection of 25°

4. Aero-Acoustic Noise Analysis & Evaluation

In this chapter, Aero-Acoustic noise analysis on the morphed and conventional wings are discussed. These analyses include the experimental work as well as the analytical work. Experiments are performed on the 3D printed scaled wing designs of the MQ-9 Reaper at the landing configuration with 25° trailing edge flap and morphing wing deflections. As mentioned before, due to time limitations, 0° trailing edge flap and morphing wing deflections are not analysed.

This chapter starts with describing some of the important metrics that are used in acoustics followed by the experimental work performed in order to determine the noise merits. This includes the scaling and 3D printing of the MQ-9 Reaper's wings followed by the test setup which also includes calibration of the microphones along with the description of the facility. This is followed by the experimental results and their analyses. To be able to locate the noise sources on the wings, beamforming on the microphone array data is done. This includes the mathematical approach of the Conventional Beamforming and the Point Spread Function and its minimization followed by the beamform maps of the experimental data. Noise prediction using Werner Dobrzynski's approximation method together with Karl-Stephane Rossignol's flap side-edge noise model is used to approximate the noise generation because of the wings. This is discussed in the last section of the Chapter together with its comparison to the experimental data.

An illustration of all the noise radiating components of an aircraft can be found in Figure 4.1¹.

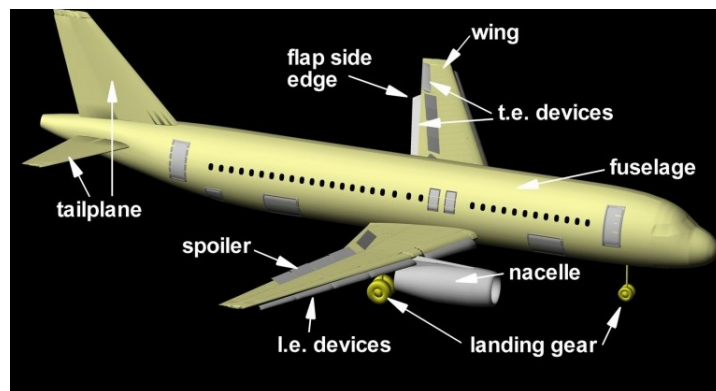


Figure 4.1: Noise-radiating components on an aircraft

4.1 Acoustic Metrics

There are several metrics used in the aerospace industry to evaluate aircraft noise. Two main metrics that will be repeatedly used in this report and the thesis report are Sound Pressure Level (loudness based) metrics and Perceived Noise Level (annoyance based). These metrics are further divided into sub-categories which are discussed in the following subsections.

4.1.1 A-weighted Sound Pressure Level (dBA)

A-weighted Sound Pressure Level have been used in assessment of noise not only in aviation industry but also for road, rail etc. It is sometimes also referred to as dBA metric. As the humans perceive high frequencies as louder compared to lower frequencies, this A-weighting was developed in order to

¹URL:<http://blog.nus.edu.sg/a0108344/2016/10> [Cited 07-April-2018]

approximate the hearing system of humans. Reduction through weights is applied in this metric system for frequencies lower than 500 Hz during noise assessment to make sure that the higher frequencies are weighted higher.

4.1.2 C-weighted Sound Pressure Level (dBC)

C-weighted Sound Pressure Level often referred to as dBC metric is used around airports for noise assessment [29]. This metric system does not apply a penalty to low frequency noise compared to the A-weighted Sound Pressure Level but it does penalize the high frequency noise ($> 4000Hz$) [41]. As this metric system does not penalize low frequency noise, it corresponds better to the annoyance from aircraft low frequency components such as jet noise. It can also very well estimate the threshold of aircraft induced house vibrations.

4.1.3 Sound Exposure Level (SEL)

Sound Exposure Level (SEL) is another metric that is used to describe the noise impact due to the single aircraft movements. It computes impact of the noise in dBA for a single aircraft movement over the period of time at which the noise impact is in 10dBA of the maximum value.

An equation with normalized time to one second to compute the Sound Exposure Level in dBA can be found in Equation (4.1).

$$L_{AE} = 10 \log_{10} \cdot \left[\frac{1}{T_1} \int_{t_1}^{t_2} 10^{\frac{L_A(t)}{10}} dt \right] \quad (4.1)$$

4.1.4 Perceived Noise Level (PNL)

These metrics were developed in early 1960's by Federal Aviation Authority (FAA) to describe the annoyance experienced by the people residing near the airports [4]. The primary reason of developing this metric system was to use it as a means of certifying noise characteristics of an aircraft [46]. Perceived Noise Level loudness scale was developed using the psycho-acoustic tests based on the aircraft sounds carried out in a test environment. This scale was given the unit of noy which is similar to the unit of sone for linear loudness.

Overall noy can be calculated by using the Equation (4.2) where n_{max} is the maximum noy value within the spectrum, n_i is the value to noy for i^{th} band and m is the total number of one-third octave bands where 0.15 in the equation is the multiplication factor for the bands.

$$N = n_{max} + 0.15 \sum_{i=1}^m (n_i) - n_{max} \quad (4.2)$$

Overall Perceived Noise Level can then be determined using the Equation (4.3) where 40 is the chosen reference value of Sound Pressure Level to get equal noisiness in the one-third octave band frequency centered at 1000Hz.

$$PNL = 40 + \frac{10 \log_{10} N}{10 \log_{10} 2} \quad (4.3)$$

4.1.5 Effective Perceived Noise Level (EPNL)

Effective Perceived Noise Level is another metric used to describe the annoyance experienced due to the effect of aircraft noise duration. Duration correction to then already existing Perceived Noise Level (PNL) was added to develop this metric to describe annoyance experienced by people [31]. In Figure 4.2, integration of this metric for duration correction is shown.

The correction for duration which needs to be applied to Perceived Noise Level can be found in Equation (4.4). In the equation, k refers to the time-step index (typical value of 0.5 for aircraft certification) and d refers to the time interval.

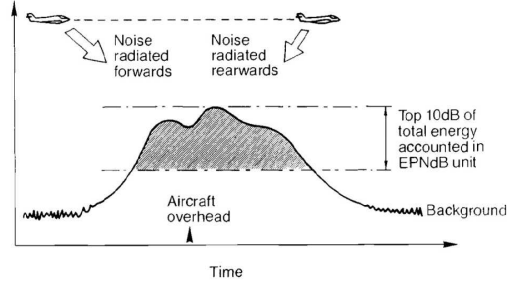


Figure 4.2: Duration correction for Perceived Noise Level [44]

$$D = 10 \log_{10} \left[\sum_{k=0}^{2d} 10^{PNL(k)/10} \right] - PNL - 13 \quad (4.4)$$

With Equation (4.4), duration correction factor can be computed and can be used to calculate the Effective Perceived Noise Level (EPNL). This relation for Effective Perceived Noise Level can be found in Figure 4.5.

$$EPNL = PNL + D \quad (4.5)$$

4.2 Experimental Aero-Acoustic Noise Analysis

In this section, the experimental setup, preparations to perform experiments and the experimental results are discussed.

4.2.1 3D Printing of the wing models

To be able to perform experiments in the anechoic windtunnel channel, scaled wing models are 3D printed. Wing models were developed using *DS CATIA* as discussed in Section 3.3 and the model *stl* format files are exported to a 3D printing software where some processing to the models is done before printing. In total two wing models are generated, one with a flap setting of 25° and the other morphing wing accordingly to observe the potential noise merits between these two.

3D printing material selection and interface connection

At first, ABS plastic was favoured over PLA plastic due to its higher strength. As the wing was to be printed in two separate parts and joined together, another reason for the ABS material preference was based on its capability of the welding of layers. Due to this welding of the layers, the joint is relatively very strong compared to gluing but the use of ABS for printing led to several problems.

At first, the layer thickness used was 0.06mm which would lead to the printing time of one part of the wing to 13 days which was not feasible with the time frame available. Therefore, a concession had to be made with the layer height used. This resulted in the parts to be printed with the layer height of 0.2mm. The quality of the surface was not as bad compared to the 0.06mm but another issue with the printing occurred due to over-sensitivity of ABS material to temperature. This led to an unacceptable and unfixable amount of layer delamination due to thermal stresses as can be seen in Figure 4.3. The ABS plastic is too temperature sensitive for printing of the wing surface as the leading edge and trailing edge form a stress concentration over a long thin length.

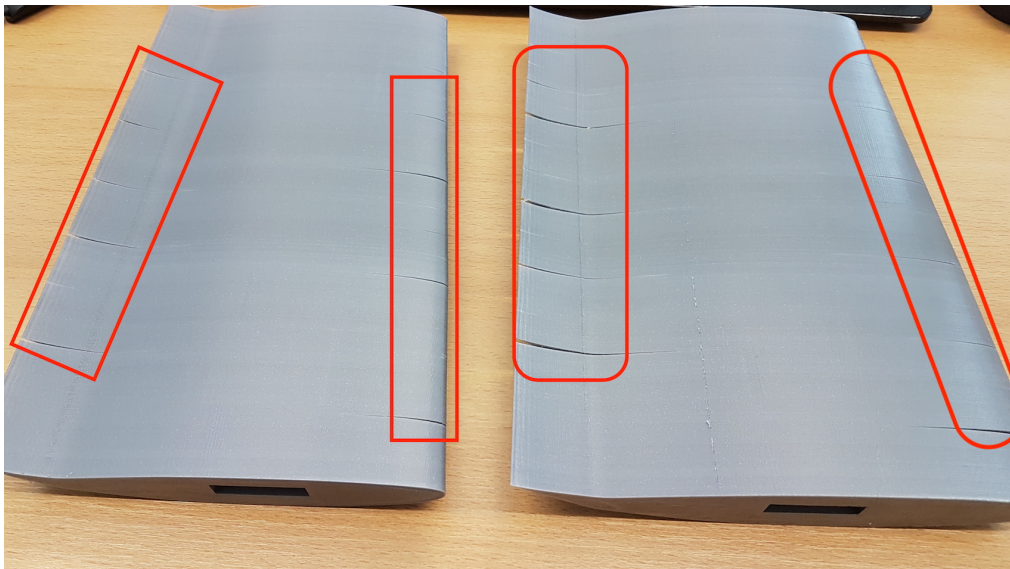


Figure 4.3: 3D printed morphing wing using ABS plastic with layer delaminations highlighted

In the figure above, the rectangular shaped hollow surface at the bottom of the wing is for mounting the wing in the test section. It is a metal core with 51cm in length, which is used to increase or decrease the wing angle of attack when an input is given. This interface can be seen in Figure 4.4



Figure 4.4: Interface rod to mount the wing in the test section

The initial choice for ABS was based on the welding of layers to keep very high overall strength of the structure with a very strong joint due to the requirement of testing at high velocities, but the option of strength provided by metal core for the model was not taken into account. As the wing will receive adequate support from the metal core, it was agreed to use PLA for 3D printing and glue bond for joining wing parts.

Scaling and geometrical adjustments to the wings

Due to the requirement of the windtunnel test section both models are required to be 51cm in span to make sure it fits both horizontal side-plates. If a gap is left between the wing and the horizontal side-plates, production of noise at the edges can occur, which must be avoided as it is an additional source in addition to the noise of the wing itself.

Only parts with high-lift devices/surfaces are printed meaning that the outboard wings from both wing models are removed. Dihedral have also been removed from the wings so that there is no additional Z-component increase along the span. A straight metal rod needs to be inserted for the interface in the models so dihedral had to be removed from the wing. The taper ratio for the wings still exists in the prototypes, therefore the longest chord length is at the root of the wing.

Both models are scaled down by a factor 10.21 in X and Z direction. With this scaling factor the morphing wing (bigger of the two) is 20cm in X-direction (chord-wise) at the wing root. Motivation of fixing the maximum chord length is due to the printing size limitations of the printer ($350\text{mm} \times 200\text{mm} \times 200\text{mm}$). The other wing is smaller than the morphing wing but the scaling factors are kept same in order to

observe the potential noise merits (*in CATIA and 3D printing software scaling factors become as (1/s-scaling factor) otherwise it will increase in size*). Longer the chord length, higher is the noise generated at the trailing edge.

To meet the windtunnel requirements of spanwise model length of 51cm, morphing wing needs to be scaled down by factor of 10.94 i.e. in Y-direction and for the conventional wing it is scaled down by a factor of 9.505 in Y-direction. As 51cm can not be printed by the printer in one go due to the limitation in maximum printable size of the printer, therefore, the models are cut in half before printing in Y-direction. Two parts are printed for each wing and then glued together.

Printing of the wings

3D printing of the wings is carried out at the in-house 3D printing facility of NLR with *Ultimaker 3 Extended*². Maximum printable size by the printer is *350mmx200mmx200mm*. In Figure 4.5, both conventional and the morphing wings being printed in the 3D printer can be found. Due to the use of a 3.5mm layer thickness, surface roughness over all whole of the printed objects exists. This surface roughness is due to the curvilinear characteristic of the wing profile. From the figure, existence of areas where the surface unevenness is more prominent can be seen. It usually happens towards the trailing edges where non-horizontal layers from the printer exists.

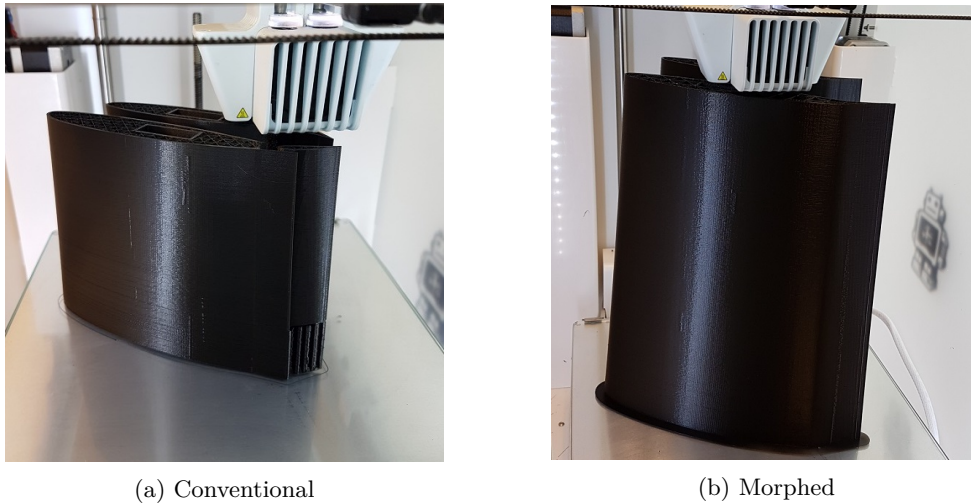


Figure 4.5: Morphed and conventional wings being 3D printed with Ultimaker 3 Extended

After 3D printing of the parts with PLA, these parts are then joined together using a strong glue bond. In Figure 4.6, glue bond of the morphing wing to join two separate parts can be seen. This was done for both the conventional and the morphing wings. The highlighted area in the figure shows the surface area where both parts were glued together. Due to this glue bond, rough surface patches are present, later requiring sanding.

²URL:<https://ultimaker.com/en/products/ultimaker-3> [Cited 27-April-2018]



Figure 4.6: Morphed wing glued after 3D printing with glued surface highlighted

From the printing technique used, the surface roughness on the wing prototypes needs to be smoothed out. Also, the uneven surface due to the glue bond needs to be sanded to make it smooth. Three different kinds of sandpapers depending on the surface roughness/unevenness were used in obtaining a smooth surface over the wings. Figure 4.7 contains the bottom side of the finished and final wing models ready for the experiments.

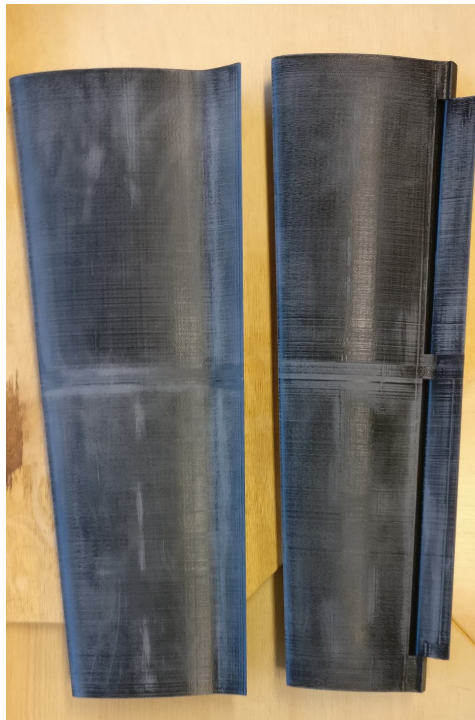


Figure 4.7: Both conventional and morphed wing models ready for testing

4.2.2 Experimental setup

Noise experiments are performed in an anechoic chamber. The main reason of performing noise/acoustic experiments in an anechoic chamber is to avoid any sound reflections. Due to this anechoic chamber, microphones record direct noise/sound such that there are no reverberant sounds.

Experiments are carried out at NLR's anechoic chamber with dimensions $5 \times 5 \times 3 \text{m}^3$. The room is covered with the foam wedges as mentioned earlier to absorb the noise in order to avoid sound reflections. Foam wedges of the NLR anechoic facility can be seen in Figure 4.8.

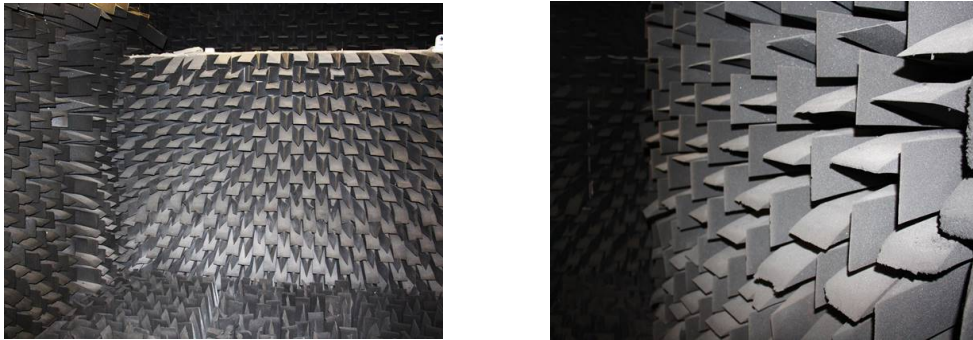


Figure 4.8: Anechoic chamber in the windtunnel is equipped with noise absorbing foam wedges

These foam wedges absorb $> 99\%$ of the noise that is above 500Hz . Low frequency noise, less than 500Hz is mainly due to the background noise, which is not of particular interest for the experiments.

The test section as seen in Figure 4.9 constitutes of two end plates, one on the upper side of the test model and one on the bottom with dimensions of $0.9 \times 0.7 \text{m}^2$ which extends up to the the windtunnel nozzle which is $0.38 \times 0.51 \text{m}^2$.



Figure 4.9: Wing profile mounted between two horizontal side-plates

These horizontal end plates result in 2D wing analysis rather than 3D. 3D effects are eliminated by the end-plates. To make sure these end-plates do not reflect noise or result in extra noise generation, these end-plates are acoustically lined with noise absorbing foam. This 5.5 cm layer of foam to absorb sound is covered by 5% open perforated plate.

Microphones in the anechoic channel are placed in an array consisting of 48 microphones. Layout of the microphone positioning is shown in Figure 4.10 along with their numbering. Microphone 1 is located in front of the center of the test section. Microphones in the array record the Sound Pressure Level at a certain distance away from the source and at a certain radial position. Positioning of the microphones in the array is already optimized such that the occurring side lobes are suppressed to the maximum over a range of frequencies.

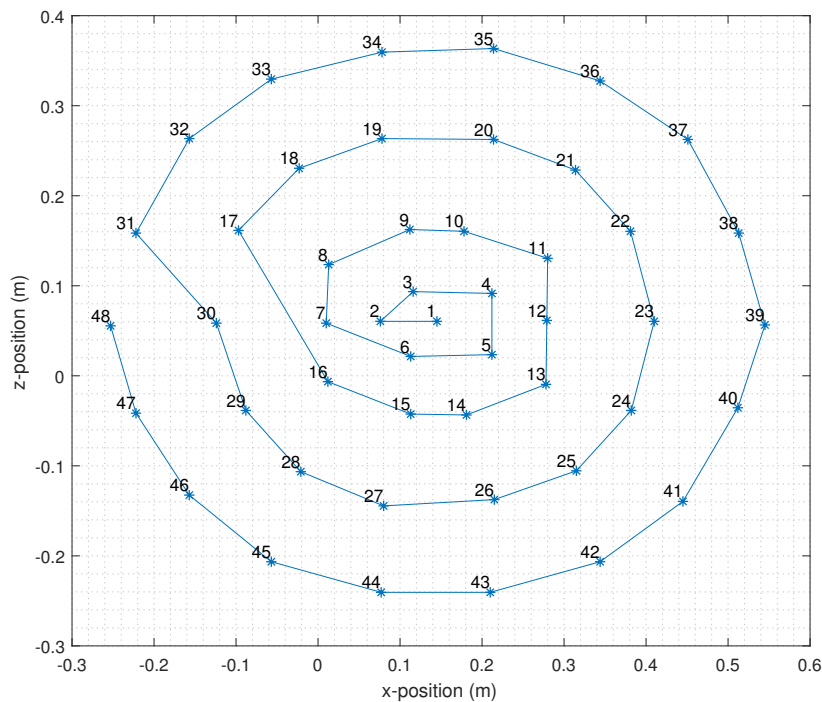


Figure 4.10: Layout of the microphone array

Each microphone in the ring array was developed by Bruer & Kjær[20], their sampling time, sampling frequency and the number of samples for each microphone can be found in Table 4.1.

Table 4.1: Important parameters of the microphones used in experiments

Parameter	Value	Units
Number of samples per microphone	1536000	[-]
Sample frequency	51200	[Hz]
Sample time	30000	[ms]

Morphing wing mounted between two horizontal end-plates in the test section with a microphone array in the background can be found in Figure 4.11.



Figure 4.11: View of the wing(morphed) fitted between side-plates and in front of the microphone array

Calibration of microphones

Microphones need to be calibrated to analyse their sensitivity and be able to make measurements. There exists some background noise originating from the external sources, which leads to an inaccurate calibration. In order to prevent this, the frequency domain of the microphone pressure was Fourier transformed. By doing so the pressure fluctuations that belong to the calibration device can be separated from other external sources present at different frequencies.

A python script was developed for the calibration of microphones using piston-phones. A set of input parameters are filled in the python script, which in return gives the output. The main output consist of a file containing all the resulting calibration factors for all 48 microphones. During calibration of the microphones, if a same microphone have been calibrated more than once all the resulting calibration factors are then analysed from the calibration output files. A calibration table in a correct format is created manually after inputting the right calibration factor for each microphone.

Results

This section of the report deals with the results of microphone calibrations. Calibration of the microphones was performed a day before the experiments. Broken microphones can be identified by huge variations in the calibration factors. Some microphones were calibrated multiple times to avoid any discrepancies in the measurements.

To check for the directivity, no corrections were required to apply as the effect of directivity is same in all directions and contributes to less than 2dB with angles ranging to 45° with maximum frequency of 15kHz.

No discrepancies were found in the frequency-dependent sensitivities of the microphones. In Figure 4.12, final calibration factors can be found where it can be seen that all of the calibrated values for microphones

lies close to each other. Therefore, no faulty microphone was detected during the calibration.

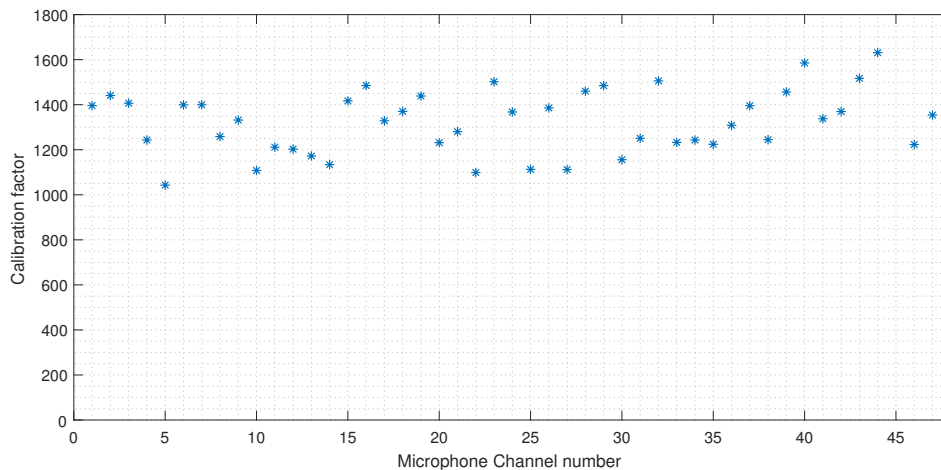


Figure 4.12: Calibration factors for all 48 microphones

Operational settings

In this part of the chapter all the operational settings for the experiments are discussed. For each of the wings it was decided to test angles of attack of 0° , 2° , 4° , 6° , 8° , 10° and 12° for each of the 35, 50 and 70 m/s cases. For the conventional wing the highest speed of 70m/s was not possible, reasons of which will be discussed later. Background and windtunnel noise at 35, 50 and 70 m/s were also measured in an empty test section to visualise the differences in the Sound Pressure Level spectra with the presence of wing models.

For each geometrical and operational setting, 30 seconds were required to obtain the microphone data and about another 10 to 15 secs for saving it.

Data acquisition

The data acquisition system records data in the form of binary files from microphones for different operational and geometrical settings. This data is then saved and later used for post processing and analysis. Acoustic data for each configuration was saved using NLR's *VIPER* data acquisition system. As mentioned in Table 4.1, each configuration measurement time was 30s with a sampling frequency of 51200Hz which leads to 1536000 samples for each microphone.

For frequencies less than 500Hz, mainly the background noise and irrelevant noise sources are present, therefore a 500Hz high-pass filter was applied. On the other side, a 25.6kHz low-pass filter was applied as the frequencies above that level are not hearable for a human ear. Both of these filters were applied to the signal of each microphone before the AD converter.

Experiments

Experiments were carried out at the NLR's AV-LAB. At first the morphed wing was tested in the windtunnel for 35, 50 and 70 m/s and for each speed seven different angles of attack were tested. These angles of attack range from 0° to 12° in steps of two. The highest angle of attack was limited to 12° to avoid any damage to the wing structure, as higher angles of attack increase the load on the wing surface. A 3D printed wing prototype was never tested at the AV-LAB before so to be sure to avoid any structural damage to the wing it was limited to 12° .

Due to the open-jet or semi open-jet nature of the windtunnel, the actual angle of attack at the wing is slightly lower than the input provided. As no real way to obtain the corrected angle of attack for the windtunnel was known, the input angle of attack is assumed to be the flow angle of attack at the wing.

Morphing wing was successfully tested for the 35, 50 and 70m/s but the conventional wing was only tested for 35 and 50m/s. At 70 m/s the flap of conventional wing started to deform slightly. With this deformation, the comparison with the conventional and the morphed wing would not have been valid. This deformation was observed at 0° angle of attack. With the increase in angle of attack, probability of the failure of the structure would have increased. Therefore, it was decided to not proceed with the 70m/s testing of the conventional wing.

An overview of the testing facility before the start of the experiments can be seen in Figure 4.13.

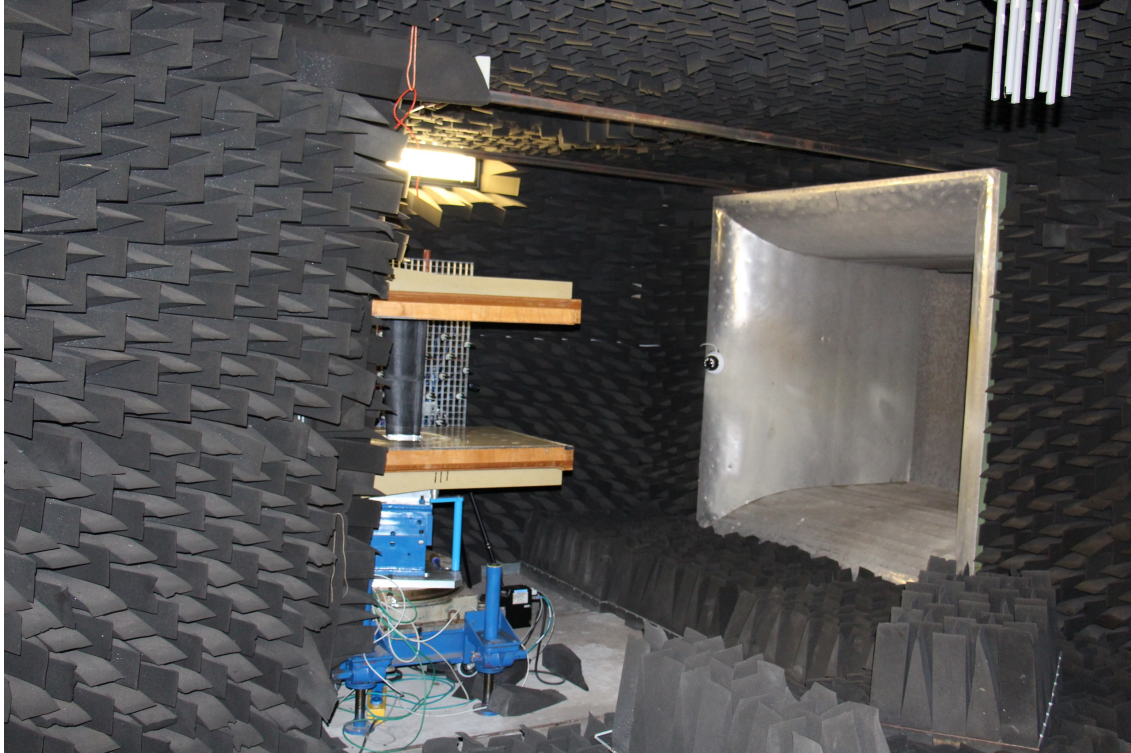


Figure 4.13: Overview of the noise facility before an experiment

Final Test Matrix

A final test matrix, after completing all the experiments is assembled in Table 4.2. Table consists of six columns with first for the event/filename saved as by the data acquisition system. The events column starts from measurement 5 as the first four measurements were done with the speaker as shown in Table 4.3. In total 50 measurements were done as seen in the first column of the table. In the second column the wing type tested in the test section is mentioned. It is either a conventional wing, morphed wing or an empty test section for recording the background and windtunnel noise. In the third column, wind speed is mentioned which is either 35, 50 or 70m/s. The fourth column is the angle of attack at which the wings are placed with respect to the incoming flow. Angles of attack range from 0° to 12° in steps of two for a certain geometrical or operational setting. Mach numbers and the speed of sound are shown in fifth and sixth column. The speed of sound is based on the temperature in the test section and the mach number is a function of the wind speed and the speed of sound.

Rows that are highlighted with a red colour indicate either a repeated measurement or a wrong measurement. Rows highlighted in red colour were not analysed during the data analyses from experiments. Rows with similar operational settings have been highlighted with a similar colour both for the morphed and the conventional wing. As discussed earlier 70m/s experiments were only possible for the morphing wing, therefore, no datasets in the table can be found for conventional wing at 70m/s.

Table 4.2: Final test matrix

Event	Wing type	Speed[m/s]	Angle of attack[°]	Mach[-]	Speed of sound[m/s]
DPN5	Morphed Wing	35	4	0.102	341.74
DPN6	Morphed Wing	35	6	0.102	341.86
DPN7	Morphed Wing	35	8	0.102	341.93
DPN8	Morphed Wing	35	10	0.102	341.97
DPN9	Morphed Wing	35	6	0.102	342.01
DPN10	Morphed Wing	35	12	0.102	342.07
DPN11	Morphed Wing	35	0	0.102	341.5
DPN12	Morphed Wing	35	6	0.102	341.95
DPN13	Morphed Wing	20	2	0.059	341.19
DPN14	Morphed Wing	35	2	0.102	341.55
DPN15	Morphed Wing	50	0	0.145	344.9
DPN16	Morphed Wing	50	2	0.145	345.36
DPN17	Morphed Wing	50	4	0.145	345.55
DPN18	Morphed Wing	50	6	0.145	345.64
DPN19	Morphed Wing	50	8	0.145	345.7
DPN20	Morphed Wing	50	10	0.145	345.75
DPN21	Morphed Wing	50	6	0.145	345.81
DPN22	Morphed Wing	50	12	0.145	345.83
DPN23	Morphed Wing	70	0	0.2	351.13
DPN24	Morphed Wing	70	2	0.2	351.67
DPN25	Morphed Wing	70	4	0.2	351.15
DPN26	Morphed Wing	70	6	0.2	351.76
DPN27	Morphed Wing	70	6	0.2	350.97
DPN28	Morphed Wing	70	8	0.2	351.75
DPN29	Morphed Wing	70	10	0.2	352.06
DPN30	Morphed Wing	70	6	0.2	352.36
DPN31	Morphed Wing	70	12	0.201	352.47
DPN32	Empty testsection	35	-	0.102	345.64
DPN33	Empty testsection	50	-	0.145	345.93
DPN34	Empty testsection	70	-	0.2	350.63
DPN35	Conventional Wing	35	0	0.102	342.36
DPN36	Conventional Wing	35	2	0.102	342.58
DPN37	Conventional Wing	35	4	0.102	342.68
DPN38	Conventional Wing	35	6	0.102	342.73
DPN39	Conventional Wing	35	8	0.103	342.78
DPN40	Conventional Wing	35	10	0.103	342.81
DPN41	Conventional Wing	35	6	0.102	342.85
DPN42	Conventional Wing	35	12	0.103	342.91
DPN43	Conventional Wing	50	0	0.146	345.7
DPN44	Conventional Wing	50	2	0.146	345.94
DPN45	Conventional Wing	50	4	0.145	346.08
DPN46	Conventional Wing	50	6	0.145	346.13
DPN47	Conventional Wing	50	8	0.145	346.18
DPN48	Conventional Wing	50	10	0.145	346.23
DPN49	Conventional Wing	50	6	0.145	346.25
DPN50	Conventional Wing	50	12	0.146	346.3

4.2.3 Results from the experiments

Results from the experiments are discussed in this part of the report. Results have been divided into four different parts. In the first part speakers in the test section at different locations and different frequencies are analysed to ensure the correct working of the microphones and the data acquisition system. In the second part, background and the windtunnel noise for three different speeds are measured. The third part contains the comparison spectra between the morphed and the conventional wing for two different microphone locations. In the last part of results, Overall Sound Pressure Levels and Overall A-weighted Sound Pressure Levels are calculated for all cases and a comparison is made between the two types of wings.

Speakers

Before the experiments were performed, speakers with two different frequencies at two different locations in the test section were analysed to make sure the microphones and the data acquisition system are working as expected. Table 4.3 contains all four cases analysed with speakers with their positioning and the frequencies. DPN values are the events/file-names used by the VIPER data acquisition system to record data. Speaker position (0,0,0) refers to the center of the test section. All other changes in the speaker positions are in metres.

Table 4.3: Test matrix for speaker analysis

Event	Test object	Speaker position	Frequency
DPN1	Speaker	pos 0 0 0	1000Hz
DPN2	Speaker	pos 0 0 0	5000Hz
DPN3	Speaker	pos 0.3 -0.21 0	1000Hz
DPN4	Speaker	pos 0.3 -0.22 0	5000Hz

Four different cases with the speakers were analysed. Figure 4.14 contains all the processed Sound Pressure Level spectra. Sound Pressure Levels lies on the Y-axis of the plots whereas frequency on X-axis.

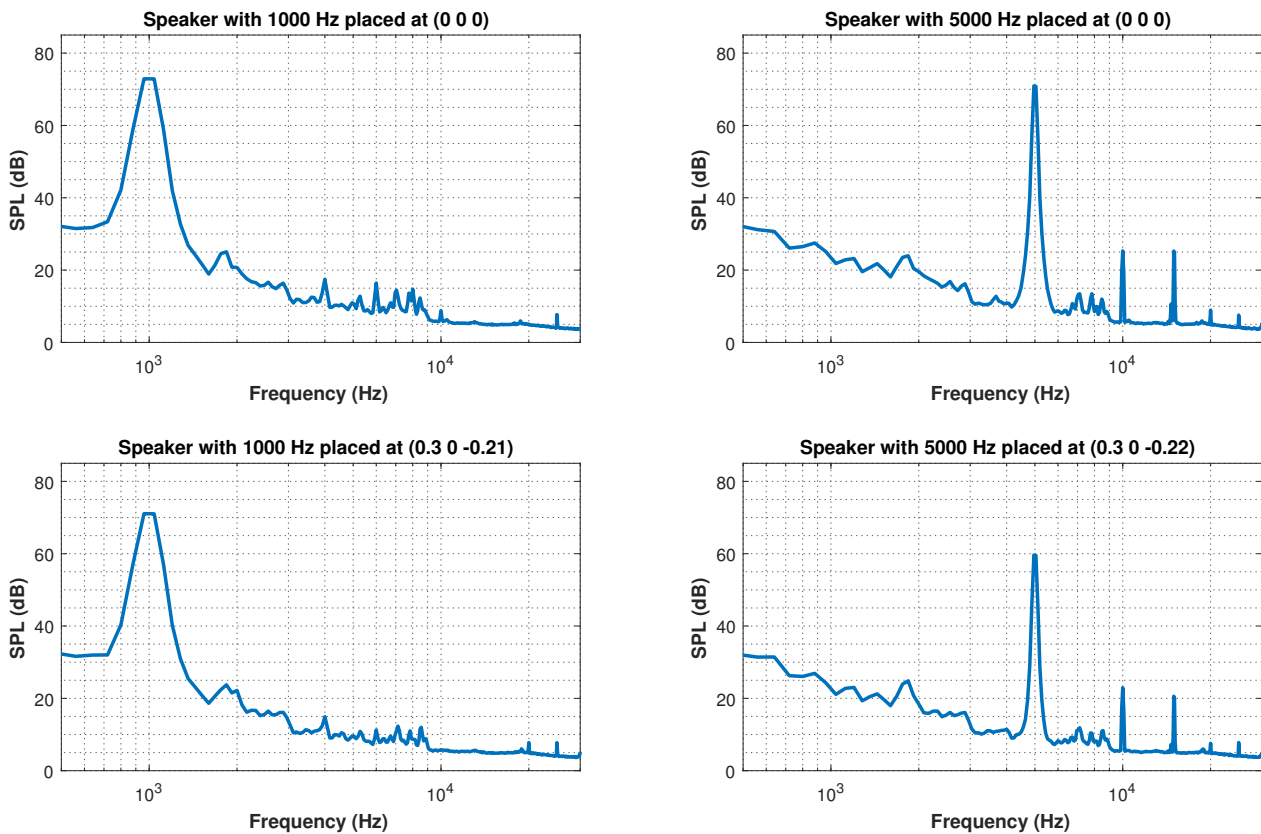


Figure 4.14: Sound Pressure Level spectra for the speaker with two different frequencies and speaker positions

All the measurements analysed here are from microphone 1. Location of the microphones is shown in Figure 4.10. For the first event *DPN1*, the speaker is positioned at the center of the test section at (0,0,0). Top two plots in Figure 4.14 corresponds to the datasets *DPN1* and *DPN2* where the speaker frequencies are set at 1kHz and 5kHz with speaker location at (0,0,0). In the subplot for 1kHz at (0,0,0)

it can be seen there is a peak at the 1000Hz frequency and for the 5kHz at (0,0,0) peak shifts to the 5000Hz mark. Other smaller peaks in the subplots belong to the background noise in the windtunnel. The windtunnel itself is not in use during the speaker analysis therefore no contribution to the Sound Pressure Levels from the windtunnel noise is present. For 5kHz it can be seen that the peak is much sharper than the 1kHz. At low frequencies (below 1000Hz) background noise is higher than at 5kHz therefore due to the difference in the Sound Pressure Levels for the background noise this difference in the peak shape exists.

In the bottom two subplots, the location of the speaker has been changed for both the 1kHz and 5kHz frequencies. This means that the speaker is no more in line with the microphone 1, which is in line with the center of the test section. This will result in the Sound Pressure Level to be recorded by the microphone to be slightly lower than the above two subplots where the speaker position is (0,0,0). From the figure, it can be verified that the Sound Pressure Level is slightly lower than the previous case.

These analyses from the speakers completely satisfy the expectations and ensured that the microphones and the data acquisition are working well with the expectations. After these analysis, actual experiments can be carried out.

Windtunnel & background noise

Before the experiments on the wing prototypes are performed, it is necessary to determine the background and the windtunnel noise to see how much noise in addition to the background and windtunnel noise the wing prototypes add. The windtunnel and the background noise was measured without any object in the test section and at three different velocities. These three velocities are the one at which the wings are going to be tested. Background and windtunnel noise were measured at 35, 50 and 70 m/s. Figure 4.15 contains the recorded sound pressure levels for these three velocities.

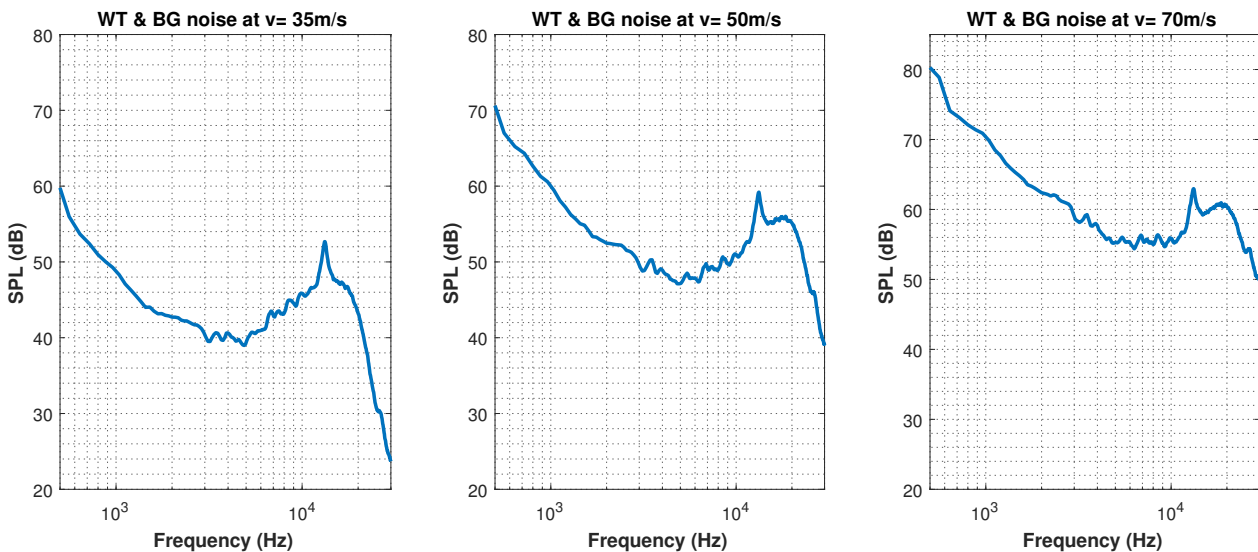


Figure 4.15: Windtunnel and background noise for 35,50 and 70m/s

The windtunnel generates broadband noise over a range of frequencies. In the figure it can be seen that as the velocity is increased, an increase in the Sound Pressure Levels can be observed over almost the whole range of frequencies. Windtunnel noise increases with the increase in velocity but the background noise remains constant.

SPL spectra

Data from the microphones is processed to generate the Sound Pressure Level spectra. Comparing these Sound Pressure Level spectra for a range of frequencies between different datasets allows to visualise the differences in the noise generation at a certain frequency. Data from two different microphones from the array is used to draw these differences. The microphone 1 is located right in front of the center

of the test section and microphone 39 is located in line with microphone 1 but at a certain distance behind the trailing edge of the wing in the test section. The Sound Pressure Levels for the conventional wing are plotted against the Sound Pressure Levels of morphing wing together with the background and windtunnel noise. Plotting against the background and windtunnel noise allows to see the differences in the noise generation by each of the wing as compared to the external sources.

Sound Pressure Level spectra from the angles of attack of 8° , 10° and 12° for two different speeds and two different microphone locations are shown as following in Figures 4.16, 4.17 and 4.18 respectively. These are discussed afterwards as well. Sound Pressure Level spectra for the other lower angles of attack can be found in the Appendix D.1.

AOA = 8°

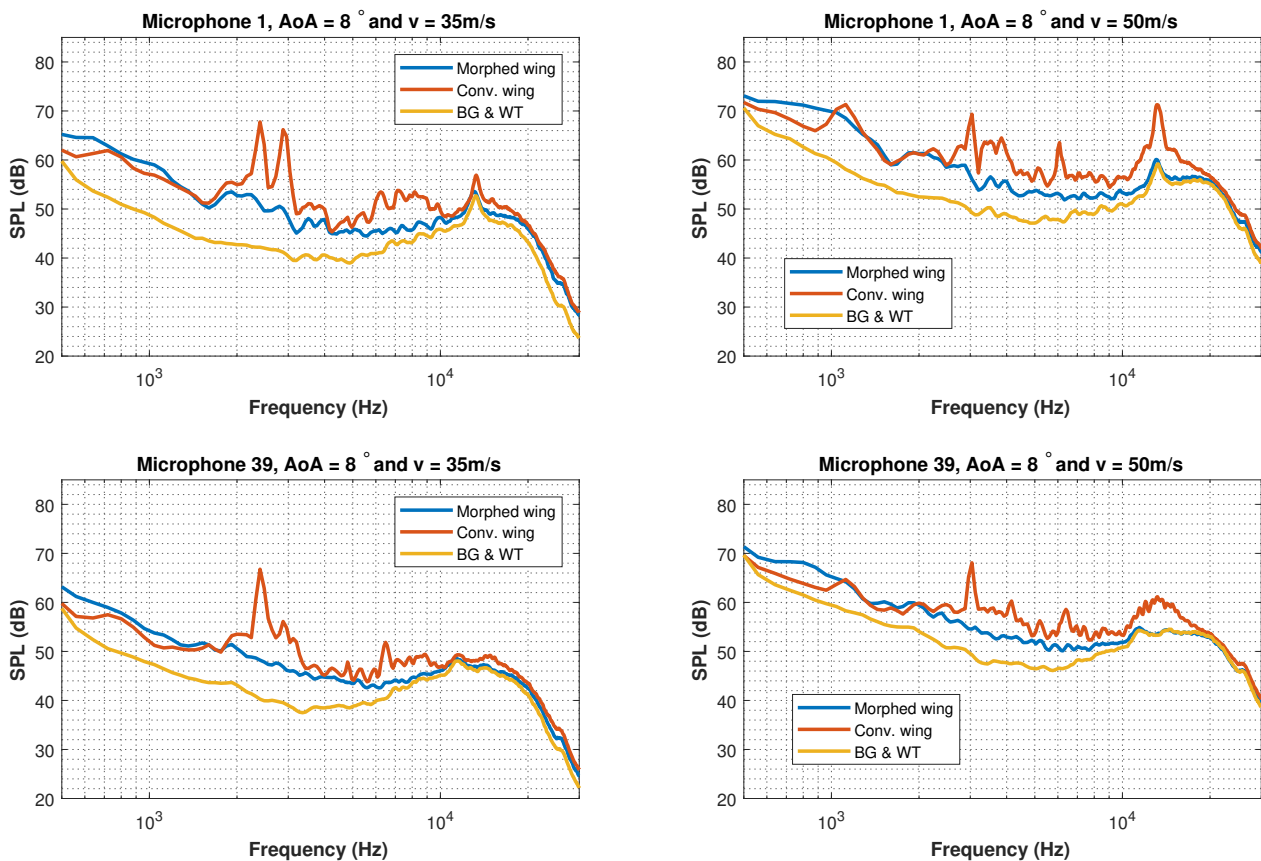


Figure 4.16: SPL spectra for morphed and conventional wing along background noise with angle of attack of 8° for two different speeds and microphones

AOA = 10°

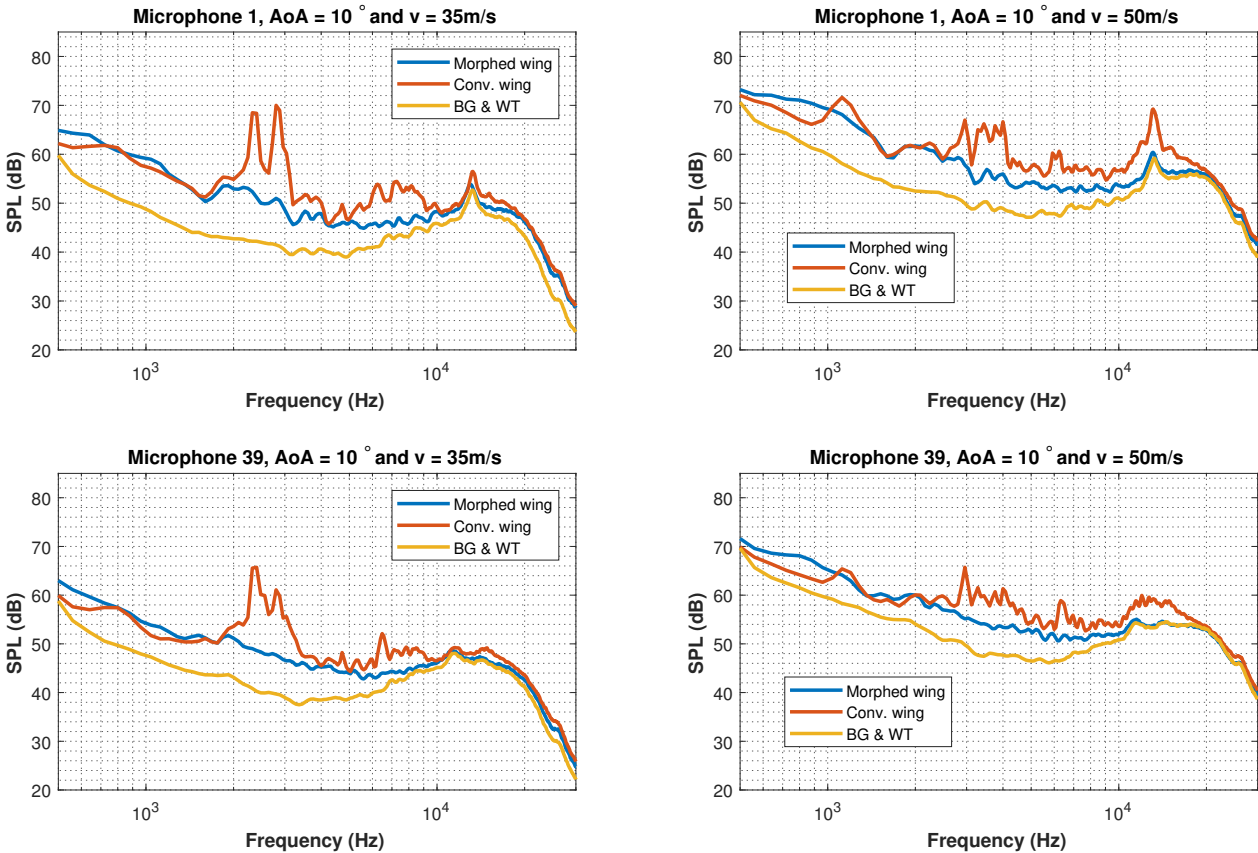


Figure 4.17: SPL spectra for morphed and conventional wing along background noise with angle of attack of 10° for two different speeds and microphones

AOA = 12°

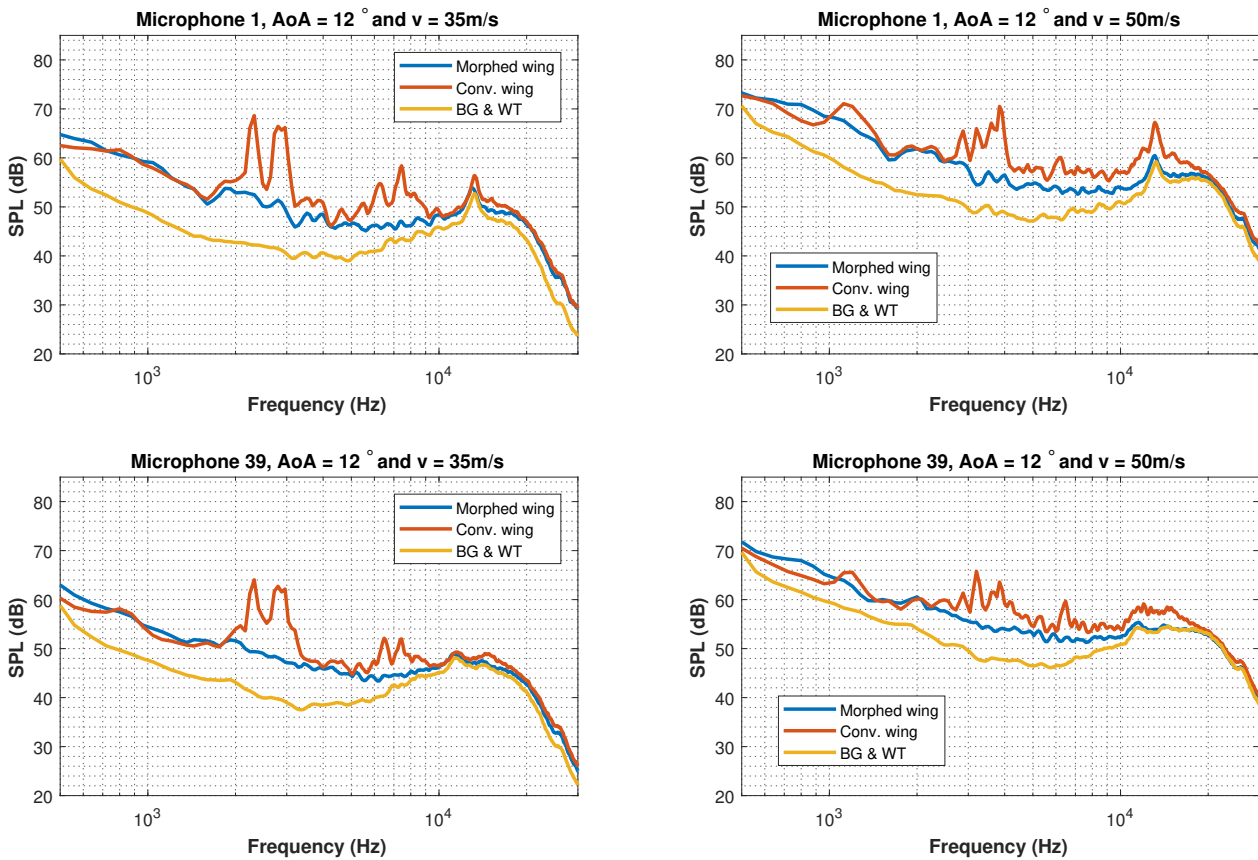


Figure 4.18: SPL spectra for morphed and conventional wing along background noise with angle of attack of 12° for two different speeds and microphones

Discussion of results

From the figures, it can be noticed that after the frequency of 1100Hz, the conventional wing generates higher noise peaks compared to the morphing wing. Between 1100 Hz and 1300Hz the difference in the noise peaks is higher for the 35m/s plots whereas for the 50m/s these peaks dampen out but the difference is still present. Only the peaks where the difference is higher than 3dB can be considered to provide the noise merits because of doubling of the sound pressure. The background and the windtunnel noise in all the cases is lower than the noise generated by the wings in the test section. It can be also noticed that at microphone 1, the noise peaks are relatively higher than that of microphone 39 which is at some distance behind the trailing edge. Loss of energy or dispersion of energy by travelling sound waves and the difference in the angle at which the microphone is located with respect to the trailing edge causes this variation in the Sound Pressure Levels.

Spectra for the wings for most of the frequency range are higher than the background noise by 3dB. At low frequencies (<500) windtunnel and the background noise is more dominant than the noise generated by the wings. Between 500Hz and 1000Hz it can be noticed that the morphing wing noise is higher or equal to the conventional wing, which is due to the noise generation due to very tiny gap left between the horizontal plates and the morphing wing. This gap generates extra amount of noise for the morphing wing at low frequencies.

Sources of these peaks are later visualised and discussed in the beamforming data for the wings.

In order to quantify the differences in the noise generation by the morphing and conventional wings, Overall Sound Pressure Levels from microphone 1 have been calculated for the wings. Overall Sound Pressure Level is the equivalent Sound Pressure Level obtained by integrating over all of the frequencies. Energy of the sound wave at each frequency is added up to construct the wave and Overall Sound Pressure Level is the level of that wave. This provides a direct measure of the differences occurred in the noise generation of the wings. Table 4.4 contains all the Overall Sound Pressure Levels of the wings and also the differences in the Overall Sound Pressure Levels of both wings.

Table 4.4: Overall Sound Pressure Level comparison between both wings

Operational settings	$OSPL_{conv.}$ [dB]	$OSPL_{morph.}$ [dB]	$OSPL_{conv.-morph.}$ [dB]
V=35m/s & AOA= 0°	76.51	76.09	66.2
V=35m/s & AOA= 2°	76.55	76.08	66.7
V=35m/s & AOA= 4°	76.84	76.07	68.9
V=35m/s & AOA= 6°	76.47	75.76	68.3
V=35m/s & AOA= 8°	77.67	74.77	74.5
V=35m/s & AOA= 10°	78.90	74.72	76.8
V=35m/s & AOA= 12°	78.54	74.77	76.2
V=50m/s & AOA= 0°	88.15	86.14	83.8
V=50m/s & AOA= 2°	88.22	85.88	84.4
V=50m/s & AOA= 4°	88.05	85.61	84.4
V=50m/s & AOA= 6°	87.64	84.26	85.0
V=50m/s & AOA= 8°	86.41	83.18	83.6
V=50m/s & AOA= 10°	85.89	83.19	82.5
V=50m/s & AOA= 12°	85.77	83.11	82.4

From the Overall Sound Pressure Level table, it can be seen that the morphing wings are generating lower overall Sound Pressure Level than the conventional wings for all operational settings and configurations. The percentage reduction in the Overall Sound Pressure Level by replacing the conventional flaps with morphing surfaces can be obtained by converting decibels to sound pressures and then computing the percentage differences.

For 35m/s data, it is noticed that the percentage difference in the Overall Sound Pressure Levels increases with the increase in the angle of attack. Minimum difference between the morphing and the conventional wing was observed at the angle of attack of 0° where the difference was just 4.7%. On the other hand, maximum difference in the Overall Sound Pressure Levels was observed at the angle of attack of 12° where the difference was around 38%. For the 50m/s data, minimum difference in the Overall Sound Pressure Level has increased incredibly but the maximum has reduced. Minimum difference of 20.66% was observed at the lowest angle of attack and the maximum difference was obtained at the angle of attack of 6° where the difference in the noise generation by the morphing and the conventional wing in terms of Overall Sound Pressure Level is about 32%.

A-weighting was developed in order to approximate the hearing system of humans. Reduction is applied in this metric system for frequencies lower than 500 Hz during noise assessment to make sure that the higher frequencies are weighted higher. Table 4.5 contains the A-weighted Overall Sound Pressure Levels between the conventional and morphing wings and from the table it can be noticed that after applying A-weighting to the data, noise generation by the conventional wing is higher than the morphing wing for all operational and configuration settings.

Table 4.5: Overall A-weighted Sound Pressure Level comparison between both wings

Operational settings	$OASPL_{conv.}$ [dB]	$OASPL_{morph.}$ [dB]	$OASPL_{conv.-morph.}$ [dB]
V=35m/s & AOA= 0°	75.31	74.81	65.7
V=35m/s & AOA= 2°	75.37	74.81	66.2
V=35m/s & AOA= 4°	75.86	74.77	69.3
V=35m/s & AOA= 6°	75.26	74.40	67.8
V=35m/s & AOA= 8°	77.27	73.27	75.1
V=35m/s & AOA= 10°	78.90	73.23	77.5
V=35m/s & AOA= 12°	78.44	73.28	76.9
V=50m/s & AOA= 0°	85.28	85.01	73.1
V=50m/s & AOA= 2°	85.37	85.04	74.0
V=50m/s & AOA= 4°	85.41	84.76	76.8
V=50m/s & AOA= 6°	85.47	83.20	81.6
V=50m/s & AOA= 8°	84.64	81.93	81.3
V=50m/s & AOA= 10°	84.44	81.93	80.9
V=50m/s & AOA= 12°	84.61	81.80	81.4

Conventional beamforming & Point Spread Function(PSF)

Usage of microphone arrays in determining the acoustic sources and their strengths has become common not only in Aerospace but in other sectors as well. Performance of this conventional beamforming is hugely dependent on the size, design and layout of the microphone arrays. Conventional beamforming results are convolved with another acoustics phenomenon known as Point Spread Function. In order to further improve the beamforming results, inverse/deconvolution methods needs to be incorporated with the conventional beamforming. In doing so, a clear and an accurate representation of the sources along with their strengths can be obtained.

To investigate and locate the noise sources in the conventional and morphed wing experiments, beamforming with the help of the microphone array is done followed by the additional algorithms to further improve the results. In this part of the chapter, mathematical background of conventional beamforming is explained followed by the Point Spread Function and the deconvolution method to minimize its effect.

Conventional Beamforming

Conventional beamforming method developed by Prof. Pieter Sijtsma of the TU Delft is followed [42]. The number of microphones is indicted with an index N and the vector p contains all the pressure values for each microphone. All these pressure values are frequency dependent and are contained in matrix 4.6.

$$\mathbf{p} = \begin{bmatrix} p_1(f) \\ \vdots \\ p_N(f) \end{bmatrix} \quad (4.6)$$

A cross-spectral matrix can then be defined using this pressure matrix which can be found in Equation 4.7. This equation contains the frequency dependent pressure values and its complex conjugate transpose.

$$\mathbf{C} = \frac{1}{2} \langle \mathbf{p} \mathbf{p}^* \rangle \quad (4.7)$$

Another well known function in acoustics is the Green's function which helps in defining a steering vector. Microphone is located at a particular distance from the noise source and the Green's function defines the propagation of the sound source(unit monopole) towards the microphone. This propagation of the monopole sound source is defined with Green's function.

Complex amplitudes a belonging to the source is then obtained using the minimization of a function J . It is shown in Equation 4.8.

$$J = \|\mathbf{p} - a\mathbf{g}\|^2 \quad (4.8)$$

This minimization of function J leads to the following result shown in Equation 4.9 where a as mentioned before are the complex amplitudes belonging to the source.

$$a = \frac{\mathbf{g}^* \mathbf{p}}{\|\mathbf{g}\|^2} \quad (4.9)$$

A weight vector depending on the steering vectors is defined in Equation 4.10 which is used later to define the auto-power(A) of the source.

$$\mathbf{w} = \frac{\mathbf{g}}{\|\mathbf{g}\|^2} \quad (4.10)$$

Auto-power of the source can be defined using Equation 4.11 using the weight vector defined in Equation 4.10.

$$A = \frac{1}{2} |a|^2 = \frac{1}{2} a a^* = \mathbf{w}^* \mathbf{C} \mathbf{w} \quad (4.11)$$

Point Spread Function and its minimization

The method to apply conventional beamforming and obtain beamform plots have been determined above. However, the conventional beamforming approach needs more processing to remove the convolution of Point Spread Function in the beamforming contours. Figure 4.19 illustrates the phenomenon of Point Spread Function. Side lobes as can be seen in the figure reduce the acoustic beamform image resolution. These side-lobes needs to be suppressed to obtain clearer beamform maps.

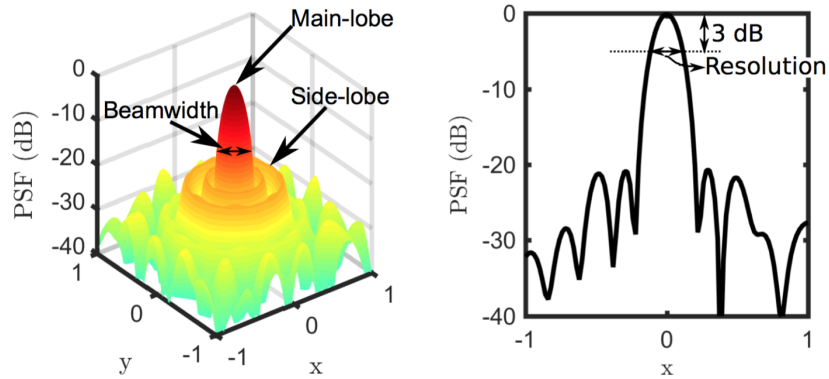


Figure 4.19: Illustration of side lobes in PSF[5]

Beamforming results can be improved by optimization of the microphone array or by increasing the microphone array aperture. After a certain increase in the microphone array aperture or the optimization of the array, the beamform map resolution can not be enhanced further. These limitations in the resolution improvement could be due to either the space limitations, loss in coherence or the limited noise source directivity. Therefore, inverse/deconvolution methods/techniques need to be incorporated to the conventional beamforming to enhance resolution of the beamform maps.

Due to the convolution of Point Spread Function with Conventional Beamforming results, the beamforming technique requires extra processing to achieve clearer and accurate results. Therefore, a technique developed by Pieter Sijtsma again at TU Delft is incorporated with the conventional beamforming[49]. Several other deconvolution/inverse methods exist that remove the effect of PSF in the beamforming

maps. Most prominent examples of these are the CLEAN[17] and DAMAS[10] but the method developed by Pieter Sijtsma is followed for the improvement of beamform maps for the experiments.

Theoretical background of Point Spread Function is explained at first and then a improved method developed by Prof. Pieter Sijtsma to take into account for different losses in the beamform maps resolution is discussed, which will also be used for the beamforming maps for the experiments. As the noise is measured with the help of an array, it is required to obtain the response of the array to the point source. Subscripts j and k refer to the scan points.

At first only the basic derivation of Point spread function is shown followed by the technique to minimize their effect. The Cross Spectral Matrix using the terms defined in the previous section can be computed using Equation 4.12.

$$\mathbf{C}_j = \frac{1}{2} \cdot \mathbf{g}_j \mathbf{g}_j^* \quad (4.12)$$

This result can then be input into Equation 4.11 of conventional beamforming to obtain the following powers of the source in Equation 4.13. This is known as the Point Spread Function which determines response of the array to the point source.

$$A_{jk} = \mathbf{w}_k^* \cdot \mathbf{C}_j \cdot \mathbf{w}_k \quad (4.13)$$

There exists several different methods to improve the beamforming results. CLEAN and DAMAS are two leading methods to improve the beamforming results but Pieter Sijtsma argues that these theoretical methods do not necessarily always improve results as they are not able to provide means of deconvolution.

Therefore, the empirical approach developed by Pieter Sijtsma is used for improving the beamforming results. It is assumed that the main and the side lobes are coherent in nature. Cross-powers of the source can be obtained from beamforming as in Equation 4.14.

$$B_{kj} = \frac{1}{2} \langle a_k a_j^* \rangle = \frac{1}{2} \frac{\mathbf{g}_k^*}{\|\mathbf{g}_k\|^2} \langle \mathbf{p} \mathbf{p}^* \rangle \frac{\mathbf{g}_j}{\|\mathbf{g}_j\|^2} = \mathbf{w}_k^* \mathbf{C} \mathbf{w}_j \quad (4.14)$$

Another assumption that is made is the coherent sources in close range to each other and the mirror sources as well are replaced with a single source which helps immensely in improving the beamforming results.

This can be written as in Equation 4.15.

$$\mathbf{w}_k^* \mathbf{C} \mathbf{w}_j = \mathbf{w}_k^* \mathbf{C}_j \mathbf{w}_j \quad (4.15)$$

The above equation is satisfied when, $\mathbf{C} \mathbf{w}_j = \mathbf{C}_j \mathbf{w}_j$ but there exists no solution for this \mathbf{C}_j .

To obtain a solution for \mathbf{C}_j , Equation 4.16 is written where \mathbf{h} refers to the steering vector which is determined empirically constructed from the sound coherence. Matrix \mathbf{H} comprises of the diagonal elements of $\mathbf{h} \mathbf{h}^*$.

$$\mathbf{C}_j = A_j \cdot (\mathbf{h} \mathbf{h}^* - \mathbf{H}) \quad (4.16)$$

Now this Equation can be input into $\mathbf{C} \mathbf{w}_j = \mathbf{C}_j \mathbf{w}_j$ and the simplification leads to Equation 4.17.

$$\mathbf{h} = \alpha \left(\frac{\mathbf{C} \mathbf{w}_j}{A_j} + \mathbf{H} \mathbf{w}_j \right) \quad (4.17)$$

α in Equation 4.17 is still unknown and needs to be solved. It is defined as in Equation 4.18.

$$\alpha = \frac{1}{\mathbf{h}^* \mathbf{w}_j} \quad (4.18)$$

To obtain the value of α , Equation 4.17 is multiplied by w_j^* which results in the following equation.

$$\mathbf{w}_j^* \mathbf{h} = \frac{1}{\alpha^*} = \alpha (1 + \mathbf{w}_j^* \mathbf{H} \mathbf{w}_j) \quad (4.19)$$

Simplification of Equation 4.19 leads to Equation 4.20.

$$|\alpha|^2 = \frac{1}{(1 + \mathbf{w}_j^* \mathbf{H} \mathbf{w}_j)} \quad (4.20)$$

Taking square roots on both sides result in Equation 4.21 and the solution for α is determined.

$$\alpha = \frac{1}{(1 + \mathbf{w}_j^* \mathbf{H} \mathbf{w}_j)^{\frac{1}{2}}} \quad (4.21)$$

Using Equation 4.21 and putting it back into Equation 4.17 yields the following equation. By using an iterative approach with the initial value using $\mathbf{h} = \mathbf{g}_j$, Equation 4.22 can be solved. Using Equation 4.13 and 4.18, point spread function for spatial coherence can be determined.

$$\mathbf{h} = \frac{1}{(1 + \mathbf{w}_j^* \mathbf{H} \mathbf{w}_j)^{\frac{1}{2}}} \left(\frac{\mathbf{C} \mathbf{w}_j}{A_j} + \mathbf{H} \mathbf{w}_j \right) \quad (4.22)$$

Beamforming results

By using the conventional beamforming approach with point spread function minimization and applying it to the microphone data, the beamform maps to obtain and analyse the presence of noise sources for different frequencies can be generated from the microphone data. Similar configurations and operational settings analysed for the Sound Pressure Level spectra are beamformed in this part of the report. Beamform maps for the other configurations can be found in Appendix D.2

Before the experiments were performed, speakers with two different frequencies at two different locations in the test section were analysed to make sure the microphones and the data acquisition system are working as expected. To make sure the correct working of the algorithms developed, beamform maps were generated for this speaker data before proceeding with the wings. Figure 4.20 contains the beamform maps for the speaker with 1000Hz and 5000Hz with speaker position at (0,0,0). From the plots for the speakers it can be seen there exists only two colour maps at 1000Hz and 5000Hz with other frequency plots being empty. This ensures the correct working of the beamforming algorithms after which these algorithms were applied to the microphone data of both conventional and the morphing wing.

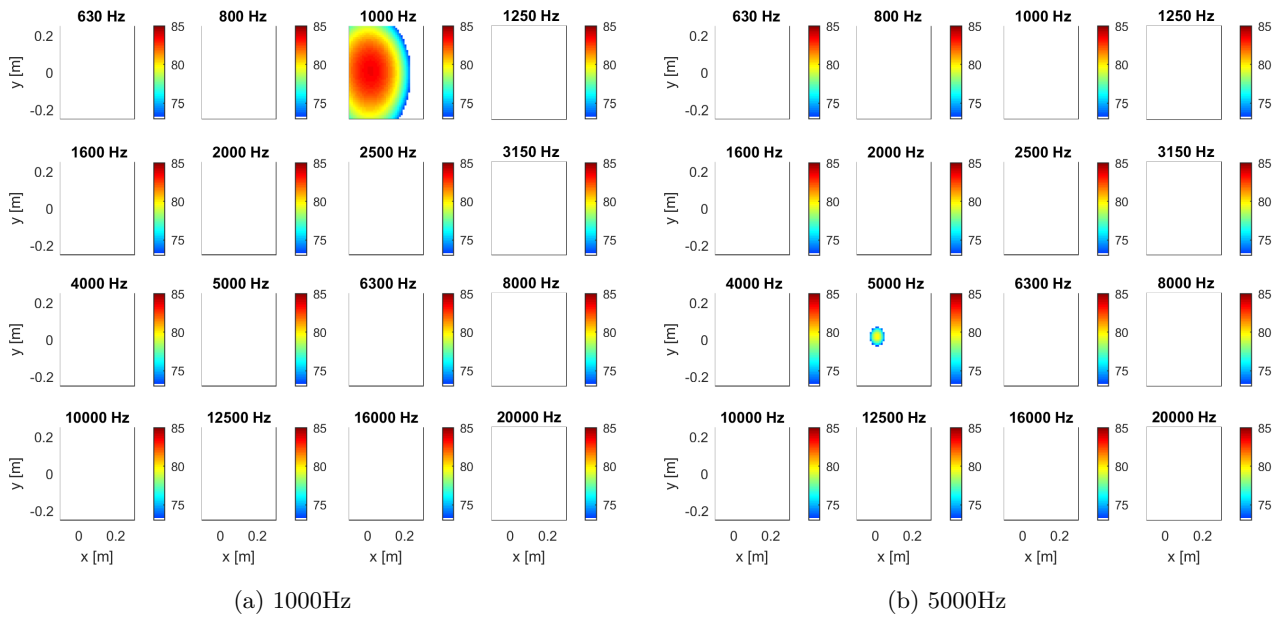


Figure 4.20: Beamform maps of speaker with two different frequencies and speaker position at (0,0,0)

For 35 m/s speed and the angles of attack of 8° , 10° and 12° , beamform maps for the conventional and morphed wings can be found in Figures 4.21, 4.23 and 4.25 respectively. For 50 m/s speed and the angles of attack of 8° , 10° and 12° , these can be found in Figures 4.22, 4.24 and 4.26 respectively. Beamform maps for other operational and configurational settings can be found in the Appendix. Beamform maps for the morphed and conventional wings are placed against each other to observe the differences in the local noise sources.

AOA = 8° and 35m/s

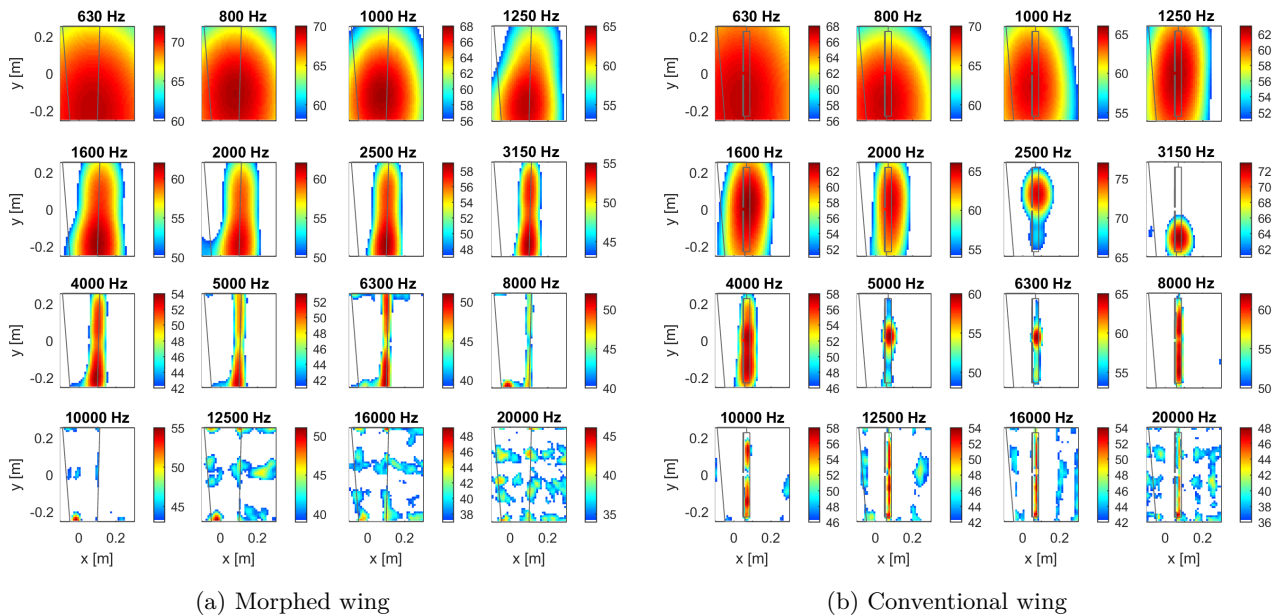


Figure 4.21: Beamform maps for the conventional and the morphing wing with an 8° angle of attack and 35m/s

AOA = 8° and 50m/s

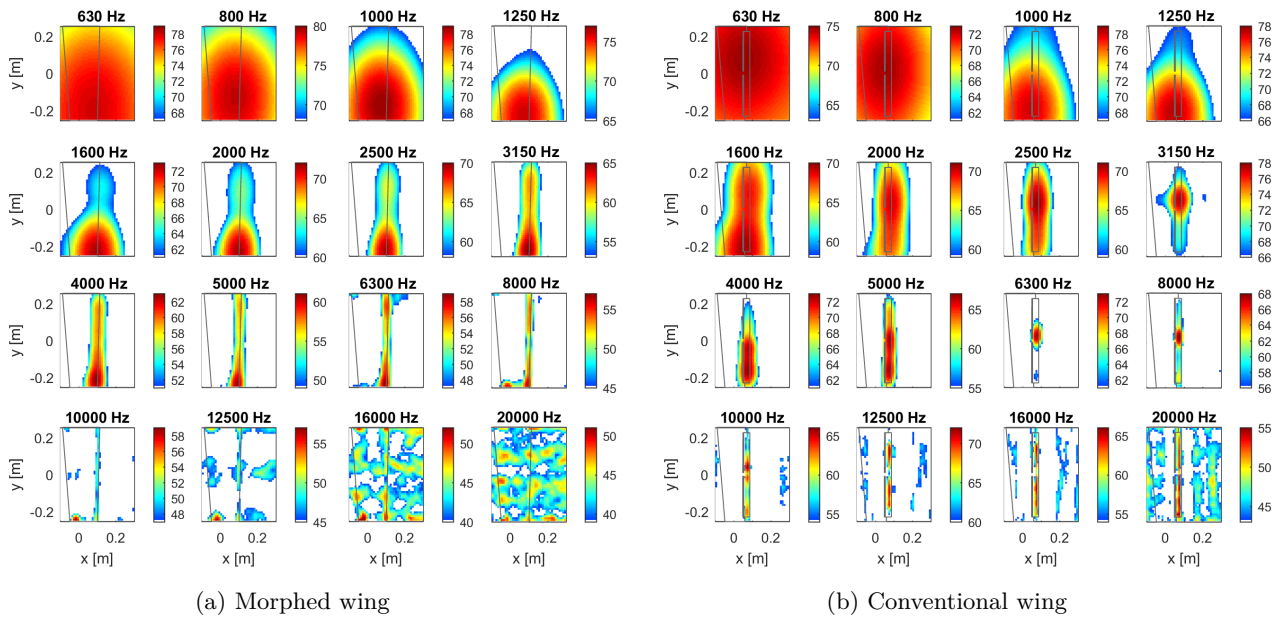


Figure 4.22: Beamform maps for the conventional and the morphing wing with an 8° angle of attack and 50m/s

AOA = 10° and 35m/s

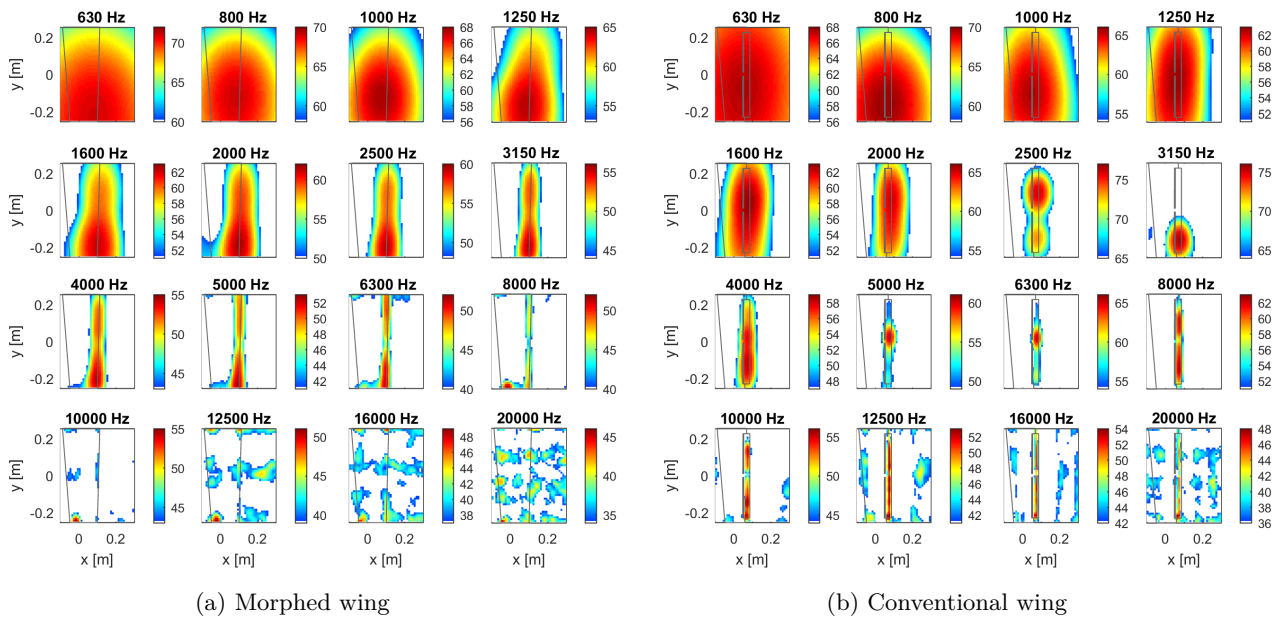


Figure 4.23: Beamform maps for the conventional and the morphing wing with a 10° angle of attack and 35m/s

AOA= 10° and 50m/s

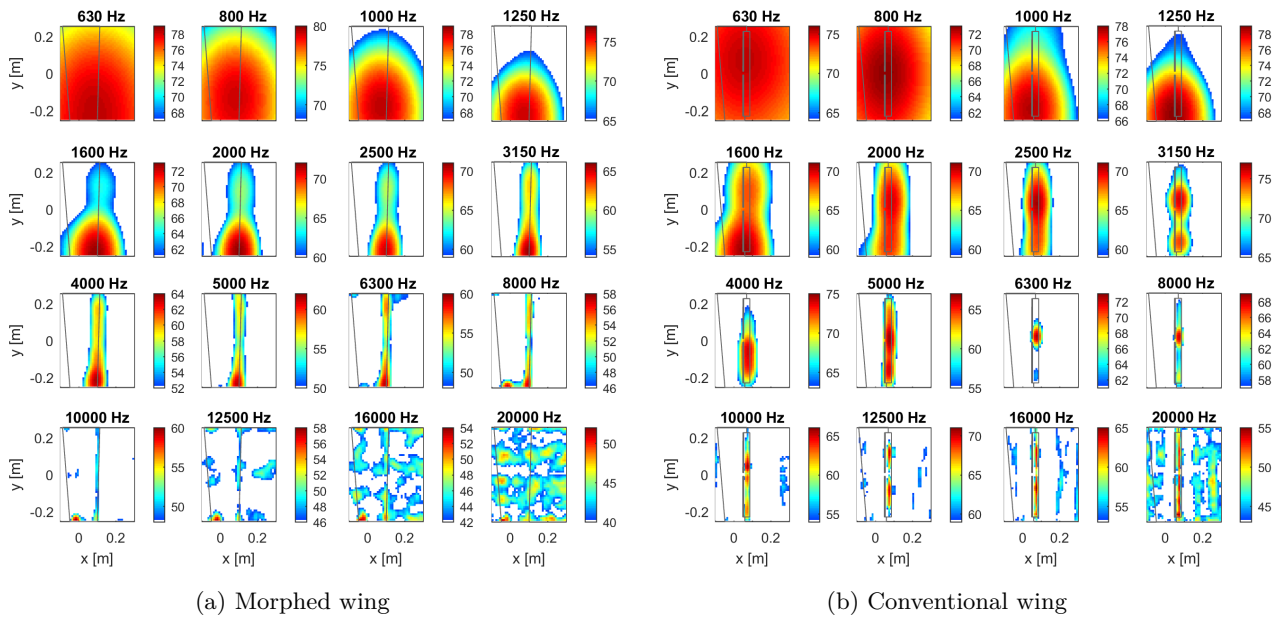


Figure 4.24: Beamform maps for the conventional and the morphing wing with a 10° angle of attack and 50m/s

AOA= 12° and 35m/s

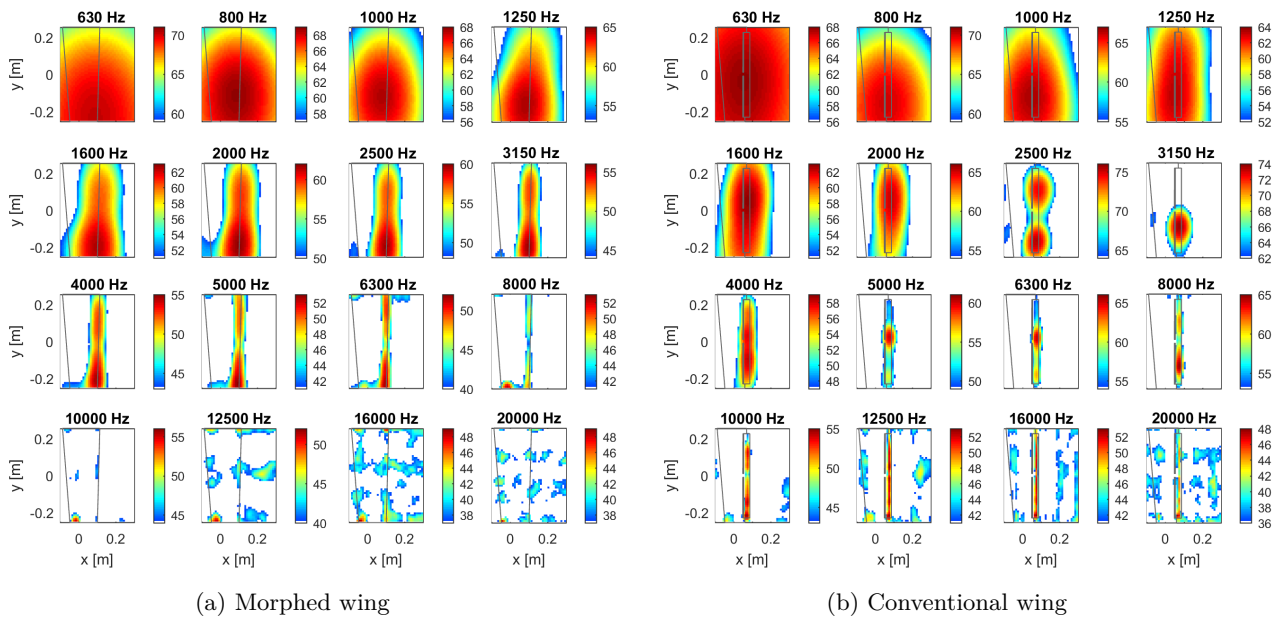


Figure 4.25: Beamform maps for the conventional and the morphing wing with a 12° angle of attack and 35m/s

AOA= 12° and 50m/s

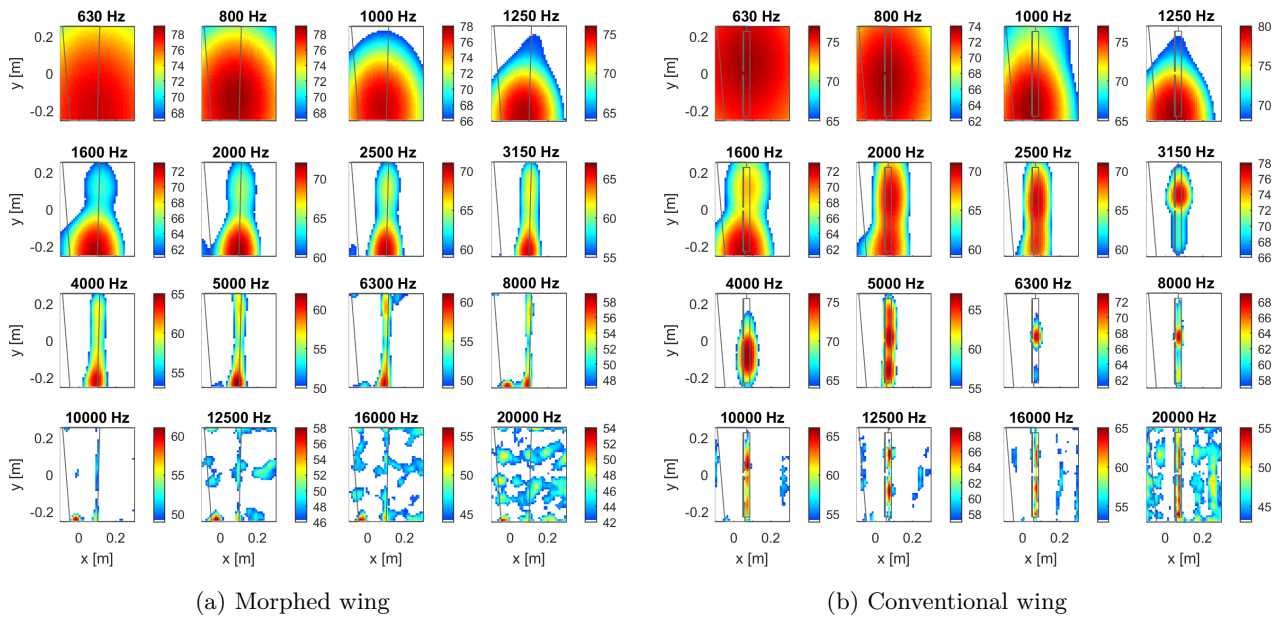


Figure 4.26: Beamform maps for the conventional and the morphing wing with a 12° angle of attack and 50m/s

Discussion of beamform maps

By using the conventional beamforming approach together with point spread function minimization and applying it to the microphone data, the beamform maps are generated for the microphone data. In the beamform maps, the wings are highlighted in the background for each frequency which helps in locating the noise sources on the wing. 16 one-third octave band center frequencies starting from 630Hz up to the hearing limit of 20kHz were analysed. For the 630 Hz and 800 Hz the low frequency noise is higher for the morphing wing due to the larger size of the wing and the small imperfections.

At 1600 Hz the noise generation due to the geometrical imperfections and taping of wing root with the interface is dominant. From 1600Hz onwards, the noise generation from the trailing edge deflection for the morphing wing and flap for the conventional wing are the main noise sources. For the beamform maps of conventional wing, wing-flap bracket at the center of the wing is generating additional noise peaks at the frequency of 6300 and 8000 Hz. From 4000Hz to 8000Hz other noise sources due to the geometrical imperfections are dampened out and the trailing edge noise from the wings is dominant. Between 10kHz to 20kHz at high frequencies, trailing edge of the morphing wing is no longer a dominant noise source whereas for the conventional wing the flap gaps are still very much the main noise generation source.

4.3 Analytical Aero-Acoustic Noise Analysis

Numerical simulation models such as Computational Aero-Acoustics (CAA) are high fidelity software that models the near-field and far-field noise produced by an aerodynamic source. Navier-Stokes equations for aerodynamics and acoustic wave equations for the propagation of the waves(acoustic) are combined together and used in these high-fidelity software. These software provide noise predictions up to high accuracy due to very few assumptions used but due to immense computational costs their application is limited to only simple geometries.

Due to the huge computational costs of high-fidelity software, noise modeling during the aircraft design is done by using the models that have relatively lower computational costs. These models provide decent accuracy during the initial design of the aircraft and these models range from purely theoretical,

semi-empirical to experimental data.

In this section, noise prediction technique has been used in order to approximate the noise generated by the morphing and the conventional wing. From the study of both Martin Fink's noise prediction tool and the Werner Dobrzynski's noise prediction tool during the literature study, it was concluded that both models predict noise up to sufficient accuracy. Therefore, after detailed discussions within the Faculty's lecturers Dr. ir. Sahai and Dr. ir. Bertsch it was decided to continue with the **Werner Dobrzynski's** method for thesis work. This was purely based on the ability of the model to adapt to morphing of the wing where it includes the wing chord along with the directivity. During flap morphing, there is only a clean airfoil with extra trailing edge directivity when high lift is required.

4.3.1 Werner Dobrzynski's noise prediction model

This model was developed at the German Aerospace Center (DLR) and at NASA by David P. Lockard and Christopher J. Miller. Only a clean airfoil and trailing edge device (flaps) are studied here according to the requirement of the thesis work.

Sound Pressure Level spectrum using Werner Dobrzynski's noise approximation model depends upon the summation of various individual terms. These include spectral Shape Function ($\Delta L_{spec}(Str)$), Velocity dependent term (ΔL_{vel}), Geometry dependent term (ΔL_{geo}), Normalized reference level (L_{norm}) and Directivity term (ΔL_{dir}). All these terms are computed for a clean airfoil and a trailing edge device in the subsequent sections.[9]

Formulation of total Sound Pressure Level using the individual terms is shown in Equation (4.23).

$$L_{\theta}(Str) = \Delta L_{spec}(Str) + \Delta L_{geo} + L_{norm} + \Delta L_{vel} + \Delta L_{dir} \quad (4.23)$$

Strouhal number is the dimensionless frequency. For Werner Dobrzynski's model it is defined as $Str = f \cdot x_{ref} / v_{ref}$ where f refers to the frequency, x_{ref} refers to the reference dimension of noise source and v_{ref} is the reference velocity.

Clean airfoil

Clean airfoil noise past the trailing edge is generated due to the convection of the turbulent flow. Similar noise generation phenomenon occurs at the tail surfaces. Thickness of the boundary layer is used for the turbulent length scale. Figure 4.27 illustrates the noise generation phenomenon due to the convection of turbulent flow.

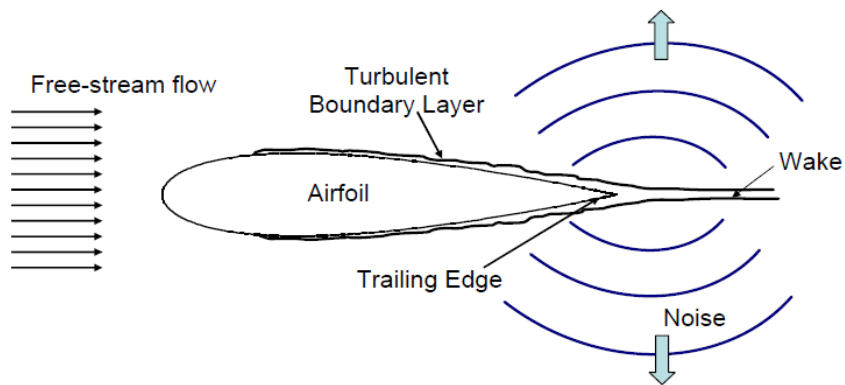


Figure 4.27: Clean airfoil noise at the trailing edge generated due to turbulent flow [40]

Following are the equations, that are being used for modelling of the clean airfoil noise. Some of the equations have already been simplified before presenting here. These equations are taken from the PhD work of Lothar Bertsch at the German Aerospace Center [9].

To be able to compute the Sound Pressure Level due to normalized reference level, geometry and velocity dependent term, acoustic intensity (I) needs to be determined. Formulation for acoustic intensity can be found in Equation (4.24).

$$I = \frac{1.7}{2\pi^3} \cdot \frac{\rho_\infty}{c_\infty^2} \cdot v_m^5 \cdot \frac{l_a \Delta w}{d^2} \cdot \left[\left(\frac{u_0}{v_m} \right)^5 \cdot \frac{\delta}{\delta^*} \right]_{TE} \cdot \cos^3(\psi) \quad (4.24)$$

In Equation (4.24), v_m represent the mean inflow velocity, c is the ambient speed of sound, l_a and Δw refer to mean airfoil length and element length respectively. u_0 is the characteristic velocity scale, v_m refers to the mean inflow velocity, δ is the boundary layer thickness, δ^* is displacement(turbulent flow) thickness and ψ is the trailing edge sweep angle for that particular element.

Ratio between the boundary layer thickness and displacement thickness is assumed to be 8 as suggested in [9]. There exists two values for the ratio $(\frac{u_0}{v_m})$ based on the Lockard's approach and Dobrzynski's approach. Lockard used a value of 0.066 whereas Dobrzynski used 0.046 and due to this difference, Lockard predicted about 8dB higher Sound Pressure Level. Lockard also did not make use of the trailing edge sweep angle in his approach whereas Dobrzynski did take into account the effect of the trailing edge sweep. Use of this trailing edge sweep angel results in a higher Sound Pressure Level (about 1.9dB for 30°). Dobrzynski's approach is used in this study and a value of 0.046 is used for the ratio between the boundary layer thickness and the displacement thickness. The trailing edge sweep angle is also incorporated.

Using the above approach, the Equation (4.24) can be simplified. Simplified equation can be found in Equation (4.25).

$$I = \frac{8 \cdot 1.7}{2\pi^3} \cdot \frac{\rho_\infty}{c_\infty^2} \cdot v_m^5 \cdot \frac{l_a \Delta w}{d^2} \cdot 0.046^5 \cdot \cos^3(\psi) \quad (4.25)$$

Sound Pressure Level due to the normalized reference level, geometry and velocity dependent term is computed using Equation (4.26). This equation is normalized by using the reference acoustic intensity and value for it is $10^{-12} W/m^2$. Acoustic intensity has already been determined in the previous equation.

$$L_{norm/vel/geo} = 10 \cdot \log_{10} \left(\frac{I}{I_{ref}} \right) = 120 + 10 \cdot \log_{10}(I) \quad (4.26)$$

Sound Pressure Level increment due to the directivity term depends only on the wing dihedral angle(ν) and the lateral emission angle (β). Its formulation can be found in Equation (4.27).

$$\Delta L_{dir} = 10 \cdot \log_{10} \left(\frac{|\cos(\beta^* - \nu)| + |\cos(\beta^* + \nu)|}{2} \right) \quad (4.27)$$

Spectral shape function is now calculated using the Equations (4.28) and (4.29). The Equation (4.28) is used in case when the Strouhal number is less than the maximum Strouhal number and Equation (4.29) is used when Strouhal number is higher than the maximum Strouhal number.

$$\Delta L_{spec}(Str) = 10 \cdot \log_{10} \left(\frac{Str}{Str_{max}} \right) - 9.0dB \quad for \quad Str \leq Str_{max} \quad (4.28)$$

$$\Delta L_{spec}(Str) = 10 \cdot \log_{10} \left(\frac{Str_{max}}{Str} \right) - 9.0dB \quad for \quad Str > Str_{max} \quad (4.29)$$

From Equations (4.28) and (4.29), maximum Strouhal number is an unknown which is computed using the following Equation.

$$Str_{max} = \frac{13.6}{0.74\pi} \cdot \frac{u_0}{v_m} \cdot \sqrt[5]{\frac{v_m l_a}{v_\infty}} \quad (4.30)$$

Finally, the overall Sound Pressure Level can be determined by the summation of all the above discussed individual terms.

$$L_{dc}(Str) = L_{norm/vel/geo} + \Delta L_{dir} + \Delta L_{spec}(Str) \quad (4.31)$$

Flaps

In this part of the report, noise prediction technique for trailing edge device (flaps) is discussed. Due to the use of flaps, approach used in this section is adapted and made applicable to the airfoils with a high wing loading. Werner Dobrzynski's approach is used again and a value of 0.046 is used for the ratio between the boundary layer thickness and the displacement thickness is incorporated and is adjusted accordingly to the high lift coefficients. The original equation can be found in (4.32).

$$\left[\frac{u_0}{v_m} \right]_{TE,cl_c} \approx 0.046 \quad (4.32)$$

Lockard [23] suggested in his approach that δ^* is not equal to y_m , therefore new scaling of boundary layer thickness is adjusted according to the location at which maximum kinetic energy is applied. All scaling factors are based on the NACA 4412 experimental data collected by Lockard. Following three equations presents the approach adjusted for high lift coefficients.

$$\left[\frac{\delta}{y_m} \right]_{TE,cl_f} \sim \frac{10.0}{\left(1 + \frac{cl_c^2}{4}\right)} \quad (4.33)$$

$$\left[\frac{u_0}{y_m} \right]_{TE,cl_f} \sim \left[\frac{u_0}{v_m} \right]_{TE,cl_c} \cdot \left(1 + \frac{cl_c^2}{4}\right) \sim 0.046 \cdot \left(1 + \frac{cl_c^2}{4}\right) \quad (4.34)$$

Equation (4.35) shows formulation of the correlation between the low wing loading and the high high loading due to flap deployment.

$$\left[\left(\frac{u_0}{y_m} \right)^5 \cdot \frac{\delta}{y_m} \right]_{TE,cl_f} = \frac{10}{8} \cdot \left(1 + \frac{cl_c^2}{4}\right)^4 \cdot \left[\left(\frac{u_0}{y_m} \right)^5 \cdot \frac{\delta}{y_m} \right]_{TE,cl_c} \quad (4.35)$$

Now the formulation of acoustic intensity for the trailing edge device can be determined. It can be seen in Equation (4.36) where l_a and l_f refers to chord lengths of the airfoil and the deployed flap respectively.

$$I = \frac{1.7}{2\pi^3} \cdot \frac{\rho_\infty}{c_\infty^2} \cdot v_m^5 \cdot \frac{(l_a + l_f) \cdot \Delta w}{d^2} \cdot \cos^3(\Psi) \cdot \left[\left(\frac{u_0}{y_m} \right)^5 \cdot \frac{\delta}{y_m} \right]_{TE,cl_f} \quad (4.36)$$

Equations (4.37) and (4.38) shows simplified form of Equation (4.36) by using the Equations (4.33), (4.34) and (4.35).

$$I = \frac{1.7}{2\pi^3} \cdot \frac{\rho_\infty}{c_\infty^2} \cdot v_m^5 \cdot \frac{(l_a + l_f) \cdot \Delta w}{d^2} \cdot \cos^3(\Psi) \cdot \frac{10}{8} \cdot \left(1 + \frac{cl_c^2}{4}\right)^4 \cdot \left[\left(\frac{u_0}{y_m} \right)^5 \cdot \frac{\delta}{y_m} \right]_{TE,cl_c} \quad (4.37)$$

$$I = \frac{1.7}{2\pi^3} \cdot \frac{\rho_\infty}{c_\infty^2} \cdot v_m^5 \cdot \frac{(l_a + l_f) \cdot \Delta w}{d^2} \cdot \cos^3(\Psi) \cdot 0.046^5 \cdot \left(1 + \frac{cl_c^2}{4}\right)^4 \quad (4.38)$$

After inputting parameters for high wing loading, Sound Pressure Level due to normalized reference level, velocity and geometry can be formulated as in Equation (4.39).

$$L_{norm/vel/geo} = 120dB + 10 \cdot \log_{10} \left(\frac{1.7}{2\pi^3} \cdot \frac{\rho_\infty}{c_\infty^2} \cdot v_m^5 \cdot \frac{(l_a + l_f) \cdot \Delta w}{d^2} \cdot \cos^3(\Psi) \right) + 10 \cdot \log_{10} \left(\frac{10}{8} \cdot \left(1 + \frac{cl_c^2}{4}\right)^4 \cdot \left[\left(\frac{u_0}{y_m} \right)^5 \cdot \frac{\delta}{y_m} \right]_{TE,cl_c} \right) \quad (4.39)$$

Equation (4.39) can be further simplified into Equation (4.40) with separate term indicating the extra Sound Pressure Level due to increased wing loading.

$$L_{norm/vel/geo} = 120dB + 10 \cdot \log_{10} \left(\frac{8 \cdot 1.7}{2\pi^3} \cdot \frac{\rho_\infty}{c_\infty^2} \cdot v_m^5 \cdot \frac{(l_a + l_f) \cdot \Delta w}{d^2} \cdot \cos^3(\Psi) \cdot (0.046 \cdot v_m)^5 \right) + 10 \cdot \log_{10} \left(\frac{10}{8} \cdot \left(1 + \frac{cl_c^2}{4}\right)^4 \right) \quad (4.40)$$

where the following term corresponds to the high lift case:

$$10 \cdot \log_{10} \left(\frac{10}{8} \cdot \left(1 + \frac{cl_c^2}{4} \right)^4 \right)$$

This can further be simplified into the following equation.

$$\Delta L_{cl_f} = 0.97 + 40 \cdot \log_{10} \left(\left(1 + \frac{cl_c^2}{4} \right)^4 \right)$$

The directivity and spectral terms in this case are similar to the clean airfoil so Equations (4.27) and (4.29) are used to determine the total Sound Pressure Level. Sound Pressure Level can be determined using Equation (4.41).

$$L_{cl_f} = L_{norm/vel/geo}(cl_f) + \Delta L_{dir} + \Delta L_{spec}(Str) \quad (4.41)$$

4.3.2 Flap Side-Edge noise prediction and modelling

Flap side-edge noise contributes significantly to the overall Sound Pressure Level of an aircraft. As of today, Fink's model and the Werner Dobrzynski's model do not have the flap side-edge contribution incorporated in the noise approximation tool. To correctly validate the predicted data with the experimental data, flap side-edge noise is modelled and incorporated in to the Robert Dobrzynski's noise approximation model.

Vortex generation due to flap side-edge results in the overall increase of wing noise. As the flap side-edge vortex are efficient radiators of noise therefore the noise generated due to it is quite significant. Vortex structures resulting due to deployment of a flap are shown in Figure 4.28.

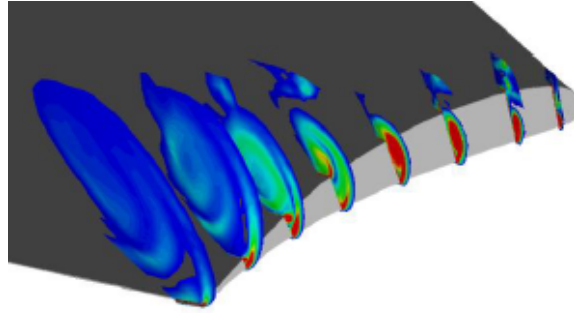


Figure 4.28: Vortex structures at flap side-edge due to flap deployment [14]

Flap side-edge noise prediction method developed by Karl-Stephane Rossignol at the German Aerospace Center (DLR) is be used for predicting noise due to the flap side-edge [37]. Sound pressure level is comprised of two different terms namely the noise spectral shape and the noise directivity. This formulation can be found in Equation (4.42) [35].

$$SPL_{fse} = SPL_n(St_c)|_{St_c \leq 25} + SPL_n(St_c)|_{St_c > 25} + D(\theta, \phi)|_f \quad (4.42)$$

A step by step approach to predict the flap side-edge noise is discussed below. Values for all the coefficients corresponding to a certain frequency can be found in Reference [37].

Flap Side-Edge noise spectral shape

Rossignol developed an empirical model based on the various experimental data for flap side-edge noise models. Cross-flow velocity is first determined in Equation (4.43) which is basically the velocity component in the spanwise direction. It is normalized with the free-stream velocity (U_0).

$$\frac{U_c}{U_0} = \frac{0.0316 \cdot \delta_f}{\delta_{ref}} + 0.1879 \quad (4.43)$$

δ_f in the Equation (4.43) is the flap deflection angle whereas δ_{ref} refers to the reference deflection angle for which Rossignol used a value of 1° . Normalized spectra for the flap side-edge noise is determined in Equation (4.44).

$$SPL_n = SPL + 20 \cdot \log_{10}(r/c) - 55 \cdot \log_{10}(U_c/U_{ref}) \quad (4.44)$$

In Equation (4.44), r/c is the ratio between the observer distance and the flap chord length and U_c/U_{ref} is the ratio between cross-flow velocity determined in Equation (4.43) with arbitrary reference velocity of 100m/s .

Rossignol then derived an approximation for the flap side-edge noise spectral using the above discussed relations. A least square fit was plotted through all the data points. This approximation is not directly dependent on the free stream velocity or flap deflection angle but on the flap chord Strouhal number. Strouhal number based on the flap chord is determined in Equation (4.45).

$$St_c = \frac{f \cdot c}{U_c} \quad (4.45)$$

In Equation (4.45), f is the one-third octave band center frequency, U_c is the cross-flow velocity which was determined in Equation (4.43) and c is the flap chord length.

Noise spectra are determined for two different range of Strouhal numbers. For Strouhal numbers equal to or less than 25, the noise spectral is determined via Equation (4.46) and for Strouhal numbers greater than 25 the Equation (4.47) should be used.

$$SPL_n(St_c)|_{St_c \leq 25} = l_0 + l_1 \cdot St_c + l_2 \cdot St_c^2 + l_3 \cdot St_c^3 + l_4 \cdot St_c^4 + l_5 \cdot St_c^5 + l_6 \cdot St_c^6 \quad (4.46)$$

$$SPL_n(St_c)|_{St_c > 25} = h_0 + h_1 \cdot St_c + h_2 \cdot St_c^2 + h_3 \cdot St_c^3 \quad (4.47)$$

Flap Side-Edge noise directivity

Directivity contribution to the Sound Pressure Level is adjusted to the microphones angle setting thus emission angle and frequency. Directivity similarly to the spectral modelling is not directly dependent on the flap deflection angle. For detailed procedure to compute the coefficients, the reader can refer to [37].

Directivity term for flap side-edge noise is dependent directly upon the polar(ϕ) and azimuthal angle(θ). It can be determined using Equation (4.48).

$$D(\theta, \phi)|_f = m_0 + m_1 \cdot \theta + m_2 \cdot \theta^2 + m_3 \cdot \theta^3 + k_0 + k_1 \cdot \phi + k_2 \cdot \phi^2 + k_3 \cdot \phi^3 \quad (4.48)$$

4.3.3 Results and comparison to the experimental data

Only the Overall Sound Pressure Levels from the analytical prediction techniques are discussed in this report. Similar geometrical and operational settings as in the experimental data are used in the noise prediction techniques. Results for only 50 m/s speed have been determined using the noise prediction simulations. For the morphing wing, clean airfoil with an additional directivity contribution due to the trailing edge deflection is added. For the conventional wing, summation of the clean airfoil, flap and the flap side-edge noise contribution is done to obtain the noise generation. Lateral and longitudinal directivity and the distance of the microphone 1 from the experiments is used in the noise prediction. Table 4.6 contains the Overall Sound Pressure Level for both wings at 50m/s and at different AOA's.

Table 4.6: Comparison of predicted Overall Sound Pressure Level between both wings

Operational setting	$OSPL_{conv.}$ [dB]	$OSPL_{morph.}$ [dB]	$OSPL_{conv.-morph.}$ [dB]
V=50m/s & AOA= 0°	69.12	65.11	66.9
V=50m/s & AOA= 2°	69.22	65.19	67.6
V=50m/s & AOA= 4°	69.68	65.37	67.8
V=50m/s & AOA= 6°	70.03	65.42	68.2
V=50m/s & AOA= 8°	70.43	65.53	68.7
V=50m/s & AOA= 10°	71.00	65.59	69.5
V=50m/s & AOA= 12°	71.12	65.63	69.7

From the table, predicted/approximated Overall Sound Pressure Levels for the morphing and the conventional wing can be found. It can be noticed from the table that the conventional wing generates higher Overall Sound Pressure Levels than the morphing wing at all angles of attack, which is similar to the experimental data. The percentage reduction in the Overall Sound Pressure Level by replacing the conventional flaps with the morphing surfaces can be obtained by converting decibels to sound pressures and then computing the percentage differences.

From the predicted data, it can be evaluated that the minimum percentage difference between both wings in the Overall Sound Pressure Level generation is 36% at the lowest analysed angle of attack of 0° and highest at the angle of attack of 12° where the difference amounts to 45%. Comparing these values to the percentage reduction of the experimental results, it can be noticed that the predicted data results in 10-15% additional reduction in the Overall Sound Pressure Level for the morphing wing. For the conventional wing, designed flap brackets as seen in the beamform maps results in additional noise production which could be seen as the reason of this increase in the Overall Sound Pressure Level differences. The flap bracket was required for the conventional wing to avoid any structural damage to the flap.

By comparing Table 4.6 with Table 4.4, it can be noticed that the noise prediction tools predict lower Overall Sound Pressure Levels than the experiments. A reason for this could be the windtunnel and the background noise present in the test section that causes this difference in the values. Another reason could be the additional noise generation due to the horseshoe vortices generated at the test section edges. The noise generated due to geometry imperfections also contributes to this difference. Overall, the differences in the experimental and the predicted data indicates reduction in the generation of the noise after flap morphing.

The noise prediction techniques provide a computationally quick with decent level accuracy to approximate the noise of the wing during initial design of the aircraft. From the results it can be concluded that these are also capable of predicting the noise generation for the morphing wings as well with decent accuracy.

5. Radar Cross-Section Analysis & Evaluation

This Chapter elaborates on the Radar Cross-Section merits aspect of the morphing and the conventional wings. Structure of the chapter is such that the theoretical background of Radar Cross-Section is discussed first followed by the selection of the Radar Cross-Section measurement software. Subsequently, discussion about the solvers of the measurement software, their suitability and selection for the study are explained afterwards followed by the radar signatures of the wings for different configurations and settings. Lastly, validation of the simulations is discussed in the last section of the Chapter.

RADAR itself is an acronym for *R*adio *D*etection *A*nd *R*anging. It has been more than a century ago when the phenomenon of radio waves being reflected against objects was observed. In the early experiments continuous waves were used and detection of the target was only determined after reflection of the transmitted wave. Drawback of continuous waves is that they do not provide any information about the range. An illustration of the continuous wave radar phenomenon is shown in Figure 5.1¹.

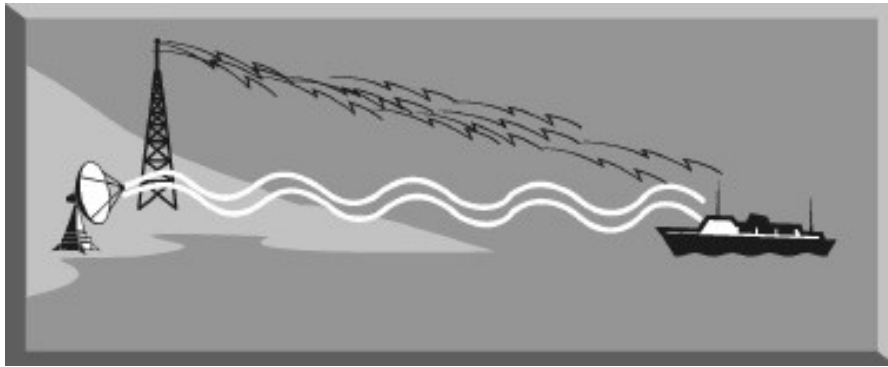


Figure 5.1: Continuous wave radar operation

In order to prevent this lack of information, advancements were made to send numerous short pulses instead of a continuous wave. Due to this, the time difference between the transmitted pulse and the return of its echo provided the information about range. This phenomenon has been illustrated in Figure 5.2².

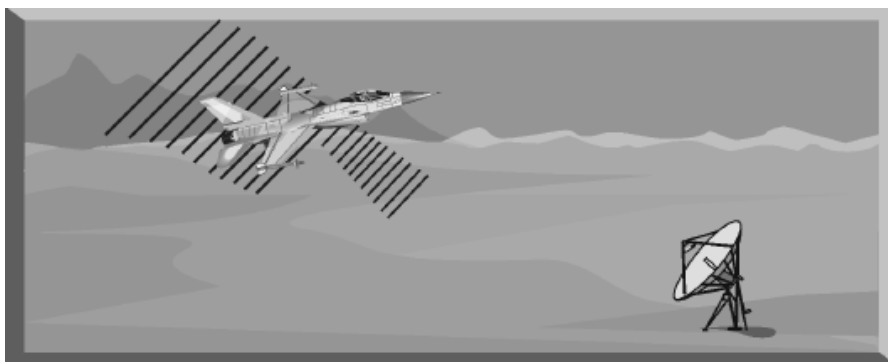


Figure 5.2: Pulse radar operation

¹URL:<https://basicsaboutaerodynamicsandavionics.wordpress.com/2016/04/13/radar-electronic-countermeasure/>
[Cited 13-Apr-2018]

²URL:<https://basicsaboutaerodynamicsandavionics.wordpress.com/2016/04/12/radar-electronic-countermeasure/>
[Cited 12-Apr-2018]

There are different sources present on an aerial vehicle that are a source of radar reflection. To be able to study radar reflections and optimize vehicle capability to avoid them one needs to know these sources. Figure 5.3³ illustrates radar reflection sources on a fighter aircraft

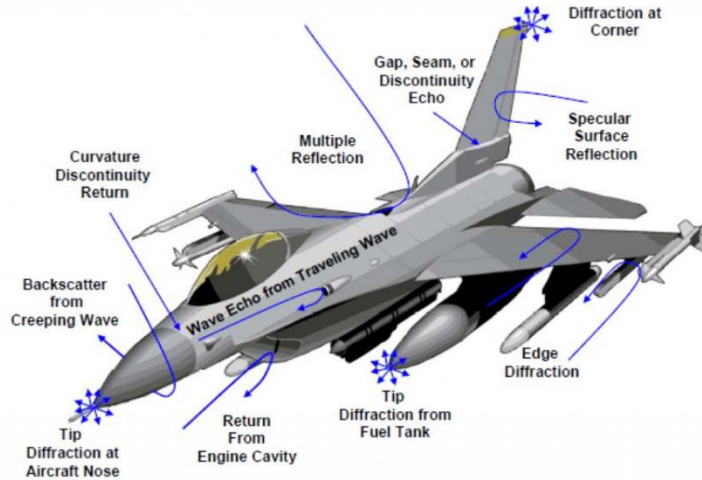


Figure 5.3: Radar reflection sources on a fighter aircraft

5.1 RCS theoretical background

In this section, basic fundamentals to determine Radar Cross-Section and radar range are determined. Below are the derivations that leads to the desired parameters of interest. During the process it is assumed that there is no dispersion during propagation which means that electromagnetic waves propagate in ideal conditions. Step by step calculation guide is studied through Reference [30] and the radar tutorials⁴⁵⁶⁷.

First of all, non-directional power density is determined in the Equation (5.1).

$$S_u = \frac{P_s}{4\pi R_1^2} \quad (5.1)$$

In the Equation (5.1), P_s refers to the transmitted power and R_1 is the range(antenna-aim). If the distribution of the radiated power is not equal in all directions, this results in the antenna gain. Antenna gain can be computed using the Equation (5.2).

$$S_g = S_u \cdot G \quad (5.2)$$

In the Equation (5.2), G refers to the antenna gain and S_g is the directional power density. To successfully detect a target not only directional power density is necessary but also the power that is reflected in direction of radar. Here comes in use the Radar Cross-Section (σ).

Reflected power can be calculated using Equation (5.3).

$$P_r = \frac{P_s}{4 \cdot \pi \cdot R_1^2} \cdot G \cdot \sigma \quad (5.3)$$

Reflected power in the Equation (5.3) depends on the transmitted power (P_s), range(antenna-aim) (R_1), antenna gain (G) and the Radar Cross-Section (σ). Equation (5.4) shows to determine the Radar

³URL:<https://basicsaboutaerodynamicsandavionics.wordpress.com/2016/04/14/radar-electronic-countermeasure/> [Cited 14-Apr-2018]

⁴URL:<http://www.radartutorial.eu/01.basics/Radar%20Principle.en.html> [Cited 23-Apr-2018]

⁵URL:<http://www.radartutorial.eu/01.basics/The%20Radar%20Range%20Equation.en.html> [Cited 25-Apr-2017]

⁶URL:<http://www.radartutorial.eu/05.bistatic/bs04.en.html> [Cited 29-Apr-2018]

⁷URL:<http://www.radartutorial.eu/01.basics/Radar%20Cross%20Section.en.html> [Cited 30-Apr-2018]

Cross-Section of a target. S_t is the power density which is being intercepted by the target and S_r is the total scattered power density in the region of range (r).

$$\sigma = \frac{4\pi r^2 S_r}{S_t} \quad (5.4)$$

Figure 5.4, clarifies all the terms and connections used in the equations.

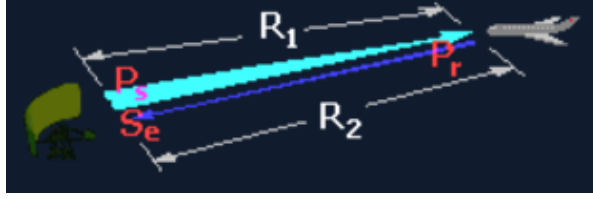


Figure 5.4: Connection between different terms in the equations used

Reflected power is also referred as the emitted power by the target. By using this phenomenon the received/yielded power density at receiver becomes as below.

$$S_e = \frac{P_r}{4\pi R_2^2} \quad (5.5)$$

In Equation (5.5), S_e is the received power density, P_r is the power reflected and R_2 is the range(aim-antenna) in metres.

Received power can now be derived after determining received power density. This can be found in Equation (5.6).

$$P_E = S_e \cdot A_W \quad (5.6)$$

In Equation (5.6), A_W is the effective antenna aperture which can be computed using the following equation.

$$A_W = A \cdot K_a \quad (5.7)$$

Equation (5.7) determines the effective antenna aperture where A is the geometrical area of the antenna and K_a is the antenna efficiency. Based on the literature, generally a value between 0.6 and 0.7 is assumed for the antenna efficiency.

By using the above derived relation for effective antenna aperture, received power relation can be rewritten as following in Equation (5.8).

$$P_E = \frac{P_r}{4 \cdot \pi \cdot R_2^2} \cdot A \cdot K_a \quad (5.8)$$

Now, both transmitted and the received power can be combined together to rewrite the power received equation. Equation (5.3) is input into Equation (5.8) and after simplifications, the resulting equation is shown in Equation (5.9).

$$P_E = \frac{P_S \cdot G \cdot \sigma}{(4 \cdot \pi)^2 \cdot R^4} \cdot A \cdot K_a \quad (5.9)$$

Another relation to present the antenna gain (G) in terms of wavelength is shown in Equation (5.10).

$$G = \frac{4\pi \cdot A \cdot K_a}{\lambda^2} \quad (5.10)$$

Again, by making antenna area (A)the subject in the equation and replacing in the Equation (5.9) results in Equation (5.11) which can be seen below.

$$P_E = \frac{P_S \cdot G^2 \cdot \sigma \cdot \lambda^2}{(4\pi)^3 \cdot R^4} \quad (5.11)$$

Radar equation can be obtained by making range (R) the subject and solving for it. It can be found in Equation (5.12).

$$R = \sqrt[4]{\frac{P_S \cdot G^2 \cdot \lambda^2 \cdot \sigma}{P_E \cdot (4\pi)^3}} \quad (5.12)$$

From the above relation it can be noticed that the maximum range (R_{max}) is achieved at the minimum power detection. P_S , G and λ are considered to be constant as they do not vary in large ranges.

To incorporate the losses in the range of the radar, Equation (5.12) is adapted a little. L_{ges} is added in the denominator which includes the loss factors. New relation for range is mentioned in Equation (5.13).

$$R = \sqrt[4]{\frac{P_S \cdot G^2 \cdot \lambda^2 \cdot \sigma}{P_E \cdot (4\pi)^3 \cdot L_{ges}}} \quad (5.13)$$

In Equation (5.13), L_{ges} is the new term comprises of the L_f , L_D and L_{Atm} . L_f is the term that take into account the reflection fluctuation losses. L_D is the radar attenuation factors for both receiving and transmitting paths. L_{Atm} are the atmospheric losses of the waves during propagation both ways.

5.1.1 Mono-static RCS

Equations used in Section 5.1 are derived for mono-static Radar Cross-Section which is the conventional configuration. Mono-static radar term is used to distinguish from the bi-static radar.

Figure 5.5⁸ depict the working of a mono-static radar where the receiver and the transmitter radar are collocated and share a same antenna.

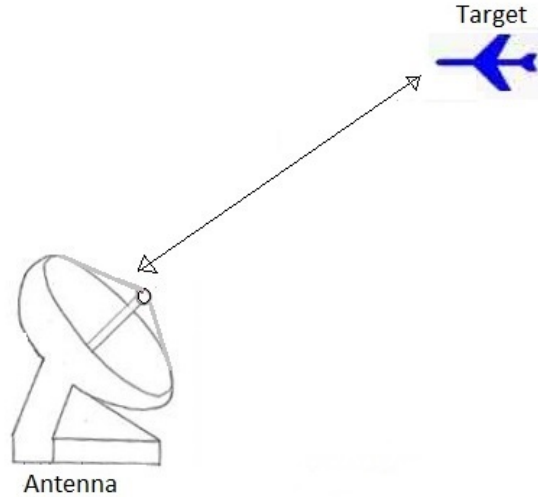


Figure 5.5: Mono-static Radar

5.1.2 Bi-static RCS

Bi-static radar consists of a system where the receiver and the transmitter are separated by a certain distance. Usually this distance between transmitter and the receiver is large and also a higher parallax. This means that even if there are no signals transmitted towards the mono-static radar antenna, there

⁸URL:<http://www.rfwireless-world.com/Terminology/Monostatic-radar-vs-Bistatic-radar.html> [Cited 18-Apr-2017]

is still a chance that the signals can be received indicating presence of the target.

Figure 5.6⁹ demonstrates the working of a bi-static radar where the receiver and the transmitter radar are separated by a certain distance and also have separate antennas.

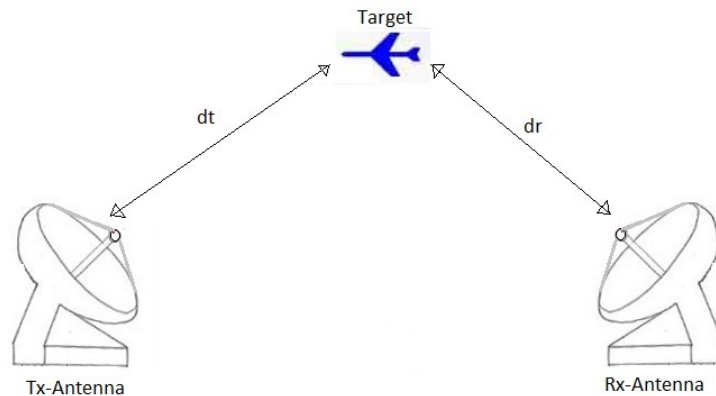


Figure 5.6: Bi-static Radar

For bi-static radar, Equations (5.1) to (5.12) were adapted by taking into account two separate antennas, distances and their efficiency. Radar range in Equation (5.13) is then re-written for bi-static radar. Radar range for bi-static radar can be seen in Equation (5.14) where subscripts r and t are referred to the receiver and the transmitter respectively.

$$R = \sqrt[4]{\frac{\sigma_m \cdot \lambda^2 \cdot R_T^4 \cdot R_R^4}{A_T \cdot A_R \cdot K_{a_t} \cdot K_{a_r}}} \quad (5.14)$$

Radar Cross-Section with bi-static radar can be re-written as in Equation (5.15) where A_e refers to projected area of the object.

$$\sigma_m = \frac{4 \cdot \pi \cdot A_e^2}{\lambda^2} \quad (5.15)$$

5.2 Radar Cross-Section Measurement Software

From the literature study, it was agreed upon to make use of the POFACETS 4.1 for the Radar Cross-Section analyses due to the licence availability issues with other commercial software but a while after a commercial licence for FEKO Hyperworks was available at the NLR. Therefore, FEKO was preferred over the POFACETS 4.1.

The FEKO is an electromagnetic simulation software developed by the Altair HyperWorks. It is based on the state-of-the-art computation methods which solves the Maxwell's equations for the simulations. It is a physics and geometry optics based software which can determine Radar Cross-Section of geometries with settable settings.

5.2.1 FEKO overview

The FEKO is an electromagnetic analyses software with a very interactive geometry specification in its CAD. Inside its CAD it can perform Boolean operation of geometries and can also create canonical structures. Multiple solution configurations can be set in its graphical user interface. The POSTFEKO is a module inside the FEKO which can be used for model validation and also helps in post processing of the results obtained through FEKO analysis. Radiation pattern can be displayed in the 3D along

⁹URL:<http://www.rfwireless-world.com/Terminology/Monostatic-radar-vs-Bistatic-radar.html> [Cited 19-Apr-2017]

with 2D(XY or polar) co-ordinates. It also does include features like multiple reflections, shadowing, edge diffraction and surface waves which are very important to this thesis study. Multiple reflections, shadowing, edge diffraction and surface waves are very important phenomena when comparing Radar Cross-Section signatures between aircraft with the conventional or the morphing high lift devices. It can also automatically update result reports in PDF, MS Word, MS PowerPoint templates. With this full version of FEKO, accuracy is not compromised. There exists no limitations on the mesh triangles, number of wires etc. in the full version of FEKO.

Although computational times depend heavily on the mesh generated but in general, computations with FEKO require high computational power. FEKO is based on the frequency domain formulation, and if the user desire to obtain time domain formulation then Fourier transforms need to be applied manually to all frequency domain data which is a downside of using FEKO.

5.3 FEKO Solvers

In this section an overview of the possible solvers available in FEKO are discussed. Based on these discussions, a solver is selected for Radar Cross-Section simulations.

Hybridization of the numerical methods is essential as these methods provide the ability to solve a broad range of electromagnetic (EM) problems. FEKO is a leading analysis software setup that provides a wide range spectrum of numerical methods and hybridization, where each method is customized to suit to a specific range of applications. Below, these methods and their ideal application industry are shortly discussed starting with the Method of Moments, which is a frequency based technique.

Method of Moments (MoM)

As mentioned above, the Method of Moments is a frequency based technique which is suitable for radiation and coupling analysis. The MoM is traditionally associated with open radiating problems involving PEC structures, lossy metals and dielectrics. The MoM is a full wave solution of the Maxwell's integral equations and has the advantage of being a "source" method due to discretization of the target. With the "field methods", boundary conditions are not set and memory requirements scale proportional to the size of the geometry and the required solution frequency. The method computes interaction between individual basis functions.

Multi-level fast multipole method (MLFMM)

This method is an alternative formulation of MoM and is suitable for electrically large, full wave analysis. Basically the advantage of using MLFMM on large models is the fact that the method does not require any change to the model. Parallel to the MoM, it also uses basis functions to model the interaction between all triangles. However, the MLFMM differs from the MoM in a way that it groups basis functions and calculates the interaction between groups of basis functions. MLFMM is an alternative technique to MoM that ensures the full wave current based solutions of electrically large structures.

Finite element method (FEM)

The FEM in FEKO is usually a hybrid FEM/MoM analysis and it is ideal for problems with several dielectrics and wave guides. In this hybrid method, the MoM is responsible for the analysis of wires and surfaces and the couplings between them whereas the FEM is responsible for the analysis of dielectric bodies. Best of both solvers is combined in it to obtain a higher efficiency meaning low memory usage. FEKO can easily evaluate if the model can be analysed using only FEM and without the need of MoM coupling which results in the low memory usage and reduced time.

Finite difference time domain (FDTD)

This is a Computational Electromagnetic (CEM) technique ideal for modeling in-homogeneous materials and simulations over a wide frequency range. This Finite difference time domain model is a time domain based and to convert the results to the frequency based domain, the Fourier transform is applied. Main usage of this kind of solver lies in the biomedical field as it is used in the cases where the materials are highly inhomogeneous. Broadband antennas can also be analysed efficiently using this type of solver as it solves the wideband problems efficiently.

Physical optics (PO)

PO and Large Element Physical Optics (LE-PO) are suitable for very large and scattering analysis. It is a current based, high frequency method. LE-PO is very similar to the PO but with the LE-PO larger elements can be analysed. Physics Optics is used to solve relatively larger structures compared to some other solvers discussed previously. FEKO again uses the hybridization technique between MoM and PO. Parts of a structure that are electrically large for the MoM are solved by the PO whereas the other with MoM which results in a better computationally efficiency.

Ray Launching geometrical optics (RL-GO)

Similar to PO, this technique is also ideal for dielectric or metal applications that has very large scattering characteristics such as Radar Cross-Section (RCS). This is applied to structures that are electrically very large. Interactions between the rays is also taken into account using the Huygens sources which models the reflection, refraction and transmission on the boundaries of the material. As the large structures are modelled with this solver, the runtime and the memory requirements are high as well. To be able to improve efficiency, FEKO allows the parallel processing using multi-core Central Processing Units.

Uniform theory of diffraction (UTD)

The UTD is formulated for modeling extremely large PEC structures. Similar to Physics Optics method this also works for very high frequencies. There exists a hybridization between the MoM and UTD. The coupling between these two enables higher accuracy of the solution and also better computational efficiency. UTD solver takes the reflections (multiple), diffractions, corner and edge diffractions, double diffractions and the creeping waves into account. UTD can only be used when the frequencies are really high e.g. radar frequencies.

5.3.1 Solver selection for RCS simulations

For the airborne, tracking and ground based radars for military applications, frequency bands between 8 and 12 GHz are used. For this very high frequency and also large scattering due to the large size of the wings, Ray Launching geometrical optics (RL-GO) was preferred for the RCS analysis of the wings. As multiple reflections are an important aspect for the Radar Cross-Section computations, RL-GO using the Huygens sources takes into account the reflection, refraction and transmission on the boundaries of the material. Other important aspects to include into Radar Cross-Section signatures are the reflections (multiple), diffractions, corner and edge diffractions, double diffractions and the creeping waves. These are modelled by the Uniform Theory of Diffraction (UTD) solver. Uniform Theory of Diffraction (UTD) must only be used at high frequencies which is the case for this study. **Therefore, a combination of two solvers, the Ray Launching geometrical optics (RL-GO) and the Uniform theory of diffraction (UTD) are used for the RCS computations.** Combination of these two solvers may result in high computational costs but will lead to results with high accuracy.

5.4 Radar Cross-Section Simulations Setup

Different geometrical and operational settings used for the RCS simulations are discussed in this section. This section have been divided into several sub-sections, each explaining the choices made and their impact on the RCS simulations.

To determine the RCS merits, four wing models in total are going to be used in the RCS simulations. 25° conventional and the 25° morphed wing and similarly a 0° conventional (no flap extension and deflection) wing and a 0° morphed(straight) wing. Modelling of these wings have been explained in Chapter 3.

A mono-static radar is responsible for both, the receiving and transmitting of the waves. Table 5.1, contains all the different wing configurations and the different locations of the radar to be used in the mono-static RCS computations.

Table 5.1: Wing configurations and radar positioning for mono-static RCS

Configuration	Location of radar
Conv. & morphed 0° TE def.	$\theta = 105^\circ$ & $\phi = 0^\circ$
Conv. & morphed 0° TE def.	$\theta = 155^\circ$ & $\phi = 0^\circ$
Conv. & morphed 0° TE def.	$\theta = 205^\circ$ & $\phi = 0^\circ$
Conv. & morphed 0° TE def.	$\theta = 255^\circ$ & $\phi = 0^\circ$
Conv. & morphed 25° TE def.	$\theta = 105^\circ$ & $\phi = 0^\circ$
Conv. & morphed 25° TE def.	$\theta = 155^\circ$ & $\phi = 0^\circ$
Conv. & morphed 25° TE def.	$\theta = 205^\circ$ & $\phi = 0^\circ$
Conv. & morphed 25° TE def.	$\theta = 255^\circ$ & $\phi = 0^\circ$

From the table, it can be noticed that 0° conventional and the morphing wings are going to be analysed for four different radar locations. For the similar radar locations, 25° wings are also going to be simulated. In total, 16 different simulations and 8 data-sets to determine the mono-static RCS merits are going to be analysed. First four rows refer to the conventional and the morphed wings with 0° deflections with their corresponding radar locations.

Spherical coordinates system is used in the software. θ and ϕ refers to the latitude and the longitudinal axis respectively. Above the wing, θ is 0°, behind the trailing edge it is 90°, towards the ground it is 180° and 270° is in front of the leading edge of the wing. ϕ is 0° at the trailing edge where wing root is located. 90° is at the tip of the right side of the wing, 180° is at the leading edge of the wing root and 270° is at the tip of the left side of the wing. Only the θ between 90 and 270 are considered, which means the location of the radar is on the ground. For the mono-static computations, ϕ is kept at 0° for all of the computations meaning that the wing roots are in line with the radar location on the ground.

The bi-static radar consists of a system where the receiver and the transmitter are separated by a certain distance. In Table 5.2 wing configurations, location of the transmitter radar and location of the receiver radar can be found in three different columns. Due to time and computational power limitations, only the 0° conventional wing and a 0° morphing (straight) wing are going to be analysed for bi-static signatures of the wings. For the transmitting radar, two different θ values of 120° and 240° are used with ϕ being 0°. For the receiver radar, θ is always kept in the opposite direction to the one used for the transmitting radar with four different ϕ angles for each θ angle.

Table 5.2: Wing configurations and Radar positioning for bi-static RCS

Configuration	Location of transmitter radar	Location of receiver radar
Conv. & morphed 0° TE def.	$\theta = 120^\circ$ & $\phi = 0^\circ$	$\theta = 240^\circ$ & $\phi = 80^\circ$
Conv. & morphed 0° TE def.	$\theta = 120^\circ$ & $\phi = 0^\circ$	$\theta = 240^\circ$ & $\phi = 160^\circ$
Conv. & morphed 0° TE def.	$\theta = 120^\circ$ & $\phi = 0^\circ$	$\theta = 240^\circ$ & $\phi = 240^\circ$
Conv. & morphed 0° TE def.	$\theta = 120^\circ$ & $\phi = 0^\circ$	$\theta = 240^\circ$ & $\phi = 320^\circ$
Conv. & morphed 0° TE def.	$\theta = 240^\circ$ & $\phi = 0^\circ$	$\theta = 120^\circ$ & $\phi = 80^\circ$
Conv. & morphed 0° TE def.	$\theta = 240^\circ$ & $\phi = 0^\circ$	$\theta = 120^\circ$ & $\phi = 160^\circ$
Conv. & morphed 0° TE def.	$\theta = 240^\circ$ & $\phi = 0^\circ$	$\theta = 120^\circ$ & $\phi = 240^\circ$
Conv. & morphed 0° TE def.	$\theta = 240^\circ$ & $\phi = 0^\circ$	$\theta = 120^\circ$ & $\phi = 320^\circ$

Similarly to mono-static computations, 16 different simulations and 8 data-sets are going to be analysed to derive the bi-static RCS merits for the conventional and the morphing wings with 0° trailing edge and flap deflections.

Before explaining the simulations setup, Figure 5.7 contains a flowchart describing the whole process leading to the simulations and ultimately to the RCS results using the FEKO.

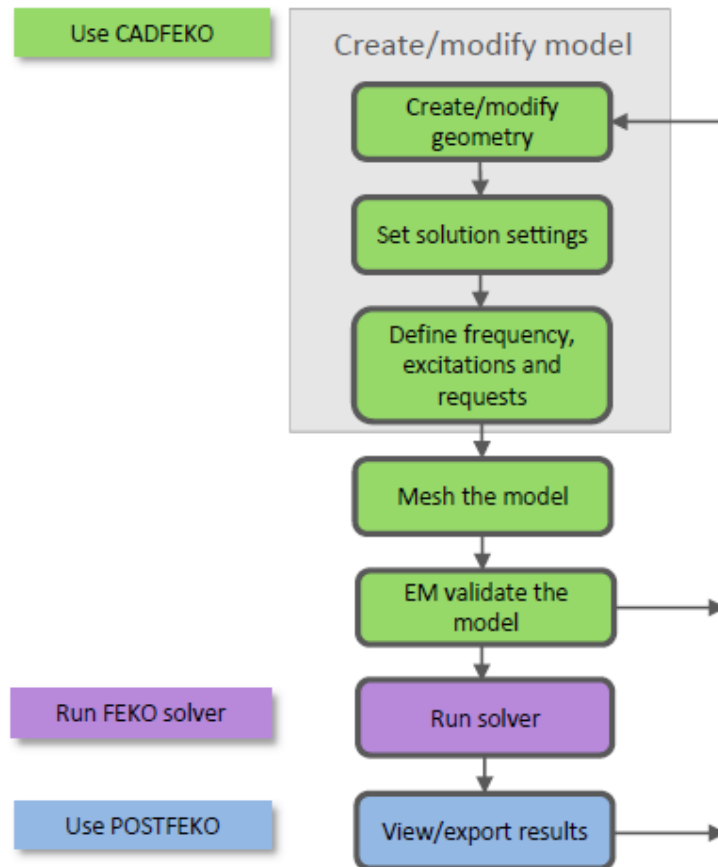


Figure 5.7: Process flow diagram for RCS simulations

Process of working with FEKO is divided into three separate categories namely CADFEKO, FEKO Solver and POSTFEKO.

In the CADFEKO, five different tasks are performed to prepare the model for the simulations. Model is first generated using CADFEKO or can be imported from different CAD programs in a certain format. Imported models require some processing before they can be used in FEKO. After geometry generation, required solvers are activated or the hybrid of solvers is setup for the simulations. After the geometry is created and the solvers have been selected, frequency is selected for the simulations. A range of frequencies can be set as well but will result in equally longer simulation times. Subsequently, excitations at which the model is being simulated are setup followed by the angles/directions at which the analysis needs to be obtained. After all these steps, the model is meshed and also the model is validated in CADFEKO, where the kernel makes sure the model is ready for the simulations without any problems. If any issues with the geometry, meshing or other settings exist, validation of the model in CADFEKO can detect it and instructs to rectify it.

After the model is prepared using CADFEKO with the geometry, meshing, requests, solution settings and the excitations, the FEKO solver is used to simulate the model for the required settings. A FEKO console with the progress is always available while the simulations are on-going. Results from the simulations are simultaneously saved in a *dat* file. If the simulations crash at some point, the results up to that point are available for the post processing.

In the POSTFEKO kernel, all the results obtained from the simulations are post-processed where it is possible to view and save contour maps, 2D plots and the processed data can also be saved which can be analysed using other software.

Simulation choices made for the RCS analyses in this thesis study are discussed in the following subsections.

5.4.1 Frequency, excitations and requests

In order to derive the potential Radar Cross-Section merits, a single frequency of **9GHz** due to time limitations is going to be used for the simulations of the wings. In an article[19], a frequency range between 7 to 11 GHz have been used for Ground to Air imaging of the Aircraft RCS scattering, therefore, a frequency of 9GHz is going to be used for the morphing and conventional wing analysis. Multiple frequencies could be used but it will eventually lead to increased simulation times. Rather than different frequencies, it was decided to use a single frequency and analyse different configurations and radars (bi-static and mono-static).

For Radar Cross-Section analyses, a plane wave excitation is used in the FEKO. Plane wave can be a single incident wave and can also be looped over multiple directions. Looping in multiple directions is helpful if several plane wave excitation locations are required for a certain target. Starting and the end angles of the directions can be set with a number of directions or just a single value of increment. Linear polarisation is used for all the analysis rather than setting a polarisation angle.

Due to the type of RCS signatures being analysed, only far-field analyses are going to be performed rather than the near-field analyses. In the ϕ direction, all 361 points from 0 to 360° are requested to observe the wing RCS signature characteristics. Other options such as the horizontal cut, vertical cut or even 3D pattern for far-field analysis can be used. In order to analyse the mono-static RCS, far-fields in the plane wave incident direction are requested whereas for the bi-static RCS, far-fields are specified separately.

An example with different plane wave excitations and far-field bi-static analyses setup is illustrated in the Figure 5.8.

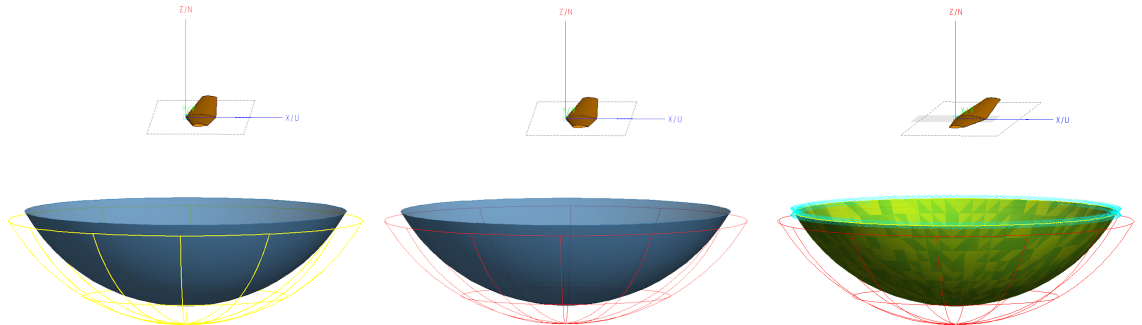


Figure 5.8: An example of different excitations and far-field bi-static analysis setup in FEKO

5.4.2 Solution settings

Solution settings for the mono-static and bi-static analyses are same. As mentioned before, a combination/hybrid of Ray Launching geometrical optics (RL-GO) and Uniform theory of diffraction (UTD) is going to be used to determine the radar signature of the wings.

In the solution settings, normal geometry and the mesh element size checking is activated. If any issues with the geometry or the meshing exists, the solver will not continue with the simulations and gives an error. To obtain as accurate RCS results as possible data storage precision was set at *double*. As the analyses are going to be performed at a high frequency of 9GHz, low frequency stabilization was not activated. To make the simulations converge faster, the PO and the MoM solutions are decoupled. Shadowing information could be stored and reused. Whenever possible, symmetry in ray-tracing is used as well.

For the Uniform theory of diffraction (UTD), maximum number of ray interactions is set to three. As mentioned before about the usefulness of UTD to these simulations, all six boxes consisting of UTD ray contributions are selected during the simulations. These include direct and reflected, double diffraction, edge and wedge diffractions, corner diffraction and cone tip diffraction. Convergence of solution is highly important for the simulations to be valid therefore, normal-to-high convergence accuracy was set before the simulations.

5.4.3 Models & mesh

All four wing models are generated using CATIA V5 and V6. Their modelling have been discussed in detail in Chapter 3. These semi-span wing models are imported into Altair-FEKO. As the wings are semi-span in size, that means the side of the root airfoil is a big flat surface. This surface is not exposed to free flow during the flight and definitely leads to an additional contribution to the RCS signatures. Even if the root side surface is left exposed in both cases, the comparison would still not be valid as root of the morphing wing is bigger than the conventional wing. As a result, the RCS signature for the morphing wing from the root side surface will be higher. Therefore, the semi-span of the wings is mirrored in FEKO to obtain the full span wing. By doing so, these undesired effects can be avoided.

After some geometrical processing to the wing models, these models are ready to be used in Altair-FEKO. After the generation of wings, their meshing is done. Triangular mesh is the only option available in FEKO to work with. The mesh in FEKO is used to define the shape of the target to be used in the simulations. Finer the mesh, better the representation of the shape of object. Mesh was selected to be as fine as the computational power allows. As the RCS scattering depends very much on the shape of the object and its sharpness, some very critical areas on the wing require finer mesh than the other parts. Therefore, the wings are decided to be meshed non-uniformly. Curved and sharp surface require more number of cells to be represented correctly during the simulations. Leading edge of the wings was meshed much more finer than the top and bottom relatively straight surfaces. In Figure 5.9, finer meshing of the leading edge of a wing compared to the top surface can be seen. Behind the leading edge, mesh size is increased gradually to maintain the mesh pattern. Triangles all over the surface of the wings need to be closed.

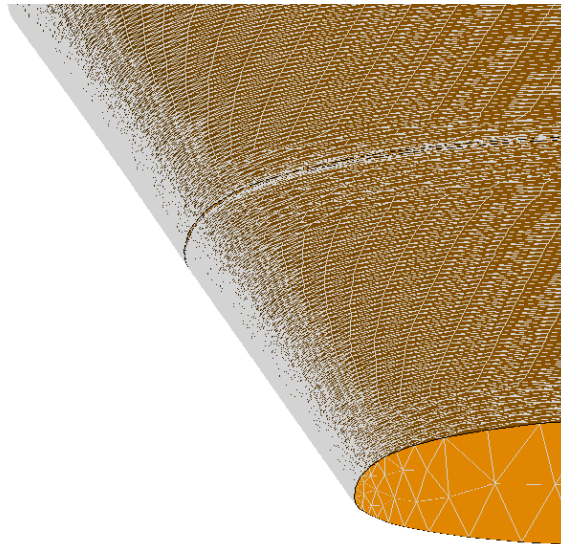


Figure 5.9: Finer mesh adaptation at the wing leading edge

Similar to the leading edge, flap track mechanisms and the sharp surfaces in the flaps are also meshed very fine compared to the other geometry. In the morphing wing, transition part and the chord at which the morphing starts are meshed finer relative to the other top and bottom wing surface. All these meshes on the wings are validated in the FEKO simulations setup kernel before the simulation could be run.

Number of triangular cells for each wing mesh can be found in Table 5.3.

Table 5.3: Mesh information for four wing types

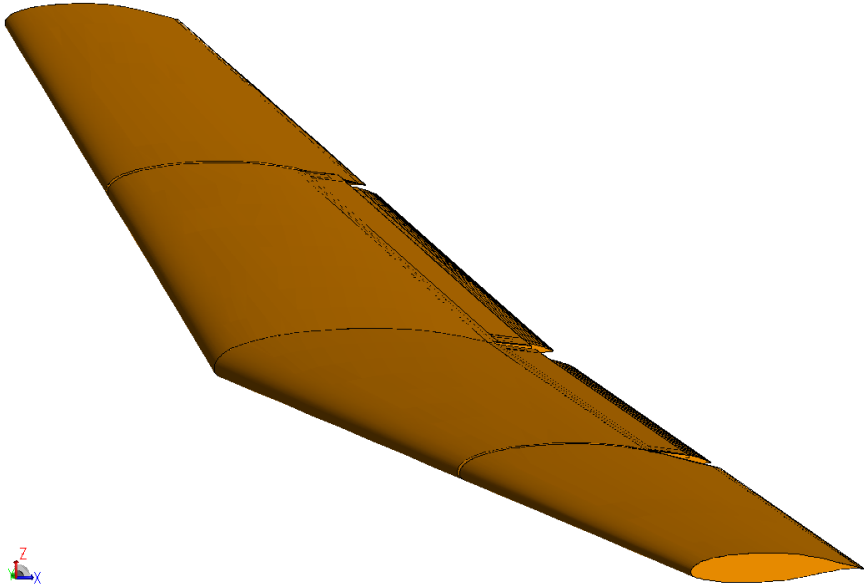
Wing type	Number of cells
Conventional wing with 25° flap deflection	269,616
Conventional wing with 0° flap deflection	200,256
Morphed wing with 25° TE deflection	139,708
Morphed wing with 0° TE deflection	131,180

From the table it can be noticed that the conventional wing with 25° flap deflection contains the highest number of mesh cells as compared to other wing geometries even though morphing wings are larger in size than the conventional wings. This is due to the flaps present in the conventional wings require additional finer meshes than the relatively 'cleaner' morphing wing surface. It can also be noticed that the conventional wing with 25° flap deflection have higher number of cells than the 0° surface, which is due to the extra finer mesh required for the leading edge of the flap. As the flap chord is extended before it can be deflected, the leading edge of the flap is also exposed to the radar therefore, it is required to be meshed much more finer.

The morphed wing with 25° trailing edge deflection consists of a transition part and a slightly curved surface at which the wing and flap morphing starts, which are not present in the straight wing(0° trailing edge deflection). This transition part and the curved surface needs to be meshed finer and that explains the difference between the mesh cells for the 25° morphed and the straight wing.

In the next four pages, all four wings modelled in CADFEKO along with their meshes can be found. These wings with their meshes are ready to be used in the simulations along with the other geometrical and operational settings discussed in previous two sub-sections.

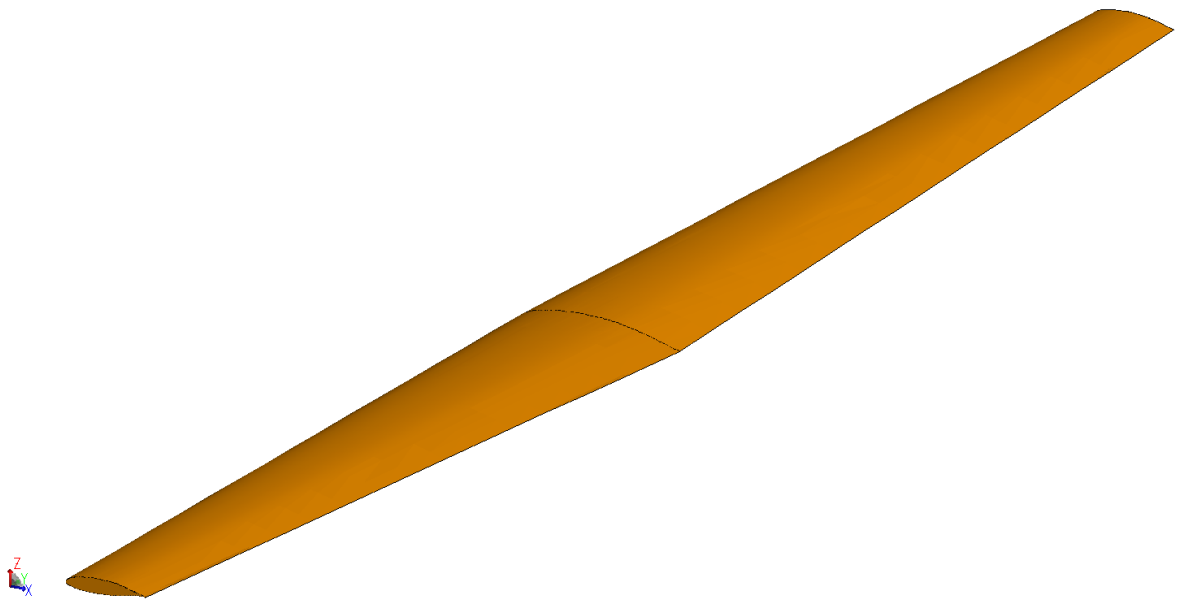
Conventional wing with 0° flap deflection



Mesh-Conventional wing with 0° flap deflection



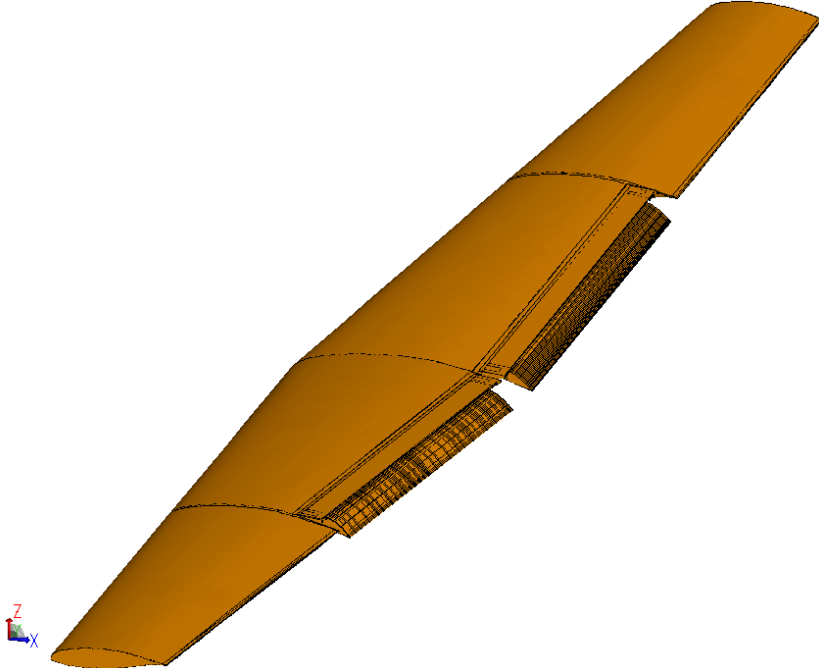
Morphed wing with 0° trailing edge deflection



Mesh-Morphed wing with 0° trailing edge deflection



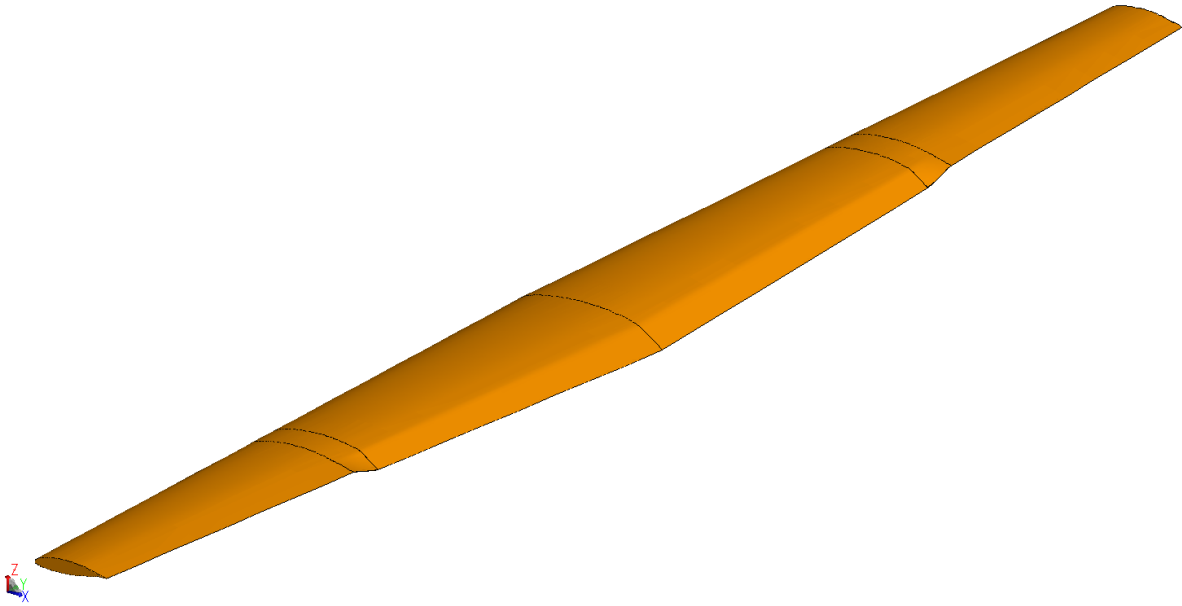
Conventional wing with 25° flap deflection



Mesh-Conventional wing with 25° flap deflection



Morphed wing with 25° trailing edge deflection



Mesh-Morphed wing with 25° trailing edge deflection



5.4.4 Simulations

During the simulations, very complex computations are performed by Hyperworks FEKO which leads to simulations being very computationally expensive. An electromagnetic plane wave targets the wings

from the set radar location which illuminates the surface of the wing. This illumination of the surface leads to the dispersion of the wave energy in different directions depending on the shape, size and orientation of the target. As the measurements are done at the frequency of 9GHz and at far-field conditions, the scattering of energy from the components is independent from each other and smaller than the overall target object. The scattered energy back to the radar from each component is different and smaller than the target itself but summation of these could be similar to the target. In each particular direction, multiple scattering can occur therefore, it was selected to compute the total Radar Cross-Section or total scattered field for each angle.

5.5 Results from RCS Simulations

This section is devoted to the results obtained from the Radar Cross-Section simulations using Hyperworks FEKO. The results are divided into two different categories: mono-static and bi-static radar signature of the wings. In total eight different mono-static RCS simulations (four with 25° conventional and morphing wing and 4 with 0° conventional and morphing wing) and 8 different (with 0° conventional and morphing wing) bi-static RCS simulations were performed. In order to observe the potential Radar Cross-Section merits, radar signatures of both wings are plotted together.

5.5.1 Monostatic RCS

From the mono-static Radar Cross-Section computations for the 0° conventional and the morphing wing, only two are presented here and the other two can be found in the Appendix C.1 of the report. Figure 5.10 and 5.11 contains mono-static radar signature of the wings with trailing edge deflections of 0° with the radar located at $\theta = 155^\circ$ & $\phi = 0^\circ$.

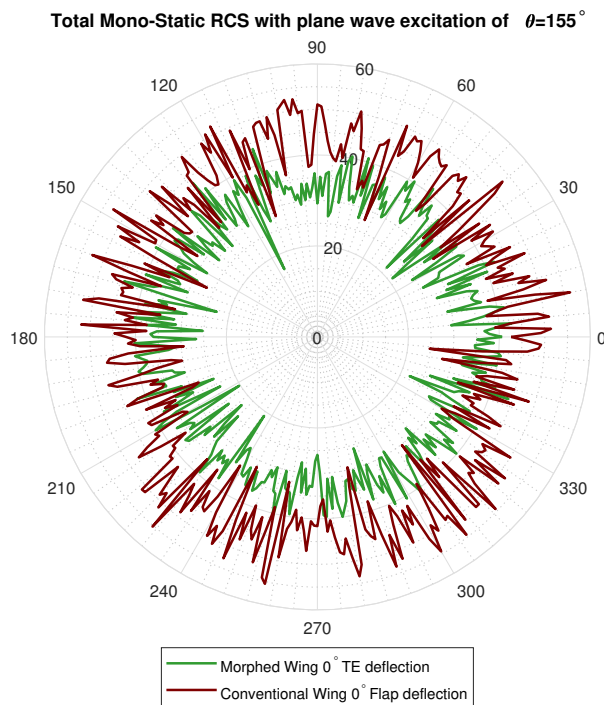


Figure 5.10: Mono-static RCS signature of the wings with TE deflection of 0° with radar location at $\theta = 155^\circ$ & $\phi = 0^\circ$

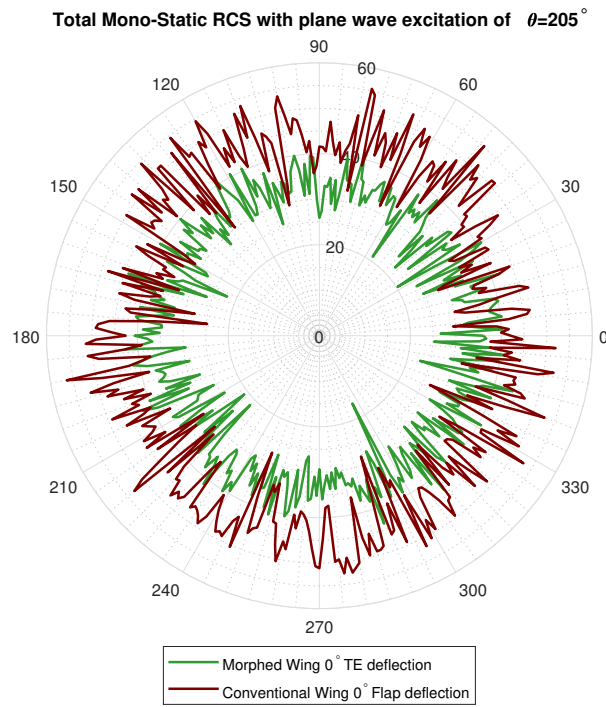


Figure 5.11: Mono-static RCS signature of the wings with TE deflection of 0° with radar location at $\theta=205^\circ$ & $\phi=0^\circ$

Similarly to the mono-static radar signature of the wings with trailing edge deflections of 0° , only two radar signature comparisons between the wings with 25° trailing edge deflections are presented here and the other two can be found in the Appendix C.1 of the report. Similar radar locations are analysed for the 25° case as well. Figure 5.12 and 5.13 contains mono-static radar signature of the wings with trailing edge deflections of 25° with the radar located at $\theta=155^\circ$ & $\phi=0^\circ$.

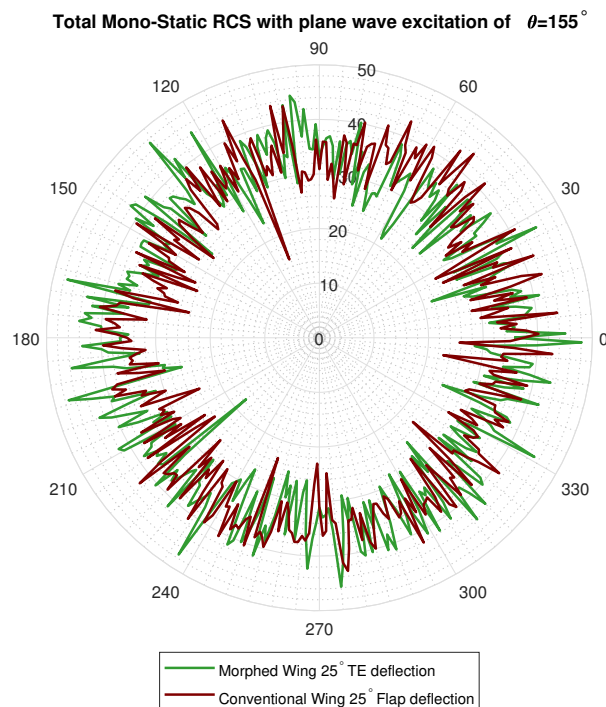


Figure 5.12: Mono-static RCS signature of the wings with a TE deflection of 25° and the radar location at $\theta=155^\circ$ & $\phi=0^\circ$

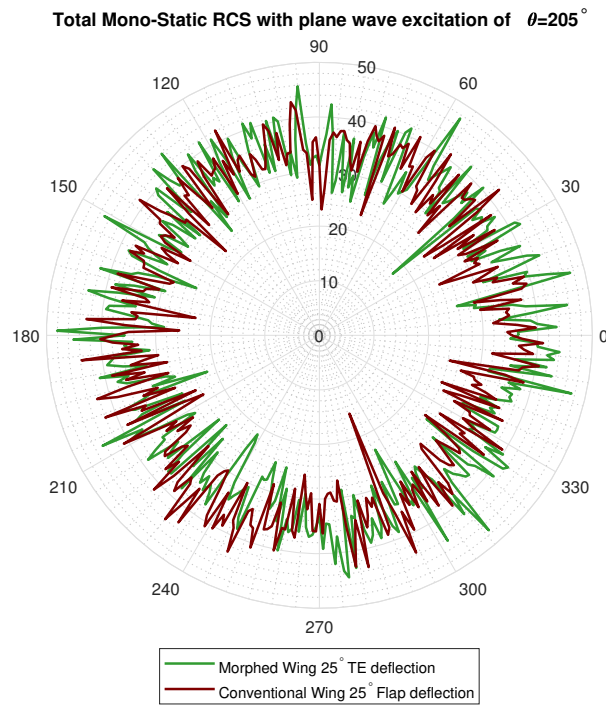


Figure 5.13: Mono-static RCS signature of the wings with a TE deflection of 25° and the radar location at $\theta=205^\circ$ & $\phi=0^\circ$

5.5.2 Bi-static RCS

Radar signature of the wings resulting from the different transmitter and receiver locations of the radar are categorized as bi-static RCS. In total eight different datasets to derive the conventional and morphing wing Radar Cross-Section merits were determined. Out of eight, four of them are presented here and the other four similarly to the mono-static case can be found in the Appendix C.2 of the report. Only the conventional and the morphing wing with 0° trailing edge deflections are analysed for the bi-static RCS as discussed before.

Figures 5.14 and 5.15 contain the comparison of the bi-static radar signature between the conventional and morphing wing at the transmitting radar location at $\theta=120^\circ$ & $\phi=0^\circ$ with the receiver radar location at $\theta=240^\circ$ & $\phi=160^\circ$ and the transmitting radar location at $\theta=120^\circ$ & $\phi=0^\circ$ with the receiving radar location at $\theta=240^\circ$ & $\phi=320^\circ$ respectively.

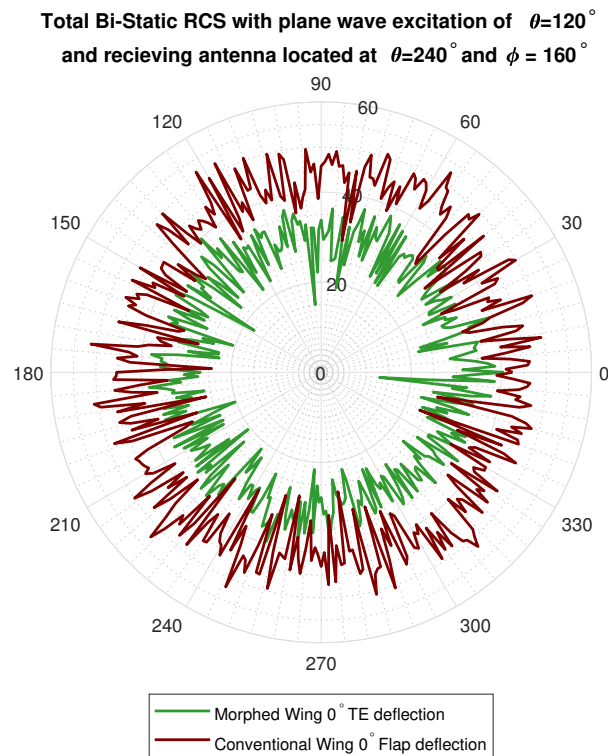


Figure 5.14: Bi-static RCS signatures of the wings with the transmitting radar located at $\theta= 120^\circ$ & $\phi =0^\circ$ and the receiver radar located at $\theta= 240^\circ$ & $\phi= 160^\circ$

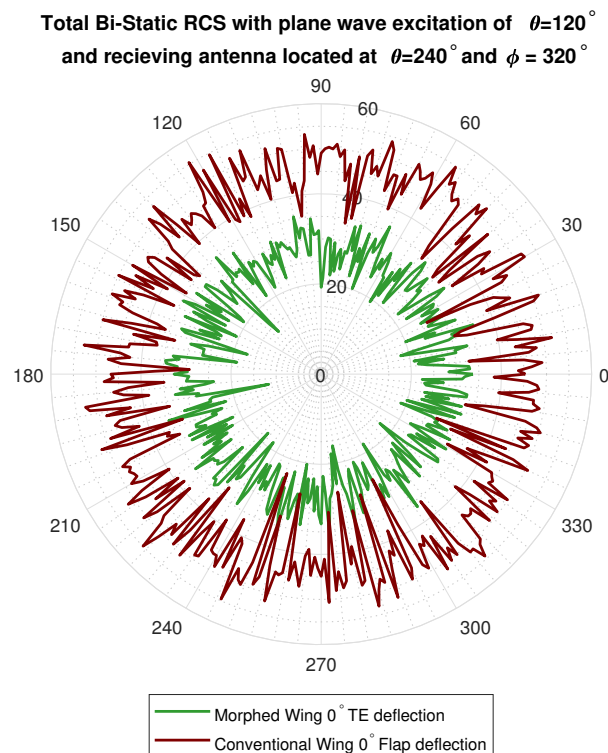


Figure 5.15: Bi-static RCS signature of the wings with the transmitting radar located at $\theta= 120^\circ$ & $\phi =0^\circ$ and the receiver radar located at $\theta= 240^\circ$ & $\phi= 320^\circ$

In the following two figures, θ location of the transmitter and the receiver have been inter-changed

with the ϕ location of the receiving radar is kept similar to the previous two bi-static radar analysis. Figures 5.16 and 5.17 contain the comparison of the bi-static radar signature between the conventional and morphing wing at the transmitting radar location at $\theta = 240^\circ$ & $\phi = 0^\circ$ with the receiver radar location at $\theta = 120^\circ$ & $\phi = 160^\circ$ and transmitting radar location at $\theta = 240^\circ$ & $\phi = 0^\circ$ with receiving radar location at $\theta = 120^\circ$ & $\phi = 320^\circ$ respectively.

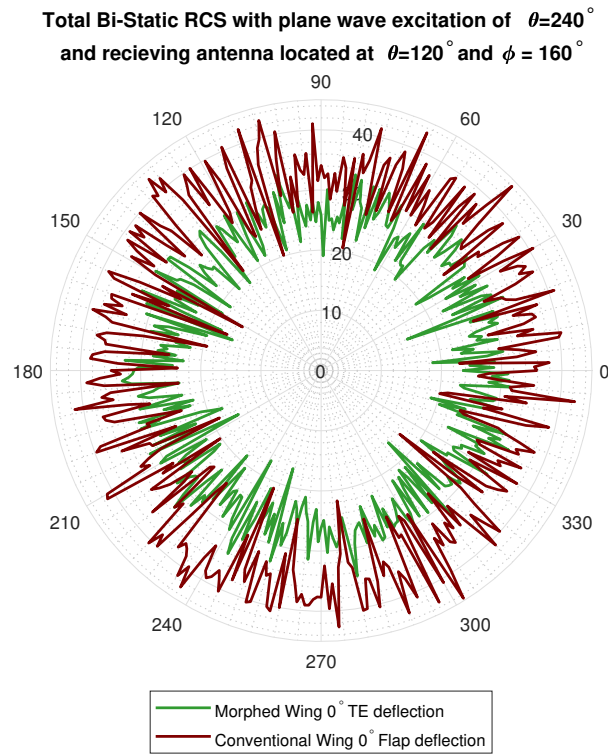


Figure 5.16: Bi-static RCS signature of the wings with the transmitting radar located at $\theta = 240^\circ$ & $\phi = 0^\circ$ and the receiver radar located at $\theta = 120^\circ$ & $\phi = 160^\circ$

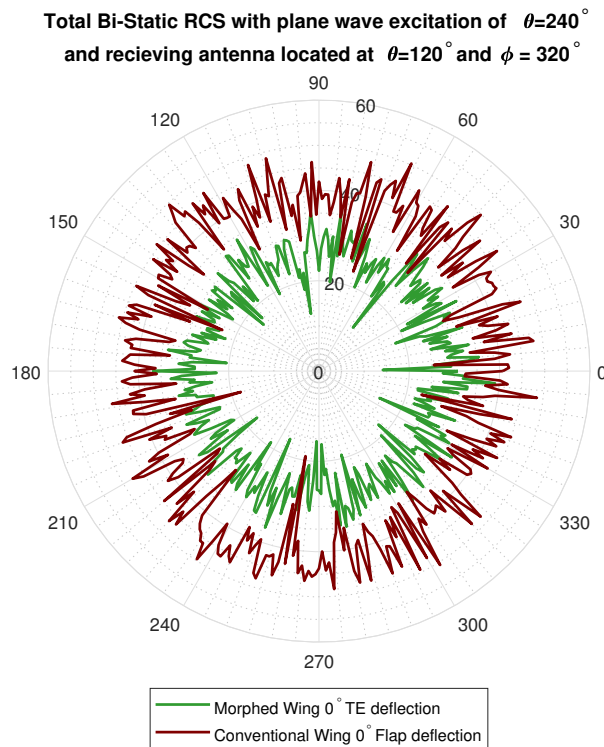


Figure 5.17: Bi-static RCS signature of the wings with the transmitting radar located at $\theta= 240^\circ$ & $\phi =0^\circ$ and the receiver radar located at $\theta= 120^\circ$ & $\phi= 320^\circ$

5.6 Discussion of results

After the wings are illuminated by the electromagnetic wave propagating from the transmitting radar from an angle, wave energy is dispersed in different directions. Some of this dispersed energy is reflected to the receiver radar. In the mono-static RCS case, the same radar performs both these operations. On the other hand, two different radars located at two different locations perform this operation for bi-static radar. As there are number of scattering sources/components present on an aircraft wing therefore, the Radar Cross-Section pattern adopts quick scintillation around the aspect angle. This rapid scintillation is due to the interference between the components that scatters this energy as they are in and out of phase against each other. This explains the pattern of radar signature in the plots.

Data has been chosen to be presented in the polar coordinates rather than rectangular presentation due to the illustration advantages that comes with the polar representation. It provides a physical feel to the scattered data of the target and the dynamic variations can also be emphasized in the radar signature in the polar plot.

Gaps that are associated with the conventional hinged high-lift devices and the control surfaces are a source of increased radar reflection. For the 0° trailing edge deflections, the RCS signature benefits for the morphing wings are observed at all angles despite the larger size of the morphing wing. Larger the size of the target, higher is the radar signature. Increase in the RCS signature of the conventional wing is due to the flap gaps, extra flap mechanisms and the flap side-edges. Scattering of the wave and reflection back to the radar because of these flap characteristics resulted in this reduced low-observability of the conventional wing with flap settings. On the other hand for the straight wing i.e. morphing wing with 0° trailing edge deflection, the transmitted radar signals are reflected away from the receiving radar leading to the improvement in the low-observability of the wing. For the 25° trailing edge deflections, morphing wings generate higher overall radar signature compared to the conventional wing. Low observability advantages of the morphing wing with 25° trailing edge deflection over the conventional wing diminishes when the trailing edge of the morphing wing is deflected downwards. Reflections between the surface and the creeping waves in addition to the larger size of the wing relative to the conventional

wing results in this decrease in the low observability of the morphing wing. Similar characteristics for the 0° trailing edge deflections were observed for the bi-static analysis as the mono-static 0° trailing edge deflection wings. Reduction in the radar signature is observed at almost all aspect angles for the receiving and the transmitting radars. Radar Cross-Section response to the corners, gaps and corner reflectors is very sensitive to the bi-static angle. Therefore, higher radar signature differences at some bi-static angles are observed between the wings.

In order to quantify the Radar Cross-Section merits, summation of the radar signature in all 360 aspect angles provide a measure of comparing the radar signature between both wings. Tables containing comparison between the RCS signature of the conventional and the morphing wings for all the simulations performed are shown here. Table 5.4 contains the mono-static RCS signature for the wings with 0° trailing edge and flap deflections followed by Table 5.5 where the mono-static RCS signatures for the wings with 25° trailing edge and flap deflections are summarised. Finally, in Table 5.6, bi-static RCS signatures for the wings with 0° trailing edge and flap deflections are shown.

Table 5.4: Mono-static Radar Cross-Section comparison of the wings with a TE deflection of 0°

Wing	Summation of Total RCS 0 to 360° [dBsm]			
	$\theta = 105^\circ$ & $\phi = 0^\circ$	$\theta = 155^\circ$ & $\phi = 0^\circ$	$\theta = 205^\circ$ & $\phi = 0^\circ$	$\theta = 255^\circ$ & $\phi = 0^\circ$
Conventional	63.44	71.99	68.02	63.41
Morphing	53.47	61.47	57.44	53.46

Table 5.5: Mono-static Radar Cross-Section comparison of the wings with a TE deflection of 25°

Wing	Summation of Total RCS 0 to 360° [dBsm]			
	$\theta = 105^\circ$ & $\phi = 0^\circ$	$\theta = 155^\circ$ & $\phi = 0^\circ$	$\theta = 205^\circ$ & $\phi = 0^\circ$	$\theta = 255^\circ$ & $\phi = 0^\circ$
Conventional	53.07	61.68	61.67	53.01
Morphing	54.93	63.22	63.38	54.81

Table 5.6: Bi-Static Radar Cross-Section comparison of the wings with a TE deflection of 0° by summation of total RCS from 0 to 360°

Location of Radars	Total RCS 0 to 360° [dBsm] Conventional wing	Total RCS 0 to 360° [dBsm] Morphing wing
T= $\theta = 120^\circ$ & $\phi = 0^\circ$ R= $\theta = 240^\circ$ & $\phi = 80^\circ$	66.81	53.92
T= $\theta = 120^\circ$ & $\phi = 0^\circ$ R= $\theta = 240^\circ$ & $\phi = 160^\circ$	70.37	58.23
T= $\theta = 120^\circ$ & $\phi = 0^\circ$ R= $\theta = 240^\circ$ & $\phi = 240^\circ$	60.05	55.77
T= $\theta = 120^\circ$ & $\phi = 0^\circ$ R= $\theta = 240^\circ$ & $\phi = 320^\circ$	72.88	54.95
T= $\theta = 240^\circ$ & $\phi = 0^\circ$ R= $\theta = 120^\circ$ & $\phi = 80^\circ$	60.88	54.32
T= $\theta = 240^\circ$ & $\phi = 0^\circ$ R= $\theta = 120^\circ$ & $\phi = 160^\circ$	61.95	53.53
T= $\theta = 240^\circ$ & $\phi = 0^\circ$ R= $\theta = 120^\circ$ & $\phi = 240^\circ$	70.22	53.94
T= $\theta = 240^\circ$ & $\phi = 0^\circ$ R= $\theta = 120^\circ$ & $\phi = 320^\circ$	68.00	54.84

5.7 Validation of Hyperworks-FEKO

Due to the confidential nature of the subject, virtually no Radar Cross-Section experimental measurements for any aerial vehicle for different configurations and aspect angles are available in open literature.

RCS measurements of the operational military aerial vehicles are not shared by the defense research institutes. In order to validate the radar signatures of the MQ-9 obtained from the simulations, validation of the the Radar Cross-Section measurement software (FEKO) is done instead of validating the radar signatures of the wings. Similar geometrical and operational configurations are validated and modelled in FEKO of an already available experimental data irrespective of the geometry.

5.7.1 Experimental data

Experimental measurements from the weapons division at the NAVAL Air Warfare Center are used to validate the software [2]. These measurements were performed indoors in a Bi-static Anechoic Chamber (BAC) with the chamber dimensions of $150m \times 150m \times 60m$. Indoor measurements poses several advantages as compared to the measurements in an open space. It provides extra security, equipment can be operated in all weather conditions and also reduces the costs of an experiment. Walls of the chamber are covered with a radar absorbing material but the performance of the material is limited, which means some of the waves are reflected off the walls[21]. Effect of these performance limitations on the results is discussed during the comparisons.

The radio frequency system for the transmission consists of a LINTEK 5000 radar system and a single feed antenna with the frequency range from 180MHz to 2GHz. Mono-static and bi-static measurements can be performed using this LINTEK 5000 High-speed radar system.[32]

Bi-static measurements were performed on an aluminum cylinder with a diameter of 4.5 inches with length of 13 feet at the VHF band frequency of 150MHz. Far-field behaviours of the cylinder radar signatures were recorded using collimators reflectors. In the near-fields close to the scattering source, the radiation values are dominated by the non-radiative behaviours present in the electromagnetic fields whereas in the far-fields actual electromagnetic radiations dominate. With an increase in distance from the source, magnitude of far-field radiation increases. These are inversrly proportional to eachother.

Only the plots of the measured data with RCS values on the Y-axis and the aspect angles on the X-angles were available instead of the raw data. Therefore, data points from the plots were extracted using *webplotdigitizer*¹⁰ which are then used in comparison with the simulated data obtained using FEKO. Process of obtaining these data points and getting to the 2D values can be seen in Figure 5.18.

¹⁰URL:<https://automeris.io/WebPlotDigitizer/> [Cited 19-Apr-2018]

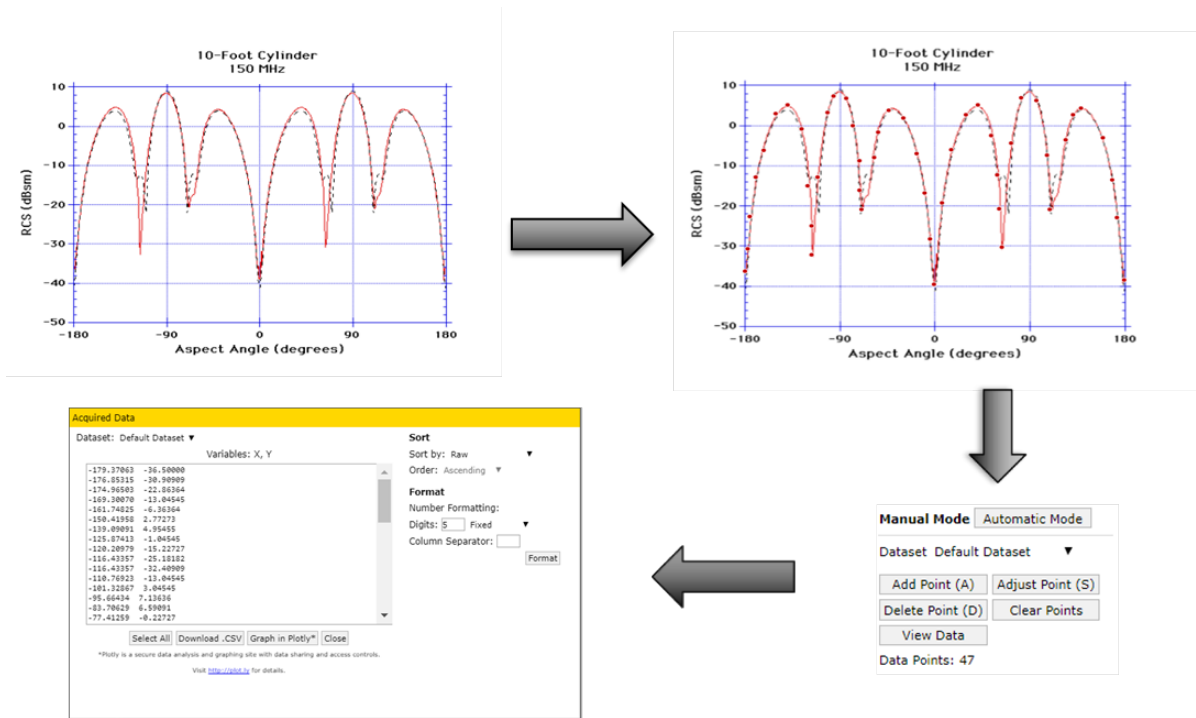


Figure 5.18: Experimental data extraction for validation

Values obtained from these measurements will be compared to the simulation values from FEKO in the next part of the chapter.

5.7.2 FEKO measurements

Comparisons of the measured RCS and the simulated RCS for the cylinder with a diameter of 4.5 inches and a length of 13 feet is discussed in this part of the chapter.

FEKO measurements were performed on an aluminum cylinder with same geometrical and operational settings. No approximations are used in the electromagnetic formulation with Method of Moments solver for the analysis. This solution can be assumed to be exact depending on the fineness of mesh.

Frequency of the simulations is set to 150MHz which is same as the one used in measurements and lies in the VHF band. Due to the low frequency measurements, Method of Moments was used where it uses full wave solution of the Maxwell's integral equations and as a result leads to relatively accurate results. Locations of the transmitter and the receiver antenna are set at similar locations as the measurements and the far-field analysis were requested during the setting up of the simulations. Cylinder was meshed as fine as the computational power allows. Increments in the aspect angles were not made too small due to very high computational power requirements. Increments in the aspect angles were chosen such that a valid picture of the scattering behaviour can be analysed.

In Figures 5.19 and 5.20, comparison of the Radar Cross-Section signatures from the NAVAIR measurements and the FEKO simulations can be found. Figure 5.19 contains the comparison in the polar plot where Radar Cross-Section in dBsm is in the radial direction as a function of the aspect angles.

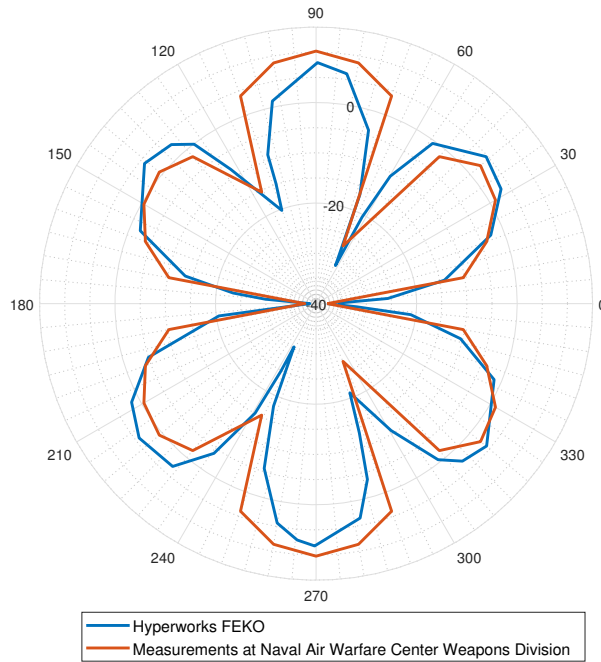


Figure 5.19: Comparison of RCS signatures of experimental and simulated analysis in a polar plot

In Figure 5.20, a 2D plot of the Radar Cross-Section comparison can be found. Aspect angles are represented on the X-axis and the RCS in dBsm is on the Y-axis.

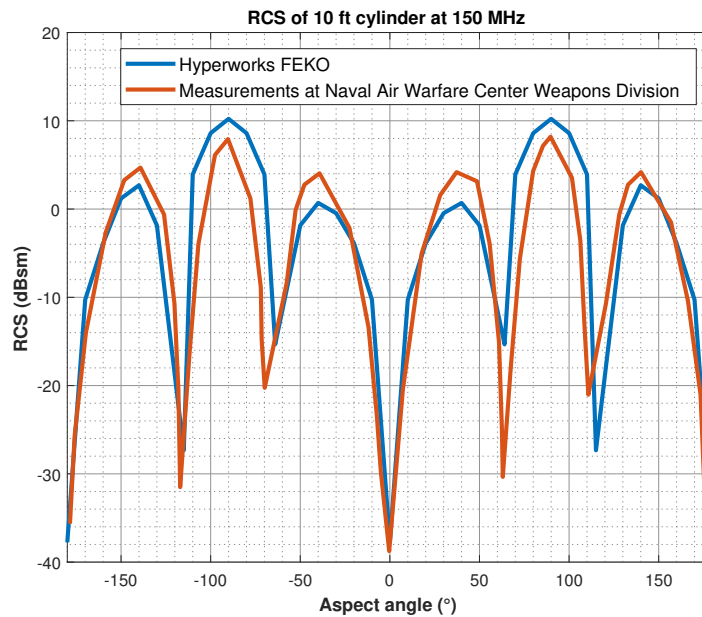


Figure 5.20: Comparison of RCS signatures of experimental and simulated analysis in a 2D plot

From the figures, it can be noticed that the Radar Cross-Section responses of cylinder for the measurements and the simulations provides with an indication of decent accuracy. For the simulations in FEKO, high degree of symmetry between 0° to -180° and 0° to 180° exists which was expected as well. For the experiments, slight discrepancies in the symmetry are visualized, which as mentioned before are due to the radar absorption limitations of the chamber wall. This leads to some of the waves to reflect off the walls. Overall, the data between the measurements and the simulations shows an excellent correlation. Similar RCS patterns for simulations and the measurements even at low Radar Cross-Section values

show a decent agreement in the obtained radar signatures.

From this validation it can be concluded that the results obtained for the wings are within decent accuracy. Therefore, it can be concluded that the Radar Cross-Section for the wings obtained and their comparisons are valid.

6. Conclusions & Recommendations

This Chapter is devoted to the conclusions that are drawn from the thesis work and the recommendations that can be suggested for the further research and future work. Conclusions of this thesis work are discussed in Section 6.1. Subsequently, in Section 6.2 recommendations for the future work are mentioned.

6.1 Conclusions

In order to make sure the prospect of flap morphing on the MQ-9 Reaper, an extensive literature review on the state-of-the-art shape-changing structures in the aerospace domain was carried out. Main technologies and design methodologies that are used to facilitate the wing morphing were discussed. Most of the work has only been carried on the Unmanned Aerial Vehicles and military vehicles due to many roadblocks that FAA puts on new design technologies in civil aviation such that it takes years or even decades to approve before it can be operational. With the available technologies and recent research on SMART materials it can be concluded that it is more than possible to implement the flap morphing on a MQ-9 Reaper.

Lack of previous research on the subject of morphing wings with respect to the Aero-Acoustic noise and Radar Cross-Section motivated the work presented in this thesis report. In Chapter 1, the following research question was stated:

What are the potential Radar Cross-Section and Aero-Acoustic noise merits of a GA-ASI MQ-9 Reaper by applying flap morphing?

This study carried out the Radar Cross-Section and Aero-Acoustic noise analysis on the MQ-9 Reaper and derived potential merits. In order to obtain the potential merits, existing wing of the MQ-9 was also modelled along with the morphing wing based on the low-fidelity aerodynamic analysis and the textbook approach. To be able to satisfy or match the performance requirements of the conventional wing and flap configuration, surface area of the morphing wing was increased by 27%.

For the first time, fully 3D printed scaled wings were successfully noise tested at the NLR's AV-LAB. For the morphing wing, 35, 50 and 70m/s speeds were tested but for the conventional wing only the 35 and 50 m/s were possible. At 70 m/s, flap of conventional wing started to deform slightly due to increased loads.

From the Sound Pressure Level spectra, it was noticed that after the frequency of 1100Hz, the conventional wing generates higher noise peaks compared to the morphing wing. Between 1100 Hz and 1300Hz difference in the noise peaks is higher for the 35m/s plots whereas for the 50m/s these peaks dampens out but the difference in the sound pressure levels still exists.

It was found out that the morphing wings generated lower Overall Sound Pressure Level than the conventional wings for all operational settings and configurations. For the 35m/s data, minimum difference between the morphing and the conventional wing was observed at the angle of attack of 0° with difference in the Overall Sound Pressure Level being 4.7% whereas on the other hand maximum difference of 38% was observed at the maximum tested angle of attack of 12°. For the 50m/s data, minimum difference of 20.66% was observed at the lowest angle of attack and the maximum difference was obtained at the angle of attack of 6° where the difference in the noise generation by the morphing and the conventional wing in terms of Overall Sound Pressure Level is about 32%.

In order to approximate the hearing system of humans, A-weighting to the Overall Sound Pressure Level of the wings was applied. Similarly, noise generation by the conventional wing was higher than the morphing wing for all operational and configuration settings. Additionally, in order to visualise the

noise sources on the wings for different operational and configuration settings, beamforming maps were generated for 16 different one-third octave band center frequencies.

Werner Dobrzynski's noise approximation technique together with Karl-Stephane Rossignol's flap-side noise approximation technique was used to predict the noise generation of both wings. From the predicted data, it was found out that the minimum percentage difference in the Overall Sound Pressure Level generation is 36% at the lowest analysed angle of attack of 0° and highest at the angle of attack of 12° where the difference mounts to 45%. Comparing these percentage values to the percentage reduction from the experimental results it can be noticed that predicted data resulted in 10-15% additional reduction for the morphing wing. Overall, the noise prediction technique provides a quick with decent level accuracy to approximate the noise of the wings during initial design of the aircraft.

Radar Cross-Section analysis were successfully performed using HyperWorks FEKO for different operational and configurational settings. Due to the number of scattering sources/components present on the wings, Radar Cross-Section pattern adopts quick scintillation around the aspect angle. This rapid scintillation is due to the interference between the components that scatters this energy as they are in and out of phase against each other. For the mono-static Radar Cross-Section analysis with trailing edge and flap deflection of 0° , a significant reduction in the radar signature is observed for the morphing wing despite its larger size compared to the conventional wing. This higher RCS signature of the conventional wing is due to the extra flap gaps, extra flap mechanisms and the flap side-edges which are not present for the morphing wing. For the mono-static Radar signature with 0° deflection, after summation of total RCS in all 360 directions, a maximum and a minimum decrease of 10.52dBsm and 9.95dBsm was observed.

Low observability advantages of the morphing wing with 25° trailing edge deflection over the conventional wing diminishes when the trailing edge of the morphing wing is deflected downwards. Reflections between the surface and creeping waves in addition to the larger size of the wing relative to the conventional wing results in this decrease in the low observability of the wings. For the 25° trailing edge and flap deflections, an increase in radar signature between 1.54 and 2 dBsm was noticed.

Similar characteristics like the mono-static 0° trailing edge deflections were observed for the bi-static analyses. Reduction in the radar signature was observed for all locations of the receiving and the transmitting radars. Radar Cross-Section response to the corners, gaps and corner reflectors is very sensitive to the bi-static angle. Therefore, the higher radar signature differences at some bi-static angles are observed between both wings.

Lastly, bi-static Radar Cross-Section analysis were also performed on 0° wings where the decrease in the overall radar signature between 4 and 18 dBsm was observed.

6.2 Recommendations

Finally, some recommendations for the future work can be suggested.

- High-fidelity CFD analysis and windtunnel tests can be used in designing the morphing wing with high accuracy.
- Identical surface roughness of the 3D printed wings should be ensured.
- Angle of attack correction should be applied to accurately determine the flow angle of attack.
- Acoustic measurements on the 3D wings can be performed to take into account the additional 3D effects and their consequences on the noise generation.
- Range of the angles of attack can be increased upto the stall limit during the experiments to analyse the noise behaviour at high angles of attack.
- Radar Cross-Section merits can be analysed for a range of radar frequencies rather than a single frequency.

-
- With high computational resources, meshes could be made more finer to obtain Radar Cross-Section merits with higher accuracy.
 - Increased number of radar locations(mono-static and bi-static) and target orientations can be analysed to re-visit conclusions on the Radar Cross-Section merits.
 - Radar Cross-Section merits can be analysed with increased number of ray interactions.
 - Instead of simulating only wings, full MQ-9 Reaper with fuselage, tail surfaces etc. should be analysed with both types of wings to take into account the reflections and ray interactions between different components.

A. History of Morphing Wing Aircraft

In Figure A.1, a timeline is given showing the implementation of morphing wing technologies (along with the type of morphing) on fixed wing aerial vehicles. Most of these aerial vehicles belong in the Military domain.






















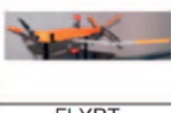













1903	1931	1931	1932	1937	1947	1951
						
Wright Flyer <i>Twist</i>	Pterodactyl IV <i>Sweep</i>	MAK-10 <i>Span</i>	IS-1 <i>Bi-to monoplane</i>	LIG-7 <i>Chord</i>	MAK-123 <i>Span</i>	X 5 <i>Sweep</i>
1952	1964	1964	1966	1967	1967	1969
						
XF10F <i>Sweep</i>	F 111 <i>Sweep</i>	XB 70 <i>Span bending</i>	Su 17 IG <i>Sweep</i>	MIG 23 <i>Sweep</i>	SU 24 <i>Sweep</i>	Tu 22 M <i>Sweep</i>
1970	1972	1974	1974	1979	1981	1985
						
F 14 <i>Sweep</i>	FS 29 <i>Span</i>	B 1 <i>Sweep</i>	Tornado <i>Sweep</i>	AD 1 <i>Obliquing</i>	Tu 160 <i>Sweep</i>	AFTI/F 111 <i>M.A.W.</i>
1993	1994	2001	2002	2003	2004	2005
						
FLYRT <i>Span</i>	MOTHRA <i>Camber</i>	AAL <i>Pitch</i>	F/A 18 <i>A.A.W.</i>	Virginia Tech <i>Span</i>	Univ. of Florida <i>Twist</i>	Univ. of Florida <i>Gull</i>
2006	2006	2007	2007	2007	2008	2010
						
MFX 1 <i>Sweep & Span</i>	Univ. of Florida <i>Sweep</i>	Virginia Tech <i>Camber</i>	Univ. of Florida <i>Folding</i>	MFX 2 <i>Sweep & span</i>	Delft Univ. <i>Sweep</i>	Virginia tech <i>Camber</i>

Figure A.1: Timeline of the implementation of morphing wing technologies [39]

B. Future of Morphing Wings in Military Domain

In this Chapter, notional future of the shape-changing/morphing wing structures in the military domain is presented. All the information in this section is gathered from the open literature and assembled into a table. This information can be found in Table B.1.

Table B.1: Future of Shape-Changing Structures in Military domain (*Note: EM-Electromagnetic & CoG-Center of Gravity*)

Vehicle Capability	Morphing feature	Challenges	Feature varied	Properties	Solutions
Multipoint aerodynamic operation	Structure/CoG	Structural changes according weight & power requirements	Mechanical	Variable Young's Modulus	Adaptable polymer/composite
Adaptive EM signature	Real/virtual appearance of vehicle	Hide in background environment/appear as another vehicle without altering performance	Mechanical/Multispectral	Variable conductivity	Adaptive polymer with structural properties
Antenna	Steerable	Reflectivity must be dynamically reconfigurable	EM	Variable dielectric with structural health	Adaptive polymer with structural properties
Optical stealth	Color/Texture/Reflectivity	Environmental issues	EM environment	Variable reflectivity/Color bandwidth	Variable dielectric/conductive polymers
Restore control surfaces after battle damage	Grow new control surfaces	Grow new structure /replace damaged portions	Mechanical loads	Variable Young's Modulus	Adaptive polymers

C. Additional Radar Cross-Section Results

In this Appendix, mono-static and bi-static radar signature of the conventional and the morphing wings in addition to the ones discussed in Chapter 5 are presented.

C.1 Mono-static RCS

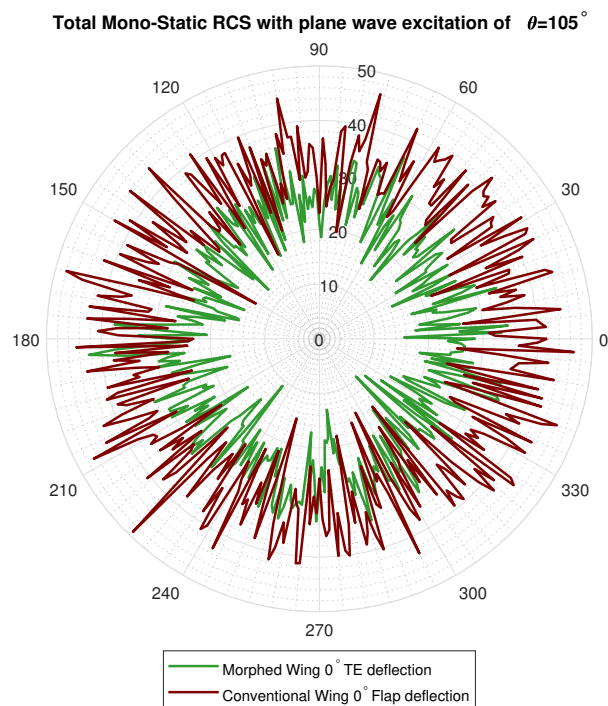


Figure C.1: Mono-static RCS signature of the wings with a TE deflection of 0° and the radar location at $\theta=105^\circ$ & $\phi=0^\circ$

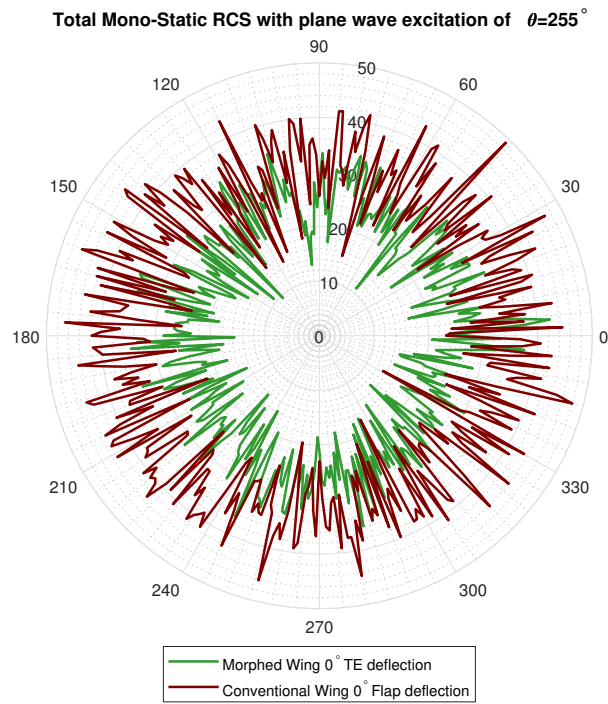


Figure C.2: Mono-static RCS signature of the wings with a TE deflection of 0° and the radar location at $\theta=255^\circ$ & $\phi=0^\circ$

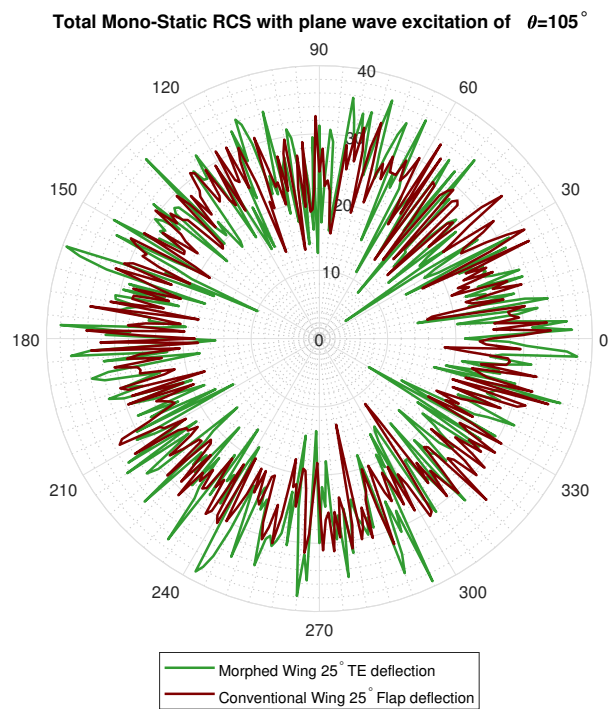


Figure C.3: Mono-static RCS signature of the wings with a TE deflection of 25° and the radar location at $\theta=105^\circ$ & $\phi=0^\circ$

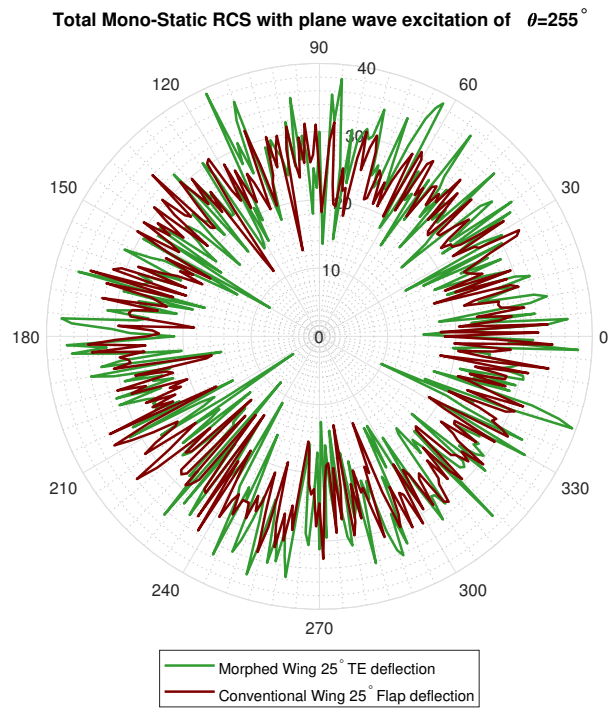


Figure C.4: Mono-static RCS signature of the wings with a TE deflection of 25° and the radar location at $\theta = 255^\circ$ & $\phi = 0^\circ$

C.2 Bi-Static RCS

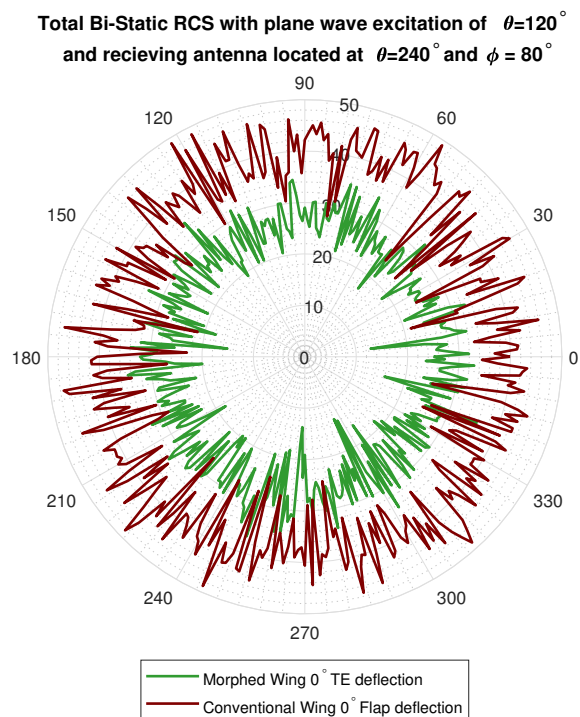


Figure C.5: Bi-static RCS signature with the transmitting radar located at $\theta = 120^\circ$ & $\phi = 0^\circ$ and the receiver radar located at $\theta = 240^\circ$ & $\phi = 80^\circ$

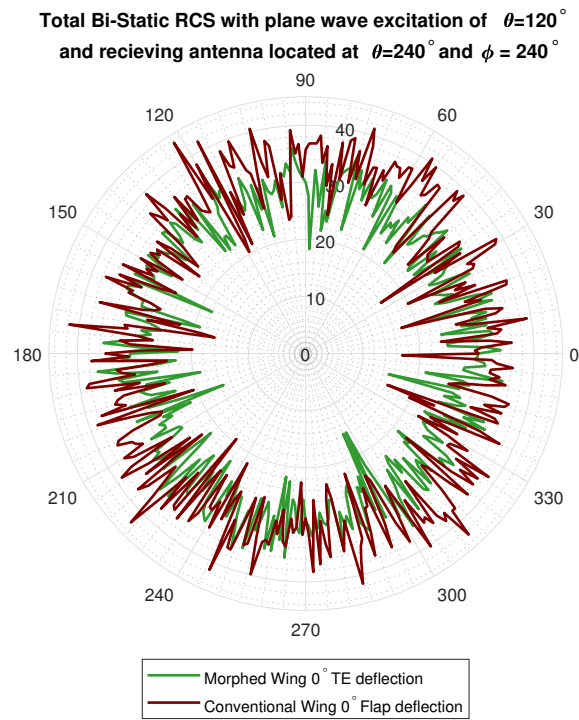


Figure C.6: Bi-static RCS signature with the transmitting radar located at $\theta=120^\circ$ & $\phi=0^\circ$ and the receiver radar located at $\theta=240^\circ$ & $\phi=240^\circ$

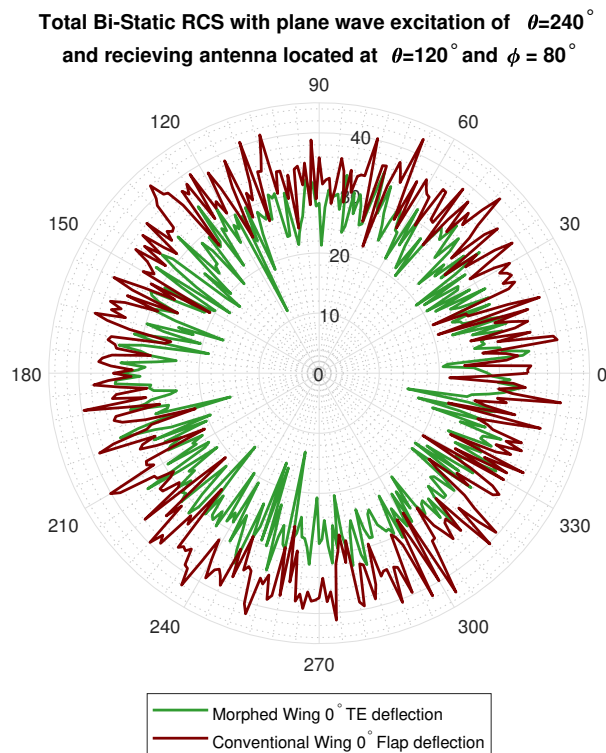


Figure C.7: Bi-static RCS signature with the transmitting radar located at $\theta=240^\circ$ & $\phi=0^\circ$ and the receiver radar located at $\theta=120^\circ$ & $\phi=80^\circ$

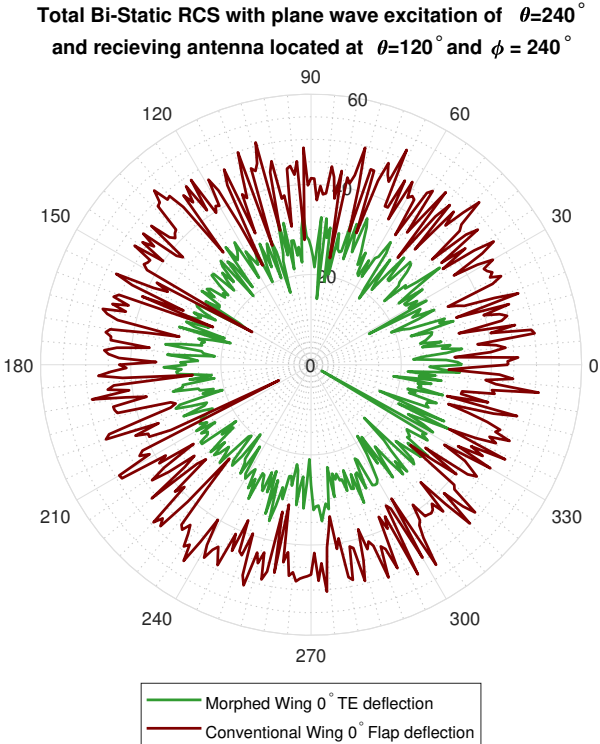


Figure C.8: Bi-static RCS signature with the transmitting radar located at $\theta= 240^\circ$ & $\phi =0^\circ$ and the receiver radar located at $\theta= 120^\circ$ & $\phi= 240^\circ$

D. Additional Aero-Acoustic Noise Results

Sound Pressure Level spectras and the beamform maps of the experimental data in addition to configurations and operational settings discussed in Section 4.2 are presented in this Appendix.

D.1 SPL spectras

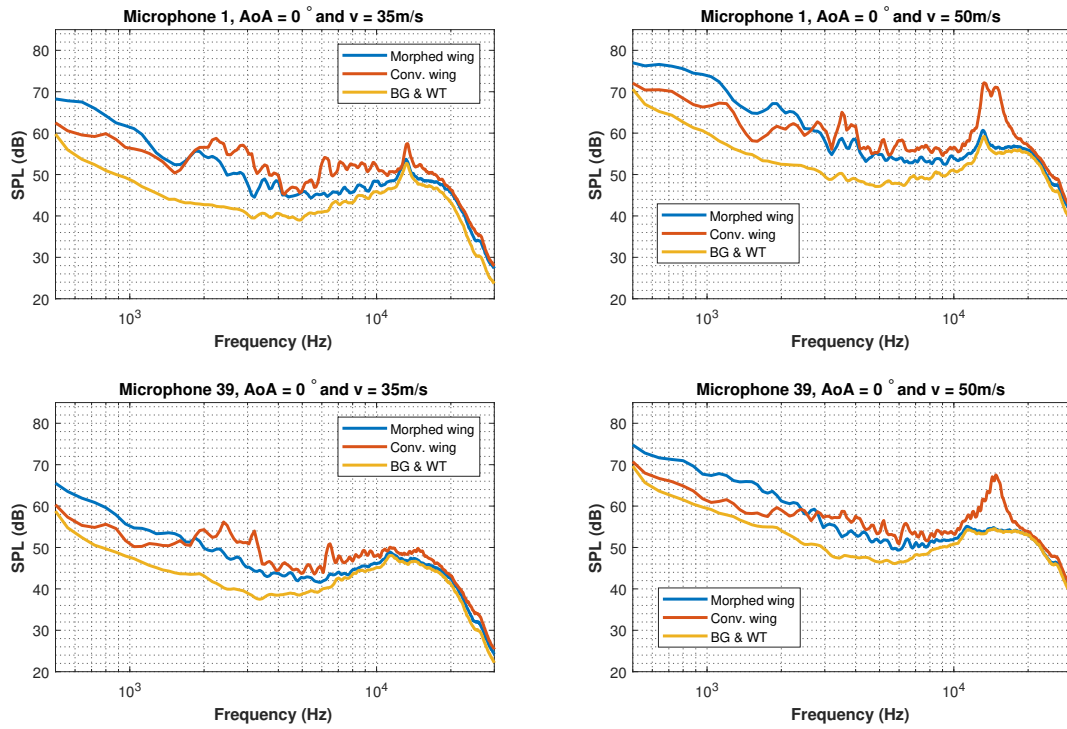


Figure D.1: SPL spectra for the morphed and the conventional wing along the background noise with an angle of attack of 0° for two different speeds and microphones

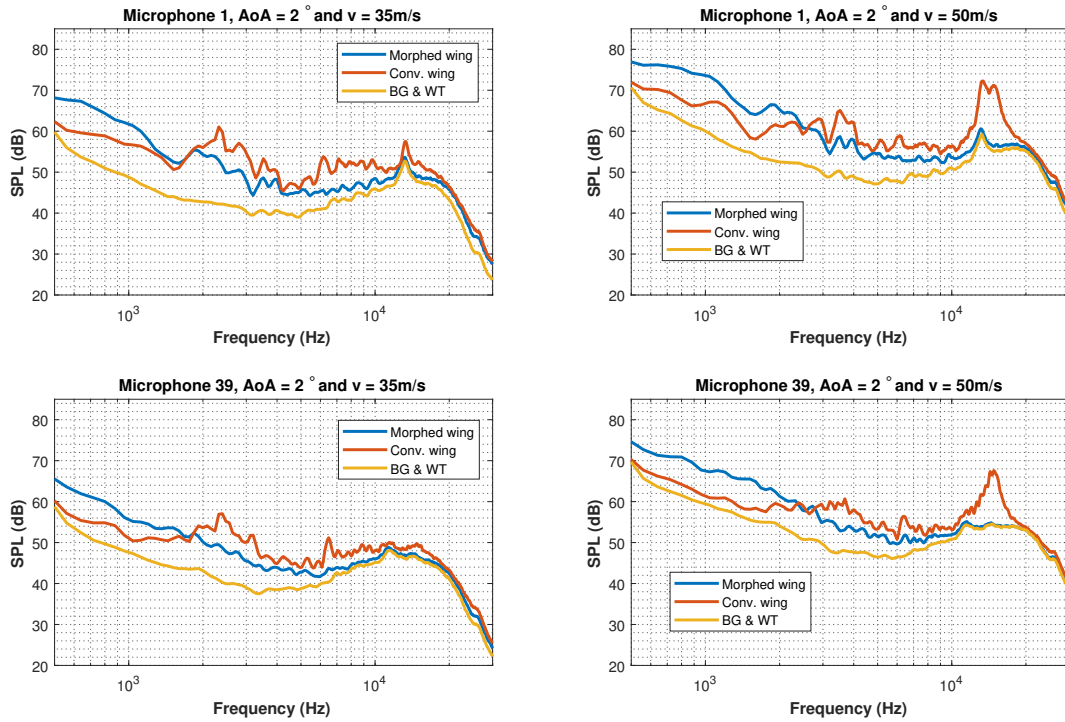


Figure D.2: SPL spectra for the morphed and the conventional wing along the background noise with an angle of attack of 2° for two different speeds and microphones

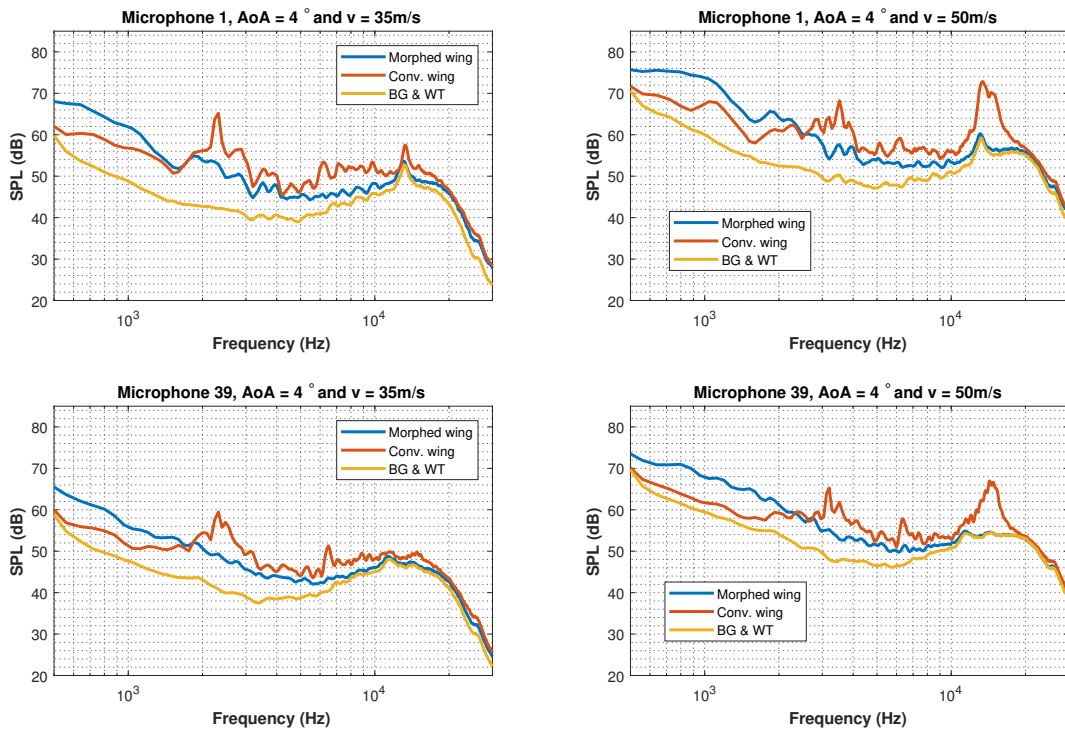


Figure D.3: SPL spectra for the morphed and the conventional wing along the background noise with an angle of attack of 4° for two different speeds and microphones

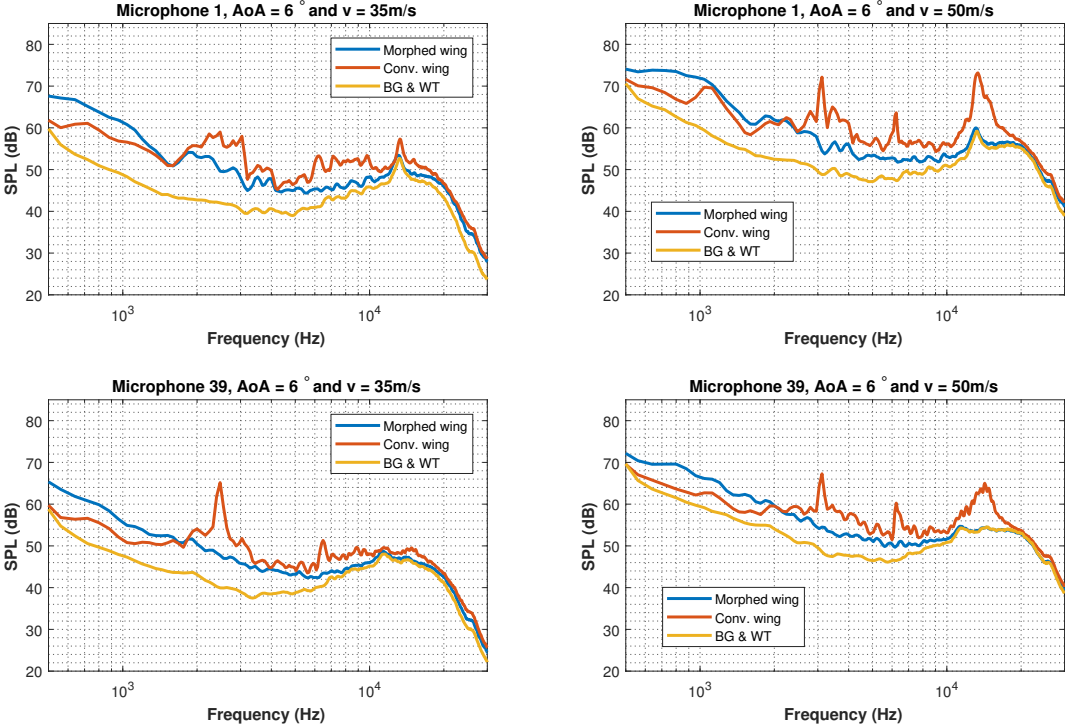


Figure D.4: SPL spectra for the morphed and the conventional wing along the background noise with an angle of attack of 6° for two different speeds and microphones

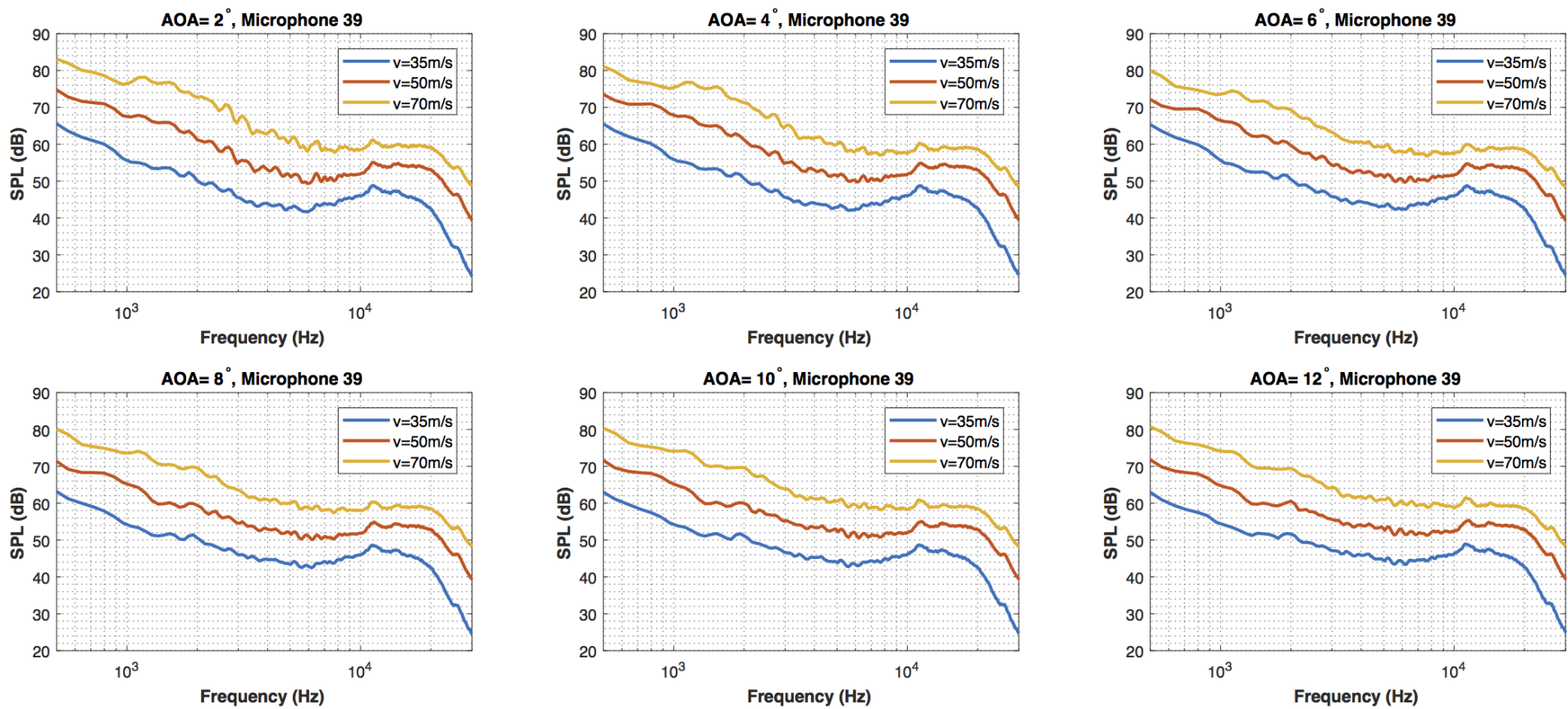


Figure D.5: SPL spectra for each AOA starting with 2° with microphone 39 and the speed of 35, 50 and 70 m/s

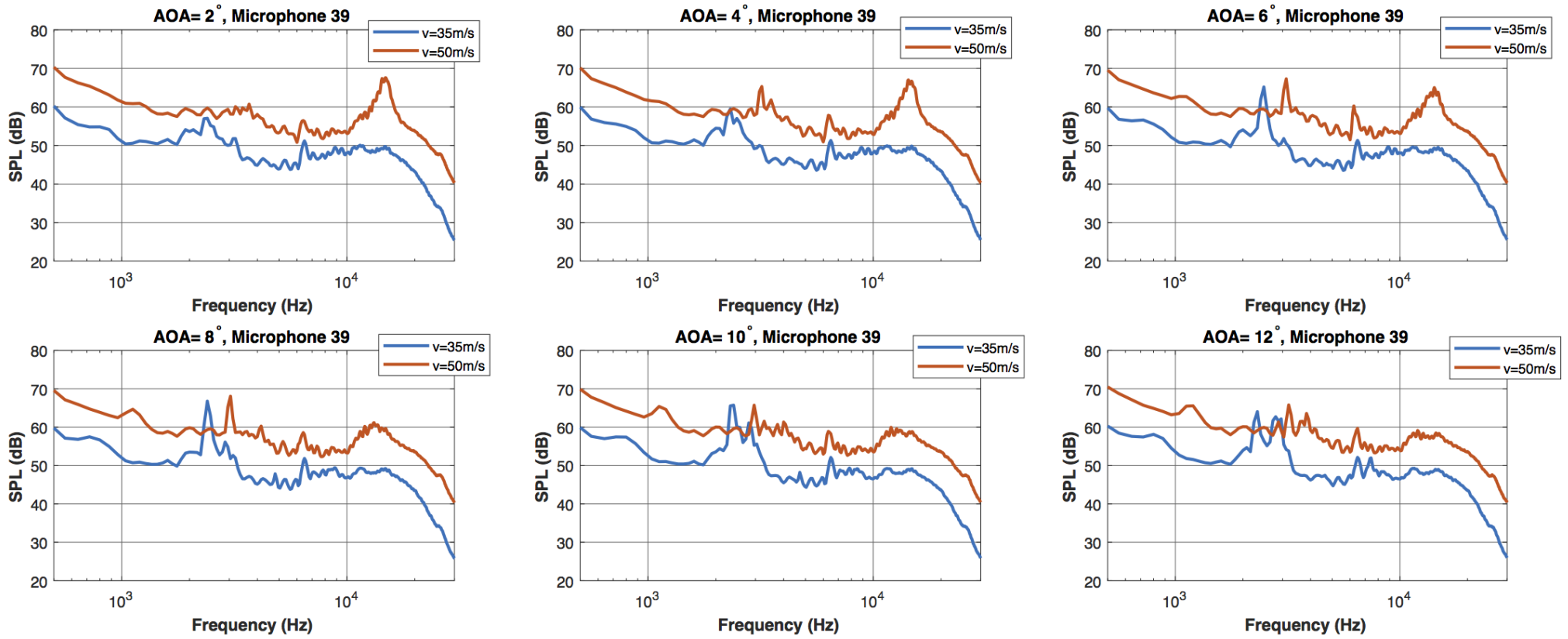


Figure D.6: SPL spectras for each AOA starting with 2° with microphone 39 and the speed of 35 and 50 m/s

D.2 Beamforming results

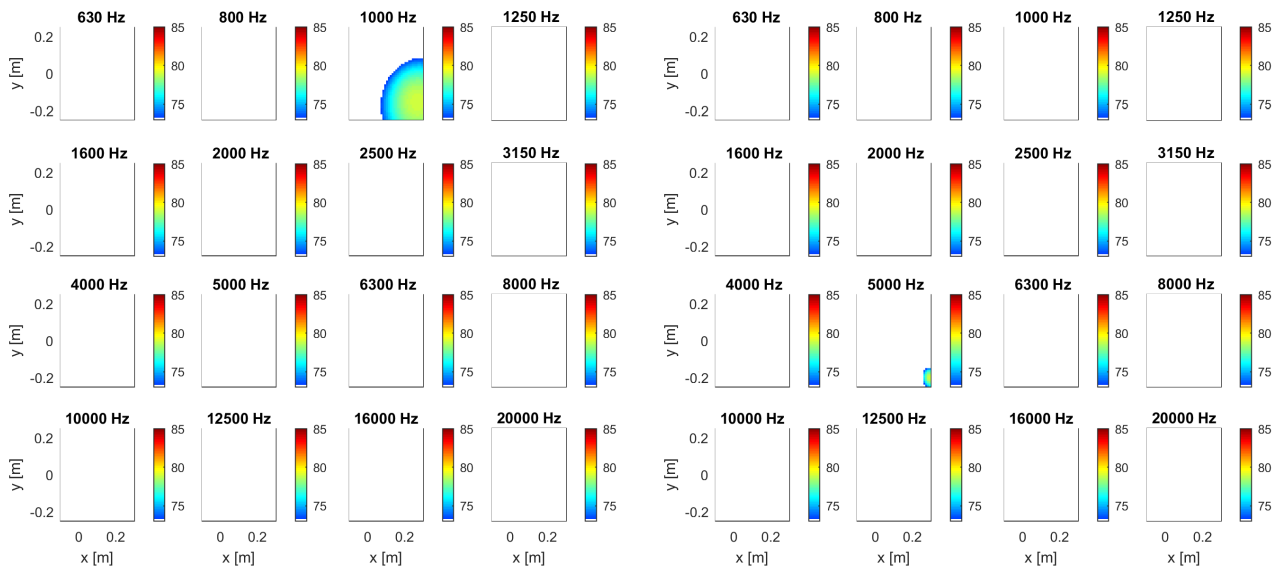


Figure D.7: Beam maps of speaker with two 1000Hz(left) and 5000Hz(right) and speaker position at $(0.3, -0.21, 0)$

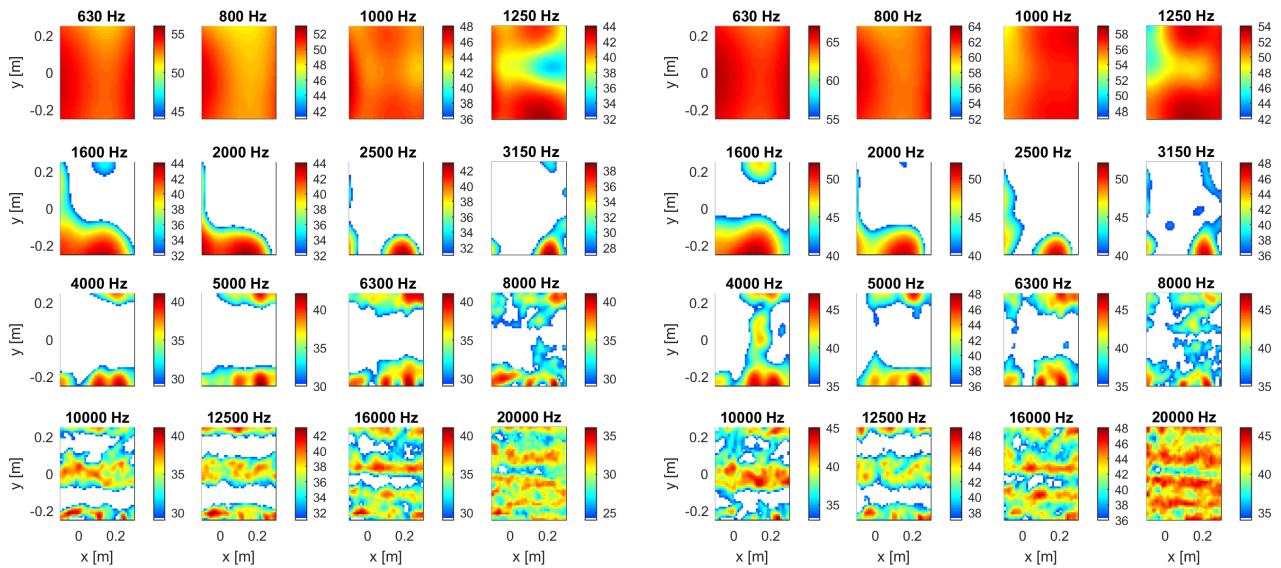


Figure D.8: Beam maps for the windtunnel and the background noise with 35 m/s(left) and 50 m/s(right) speeds

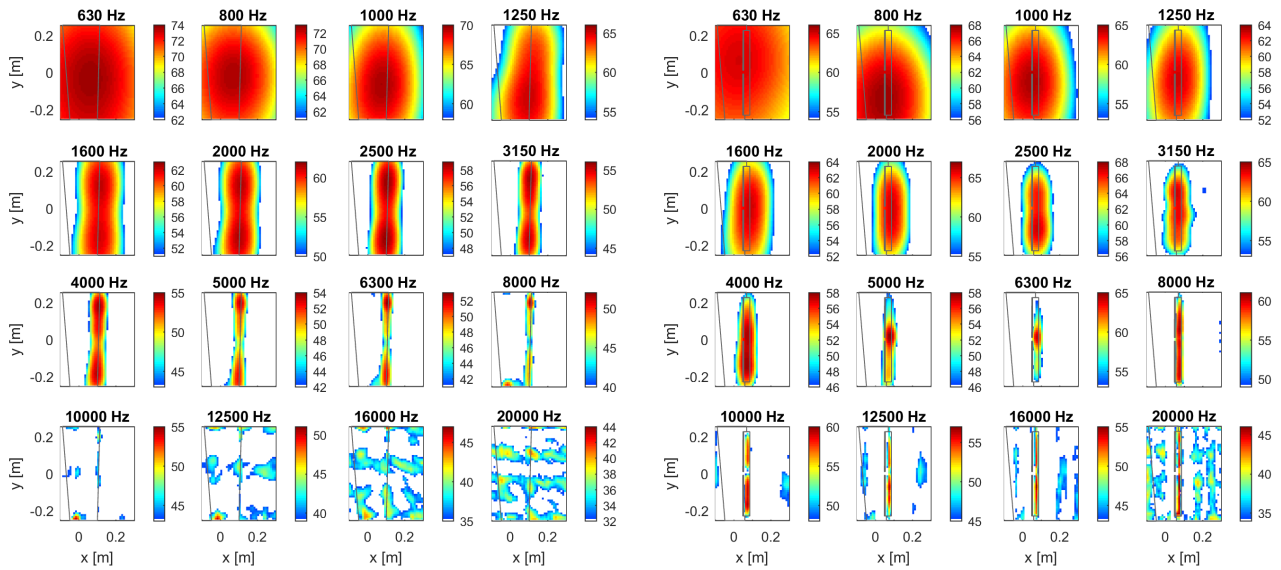


Figure D.9: Beam maps for the conventional(right) and the morphed(left) wing with 0° angle of attack and 35m/s

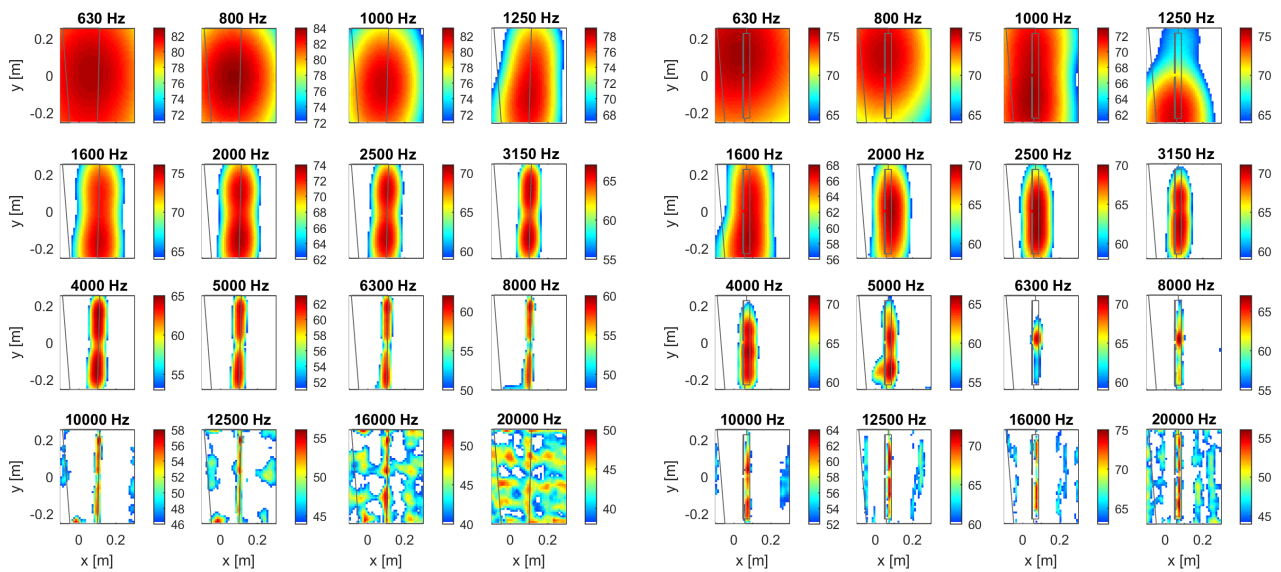


Figure D.10: Beam maps for the conventional(right) and the morphed(left) wing with 0° angle of attack and 50m/s

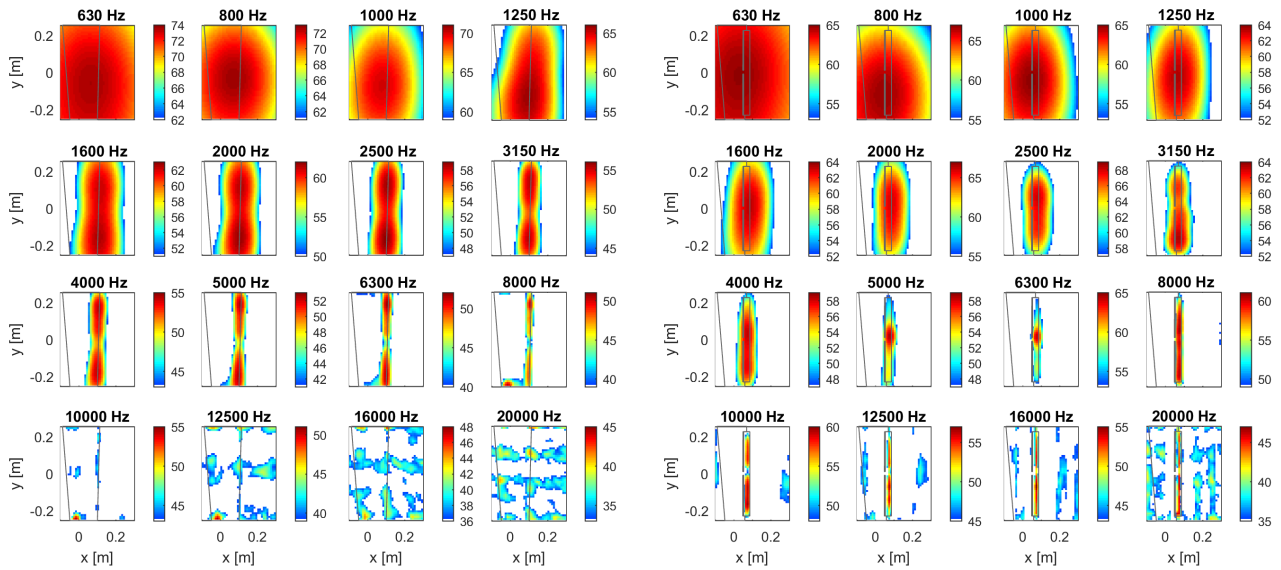


Figure D.11: Beam maps for the conventional(right) and the morphed(left) wing with 2° angle of attack and 35m/s

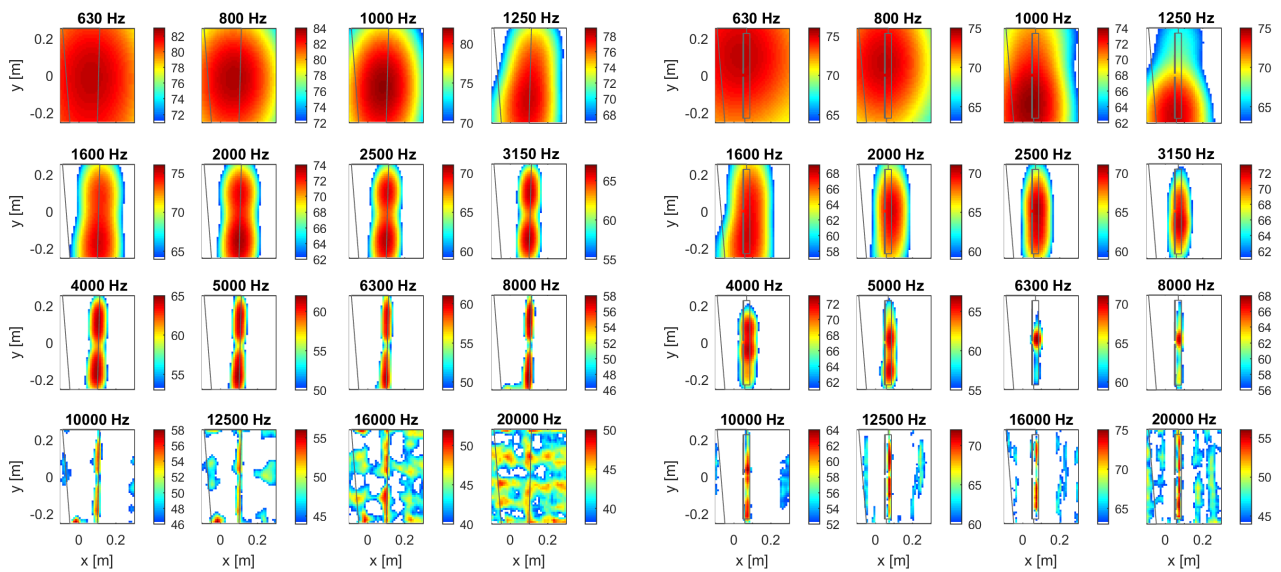


Figure D.12: Beam maps for the conventional(right) and the morphed(left) wing with 2° angle of attack and 50m/s

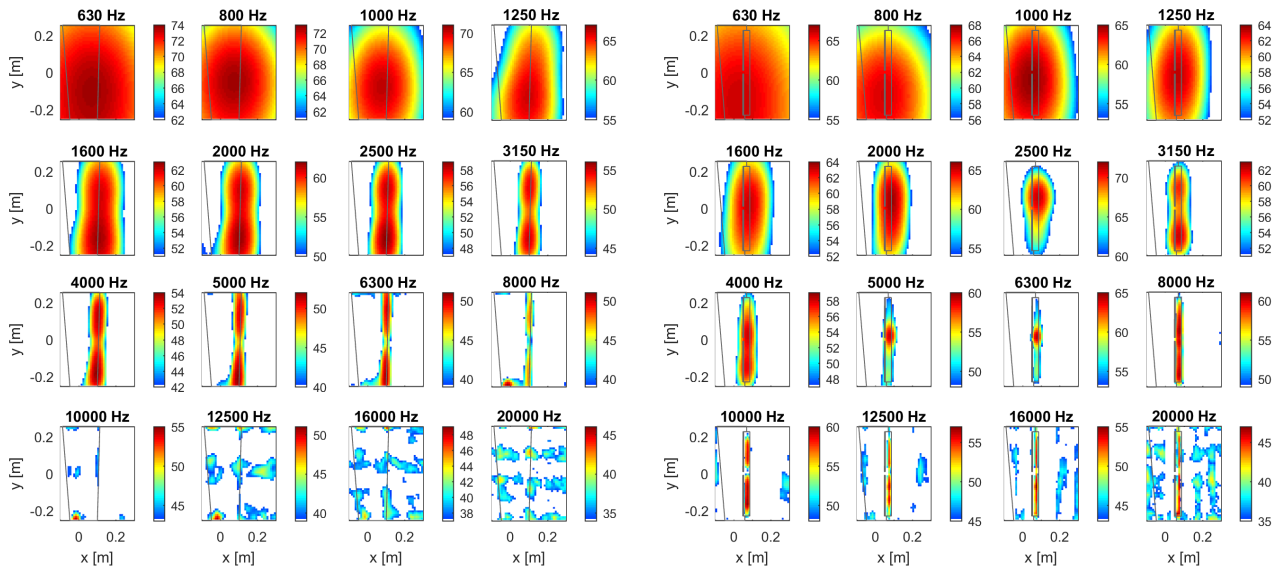


Figure D.13: Beam maps for the conventional(right) and the morphed(left) wing with 4° angle of attack and 35m/s

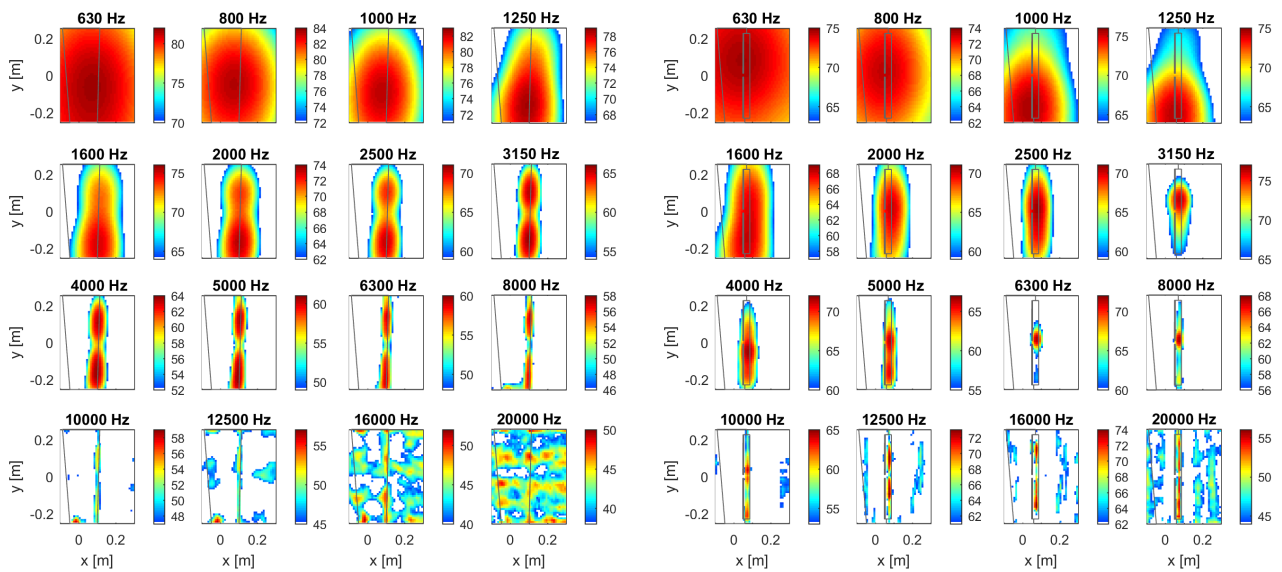


Figure D.14: Beam maps for the conventional(right) and the morphed(left) wing with 4° angle of attack and 50m/s

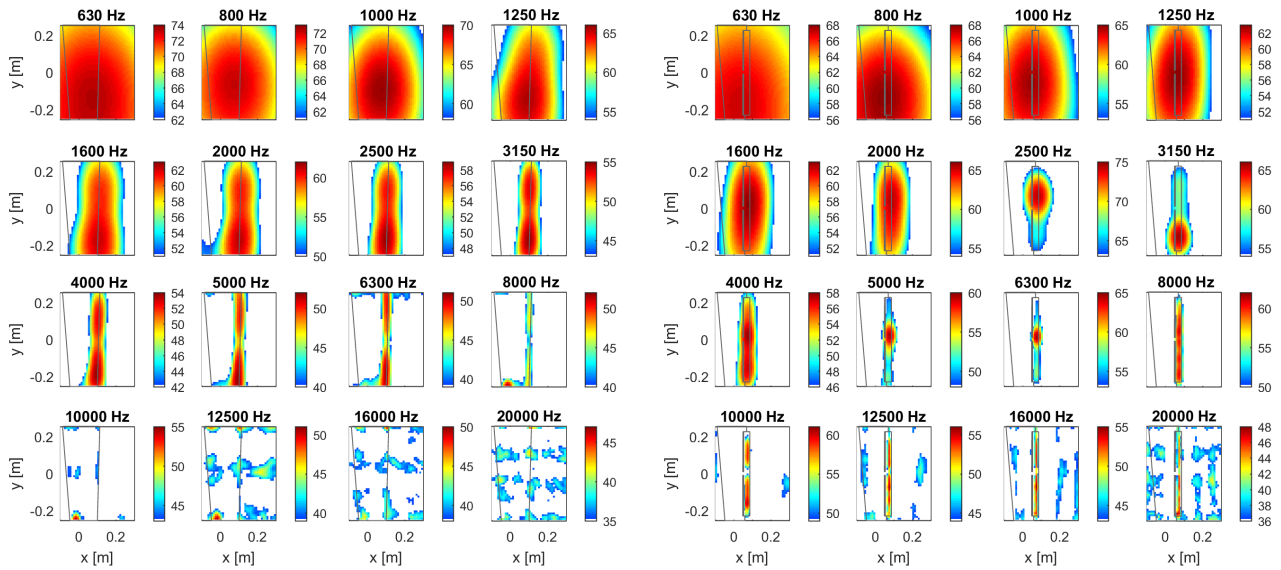


Figure D.15: Beam maps for the conventional(right) and the morphed(left) wing with 6° angle of attack and 35m/s

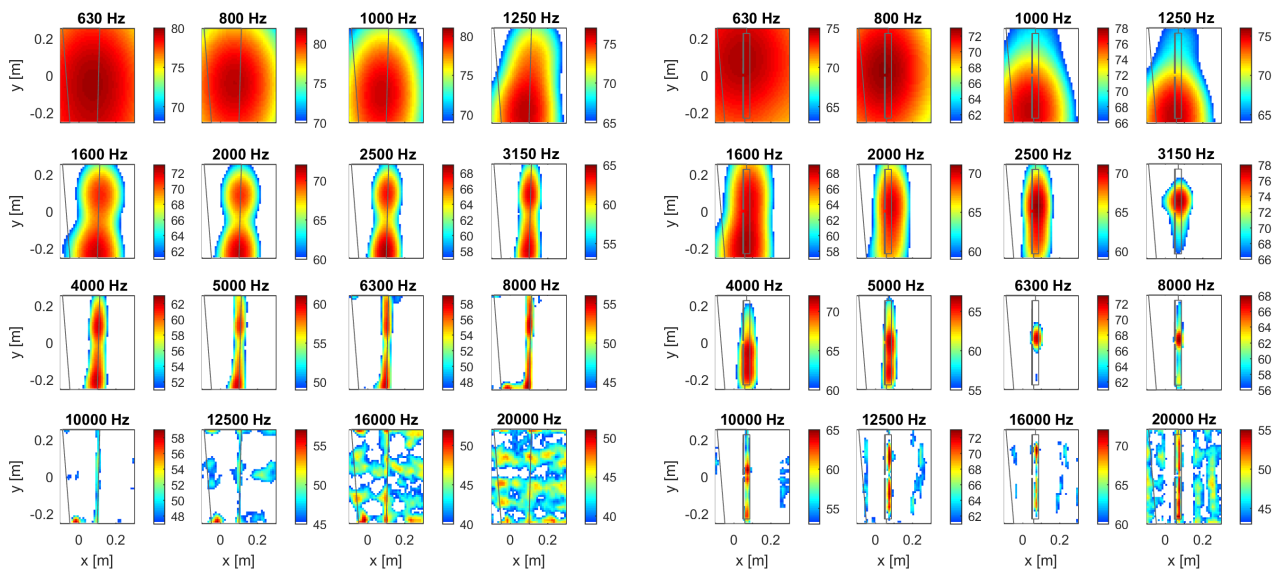


Figure D.16: Beam maps for the conventional(right) and the morphed(left) wing with 6° angle of attack and 50m/s

Bibliography

- [1] Predator B: The Multi-Role UAV. Technical report, General Atomics Aeronautical Systems, Inc. USA, 2002. URL <http://www.dtic.mil/dtic/tr/fulltext/u2/a427459.pdf>.
- [2] D. Hilliard A. Bati and K. Vaccaro. Indoor low frequency radar cross section measurements at vhf/uhf bands. Naval Air Warfare Center Weapons Division Point Mugu, California D. L. Mensa Integrated Systems Analysts, Incorporated, Camarillo, California, 1996.
- [3] M. Abdulrahim and R. Lind. Flight Testing and Response Characteristics of a Variable Gull-Wing Morphing Aircraft. *Proceedings of AIAA Guidance, Navigation, and Control Conference and Exhibit*, 16-19 August, Providence, RI, AIAA, 2004-5113, pp. 1664-1679, 2004.
- [4] Federal Aviation Administration. Noise standards: Aircraft type and airworthiness certification, calculation of effective perceived noise level from measured data. Federal Aviation Regulations Part 36, Appendix A2 to Part 36 - Section A36.4, 2002.
- [5] Christopher Bahr, Nikolas Zawodny, Brandon Bertolucci, Kyle Woolwine, Fei Liu, Jian Li, Mark Sheplak, and Louis Cattafesta. Measurement of phased array point spread functions for use with beamforming, 06 2011.
- [6] Brozowski F. Barrett, R.M. and R.S. Gross. Design and Testing of a Subsonic All-Moving Adaptive Flight Control Surface. *AIAA Journal*, 35:1217-1219, 1997.
- [7] R.M. Barrett. Intelligent Rotor Blade Actuation through Directionally Attached Piezoelectric Crystals. *Proceedings of 46th American Helicopter Society National Conference and Forum*, 21-23 May, Washington, DC, 1990.
- [8] R.M Barrett. Active Aeroelastic Tailoring of an Adaptive Flexspar Stabilator. *Materials and Structures*, 5:723-730, 1996.
- [9] L. Bertsch. Noise prediction within conceptual aircraft design. Technical report, Technische Universität Braunschweig, 2013. URL <http://elib.dlr.de/84386/>.
- [10] Thomas F. Brooks and William M. Humphreys. A deconvolution approach for the mapping of acoustic sources (damas) determined from phased microphone arrays. *Journal of Sound and Vibration*, 294(4):856 – 879, 2006. ISSN 0022-460X. doi: <https://doi.org/10.1016/j.jsv.2005.12.046>. URL <http://www.sciencedirect.com/science/article/pii/S0022460X06000289>.
- [11] D.R. Bye and P.D. McClure. Design of a Morphing Vehicle. *Proceedings of 48th AIAA/ASME/ASCE/AHS/ASC Structures, Structural Dynamics, and Materials Conference*, 23-26 April, Honolulu, HI, AIAA 2007-1728 (16 pp), 2007.
- [12] Allen M.J. Dibley R.P. Gera J. Clarke, R. and J. Hodgkinson. Flight Test of the F/A-18 Active Aeroelastic Wing Airplane. *Proceedings of AIAA Atmospheric Flight Mechanics Conference and Exhibit*, 15-18 August, San Francisco, CA, AIAA 2005-6316 (31 pp), 2005.
- [13] Lazarus K.B. Crawley, E.F. and D.J. Warkentin. Embedded Actuation and Processing in Intelligent Materials. *Proceedings of 2nd International Workshop on Composite Materials and Structures*, 14-15 September, Troy, NY, 1989.
- [14] W. Dobrzynski, K. Nagakura, B. Gehlhar, and A. Buschbaum. Airframe noise studies on wings with deployed high lift devices. In *4th AIAA/CEAS Aeroacoustic Conference, Toulouse (fr), 02.-04.06.1998*, 1998. URL <http://elib.dlr.de/13160/>.
- [15] S.M. Ehlers and T.A. Weisshaar. Static Aeroelastic Behavior of an Adaptive Laminated Piezoelectric Composite Wing. *AIAA Journal*, 28:1611-1623, 1990.
- [16] Wadley H.N.G Elzey D.M, Sofla A.Y.N. A shape memory-based multifunctional structural actuator panel. *Inter J Solids Struct*, 42:1943-55., 2005.
- [17] J. A. Hogbom. Aperture Synthesis with a Non-Regular Distribution of Interferometer Baselines. *Astron. Astrophys. Suppl. Ser.*, 15:417-426, 1974.

- [18] Scott R. Michael L. Zink S. Weisshaar T. Ivanco, T. Validation of the Lockheed Martin Morphing Concept with Wind Tunnel Testing. Technical report, 48th AIAA/ASME/ASCE/AHS/ASC Structures, Structural Dynamics, and Materials Conference, 23 - 26 April 2007.
- [19] A. Jain and I. Patel. Ground-to-air imaging radar for rcs measurement. *IEEE Transactions on Instrumentation and Measurement*, 41(6):951–956, Dec 1992. ISSN 0018-9456. doi: 10.1109/19.199441. URL <https://doi.org/10.1109/19.199441>.
- [20] Brüel & Kjær. Microphone handbook volume 1. Technical Documentation, July, 1996.
- [21] Shaeffer J. Knott, E. and M. Tuley. Certification of the point mugu bistatic anechoic chamber for uhf rcs measurements. Radar Reflectivity Laboratory, Naval Air Warfare Center Weapons Division, Point Mugu, CA, 1995.
- [22] J.N. Kudva and B. Carpenter. Smart Wing Program. *Proceedings of DARPA Technology Interchange Meeting*, 2000.
- [23] D.P. Lockard and G.M. Lilley. The Airframe Noise Reduction Challenge. Technical report, NASA, 2004. URL <https://ntrs.nasa.gov/search.jsp?R=20040065977>.
- [24] Garcia E. Wickenheiser A. Manzo, J. and G.C. Horner. Design of a Shape-Memory Alloy Actuated Macro-scale Morphing Aircraft Mechanism. *Proceedings of SPIE Smart Structures and Materials 2005: Smart Structures and Integrated Systems, San Diego CA*, 5764, p. 744, 2005.
- [25] J. Manzo and E. Garcia. Demonstration of an in situ Morphing Hyperelliptical Cambered Span Wing Mechanism. *Smart Materials and Structures*, 19:02 5012, 2010.
- [26] Kudva J. Austin F. Jardine A.P. Scherer L.B. Lockyer A.J. Martin, C.A. and B.F. Carpenter. Smart Materials and Structures-Smart Wing Volumes I, II, III, and IV. Technical report, AFRL-ML-WP-TR-1999-4162, Northrop Grumman Corporation, Hawthorne, CA., 1998.
- [27] Robert J. McGhee and William D. Beasley. Low-Speed Aerodynamic Characteristics of a WPercent-Thick Medium- Speed Airfoil Designed for General Aviation Applications. Technical report, NASA Langley Research Center, 1980.
- [28] G.D. Miller. Active Flexible Wing (AFW) Technology. Technical report, AFWAL-TR-87-3096, Rockwell International North American Aircraft Operations, Los Angeles, CA., 1988.
- [29] H. Miller. Study of low frequency aircraft takeoff noise at Baltimore- Washington international airport. *HMMH*, 1998.
- [30] Ian Moir and Allan G. Seabridge. *Military Avionics Systems (Aiaa Education)*. Amer Inst of Aeronautics &, 2006. ISBN 1563478331.
- [31] K.S. Pearsons, BOLT BERANEK, and NEWMAN INC VAN NUYS CA. *THE EFFECTS OF DURATION AND BACKGROUND NOISE LEVEL ON PERCEIVED NOISEINESS*. Defense Technical Information Center, 1966. URL <https://books.google.nl/books?id=87JKAQAACAAJ>.
- [32] L. Pellett. Vhf/uhf indoor rcs measurements using a tapered or compact range. Proceedings of the 1991 Antenna Measurement Techniques Association, 1991.
- [33] Bessette D. Field P.B. Miller G.D. Pendleton, E.W. and K.E. Griffin. Active Aeroelastic Wing Flight Research Program: Technical Program and Model Analytical Development. *Journal of Aircraft*, 37:554-561, 2000.
- [34] Reed J.L. Perkins, D.A. and E. Havens. Morphing Wing Structures for Loitering Air Vehicles. *Proceedings of 45th AIAA/ASME/ASCE/AHS/ASC Structures, Structural Dynamics & Materials Conference*, 19-22 April, Palm Springs, CA, AIAA 2004-1888 (10 pp)., 2004.
- [35] M. R. Ramdjanbeg, L. Bertsch, K.-S. Rossignol, and D. G. Simons. *Flap Side-Edge Noise Prediction Within Conceptual Aircraft Design*, pages 731–742. Springer International Publishing, Cham, 2016. ISBN 978-3-319-27279-5. doi: 10.1007/978-3-319-27279-5_64. URL http://dx.doi.org/10.1007/978-3-319-27279-5_64.
- [36] D.P. Raymer. *Aircraft Design: A Conceptual Approach*. The American Institution for Aeronautics and Astronautics, Inc., 1992.
- [37] Karl-Stéphane Rossignol. Empirical prediction of flap tip noise. In *17th AIAA/CEAS Aeroacoustics Conference*, June 2011. URL <http://elib.dlr.de/70199/>.

- [38] Peter K. C. Rudolph. High-Lift Systems on Commercial Subsonic Airliners. Technical report, NASA, 1996. URL <https://ntrs.nasa.gov/archive/nasa/casi.ntrs.nasa.gov/19960052267.pdf>.
- [39] R. M. Ajaj M. I. Friswell S. Barbarino, O. Bilgen and D. J. Inman. A review of morphing aircraft. *Journal of Intelligent Material Systems and Structures* 22, 823, 2011.
- [40] Abhishek Kumar Sahai. *Consideration of aircraft noise annoyance during conceptual aircraft design*. Dissertation, Rheinisch-Westfälische Technische Hochschule Aachen, Aachen, 2016. URL <https://publications.rwth-aachen.de/record/668901>. Veröffentlicht auf dem Publikationsserver der RWTH Aachen University; Dissertation, Rheinisch-Westfälische Technische Hochschule Aachen, 2016.
- [41] Gurovich A.Y. Albee W. W. Sharp, B.H. Study of low-frequency aircraft noise research and mitigation. Technical report, Wyle Report WR 01-21, Wyle Acoustics Group, 2001.
- [42] P. Sijtsma. Acoustic beamforming for the ranking of aircraft noise. Technical report, Netherlands Aerospace Center (NLR), 2012. URL <http://hdl.handle.net/10921/482>.
- [43] M.D. Skillen and W.A. Crossley. Modeling and Optimization for Morphing Wing Concept Generation II Part I: Morphing Wing Modeling and Structural Sizing Techniques. Technical report, NASA/CR-2008-214902, 2008.
- [44] Michael J. T. Smith. *Noise levels, scales and indices*, page 285–289. Cambridge Aerospace Series. Cambridge University Press, 1989. doi: 10.1017/CBO9780511584527.011.
- [45] Meguid S.A. Tan K.T. Sofla, A.Y.N. and W.K. Yeo. Shape Morphing of Aircraft Wing: Status and Challenges. *Materials and Design*, 31:1284 1292, 2010.
- [46] W.C. Sperry. Aircraft noise evaluation. Technical report, Federal Aviation Administration, Office of Noise Abatement, Technical Support Staff Washington, 1968. URL <http://catalogue.nla.gov.au/Record/2348638>.
- [47] Anand V.R. Birchette T. Straub, F. and B.H. Lau. SMART Rotor Development and Wind Tunnel Test. In: *Proceedings of 35th European Rotorcraft Forum 2009 (ERF 2009)*, 22-25 September, Hamburg, Germany, Article 1200 (21 pp), 2009.
- [48] E. Torenbeek. *Synthesis of Subsonic Aircraft Design*. Kluwer Academic Publishers, 1982.
- [49] Marthijn Tuinstra and Pieter Sijtsma. Suppression of spurious noise sources in airfoil self-noise measurements. In *21st AIAA/CEAS Aeroacoustics Conference*. American Institute of Aeronautics and Astronautics, 2018/05/10 2015. doi: doi:10.2514/6.2015-2689. URL <https://doi.org/10.2514/6.2015-2689>.
- [50] Roelof Vos, Ron Barrett, Roeland de Breuker, and Paolo Tiso. Post-buckled precompressed elements: a new class of control actuators for morphing wing uavs. *Smart Materials and Structures*, 16(3):919, 2007. URL <http://stacks.iop.org/0964-1726/16/i=3/a=042>.
- [51] Roelof Vos, Vijayakumari Hodigere-Siddaramaiah, and Jonathan Cooper. *Aeroelastic Flight Control for Subscale UAVs*. American Institute of Aeronautics and Astronautics, 2018/06/20 2007. doi: doi:10.2514/6.2007-1706. URL <https://doi.org/10.2514/6.2007-1706>.
- [52] T. Weisshaar. Morphing Aircraft Systems: Historical Perspectives and Future Challenges. *JOURNAL OF AIRCRAFT*, Vol. 50, No. 2, March–April, 2013. URL <http://dx.doi.org/10.2514/1.C031456>.
- [53] Stubbs M.D. Johnston C.O. Robertshaw H.H. Reinholtz C.F. Wiggins, L.D. and D.J. Inman. A Design and Analysis of a Morphing Hyper-Elliptic Cambered Span (HECS) Wing. *Proceedings of 45th AIAA/ASME/ASCE/ AHS/ASC Structures, Structural Dynamics and Materials Conference*, 19-22 April, Palm Springs, CA, AIAA 2004-1885(10 pp), 2004.
- [54] J.R. Wilson. Active Aeroelastic Wing: A New/Old Twist on Flight. *Aerospace America*, 40:34-37, 2002.
- [55] Li X. Zhang W. Yu, Y. and J. Leng. Investigation on adaptive wing structure based on shape memory polymer composite hinge. In: *International conference on smart materials and nanotechnology in engineering, China*, Proc SPIE 2007;6423:64231D-5, 2007.